

NASA TECHNICAL NOTE



NASA TN D-3975

c.1

NASA TN D-3975

LOAN COPY: RETU
AFWL
KIRTLAND AFB, N. M.



**LOAN COPY: RETU
AFWL TECHNICAL L
KIRTLAND AFB, N. M.**

**AN INVESTIGATION OF THE RESPONSE OF A
SCALED MODEL OF A LIQUID-PROPELLANT
MULTISTAGE LAUNCH VEHICLE TO
LONGITUDINAL EXCITATION**

*by William M. Thompson, Jr.
Langley Research Center
Langley Station, Hampton, Va.*





0131030

2. u/u

^{4.}
~~AN~~ INVESTIGATION OF THE RESPONSE OF A SCALED MODEL OF
A LIQUID-PROPELLANT MULTISTAGE LAUNCH VEHICLE
TO LONGITUDINAL EXCITATION

By William M. Thompson, Jr.

Langley Research Center
Langley Station, Hampton, Va.

^{3.}
NATIONAL AERONAUTICS AND SPACE ADMINISTRATION

For sale by the Clearinghouse for Federal Scientific and Technical Information
Springfield, Virginia 22151 - CFSTI price \$3.00

AN INVESTIGATION OF THE RESPONSE OF A SCALED MODEL OF
A LIQUID-PROPELLANT MULTISTAGE LAUNCH VEHICLE
TO LONGITUDINAL EXCITATION*

By William M. Thompson, Jr.
Langley Research Center

SUMMARY

The longitudinal vibration characteristics of a scaled dynamic model of a liquid-propellant multistage launch vehicle were investigated experimentally and analytically. Experimental data were obtained for the model when sinusoidally excited in the longitudinal direction through the stage I engine gimbals. The structure was supported in a suspension system that offered negligible restraint to longitudinal motion, and the vibration response was measured with different simulated fluid-propellant loadings representing flight times of: 0 sec (stage I engine ignition), 40 sec, 80 sec, 120 sec, and 152 sec (stage I engine burnout). These results are presented and discussed. Longitudinal vibration response of the model was computed by using a two-dimensional mathematical model consisting of axisymmetric shell, fluid, and mass components. A comparison of computed and measured results shows good agreement for the two basic longitudinal structural modes.

INTRODUCTION

The development of large launch vehicles in recent years has been a major outgrowth of the accelerated space program in the United States. Large liquid-propellant launch vehicles include the Atlas, Titan II, and Saturn I, all of which have successfully flown, and the larger Saturn V, which is under development. Since high cost and payload preservation require a high operational reliability of the launch vehicle system, a reliable structural design is necessary for the launch vehicle to survive the shock and vibration environment encountered during transportation to the launch site, erection on the launch pad, launch, and flight. This environment contains many sources of transient and quasi-steady-state excitation that may produce undesirable vibration response levels in the vehicle structure. Due to the many sources and the incompletely defined nature of

*The information presented herein is largely based on a thesis submitted in partial fulfillment of the requirements for the degree of Master of Science in Engineering Mechanics, Virginia Polytechnic Institute, Blacksburg, Virginia, October 1966.

dynamic excitation forces acting on launch vehicles, it is important that the structural dynamic characteristics be understood to achieve a reliable design of the structure and to prevent control instability problems.

Analytical techniques are widely used to study the vibration characteristics of launch vehicles; however, the procedures generally involve simplifications and do not always adequately represent the complex structure of the launch vehicles. For this reason, present state-of-the-art calculation procedures must generally be verified by experimental data, which may be obtained by the use of dynamically similar models at much less cost and in less time than would be necessary for similar tests with a full-scale vehicle (refs. 1, 2, and 3). Recently, a ground vibration survey of a scaled model of a liquid-propellant multistage launch vehicle was conducted (ref. 4). The purpose of these tests was to provide sufficient experimental data on the launch-vehicle structure to verify analysis and thereby eliminate the necessity of a full-scale test program.

This report presents a study of the response to longitudinal sinusoidal excitation of a scaled model of a liquid-propellant multistage launch vehicle. The purpose of the investigation is to study in detail the longitudinal response phenomena of a typical multistage liquid-propellant vehicle. Experimental data, consisting of mode shapes and associated resonant frequencies, were obtained when the model was loaded with different quantities of simulated propellant. These loadings represented flight times during the vehicle launch trajectory ranging from stage I engine ignition to burnout. Analytical mode shapes and associated resonant frequencies were computed by using a finite-element mathematical model (ref. 5) and are compared with corresponding experimental results.

SYMBOLS

The units used for the physical quantities defined in this paper are given both in the U.S. Customary Units and in the International System of Units (SI). Factors relating the two systems are given in reference 6.

A	area, in ² (m ²)
A _c	total cross-sectional area of circumferential stiffeners, in ² (m ²)
A _l	total cross-sectional area of longitudinal stiffeners, in ² (m ²)
C _{ij}	orthotropic stiffness coefficients
E	Young's modulus of elasticity, lb/in ² (N/m ²)

f	frequency, cps
I	area moment of inertia, in ⁴ (m ⁴)
I'	mass moment of inertia, in-lb-sec ² (m-N-sec ²)
I _{c,cg}	moment of inertia about center of gravity of the skin and circumferential stiffener combination, in ⁴ (m ⁴)
I _{l,cg}	moment of inertia about center of gravity of the skin and longitudinal stiffener combination, in ⁴ (m ⁴)
k	spring constant, lb/in. (N/m)
l	normalization station on longitudinal axis of model, 254 in. (6.46 m)
L	length, in. (m)
L _S	length of shell component, in. (m)
m	mass, lb-sec ² /in. (kg)
n	scale factor
r	radius of model, 12 in. (0.3048 m)
t	flight time (t = 0 at stage I ignition), sec
t ₁	skin thickness, in. (m)
t _{c,av}	average thickness of circumferential stiffener and skin combination, in. (m)
t _{l,av}	average thickness of longitudinal stiffener and skin combination, in. (m)
x	distance along longitudinal axis of model from station 0, in. (m) (see fig. 1)
x _{cg}	distance along longitudinal axis of model from station 0 to center of gravity, in. (m)

θ angular coordinate, deg

μ Poisson's ratio, 0.3

Subscripts:

f full-scale

m model

MODEL DESCRIPTION

Scaling

In the design of the model, direct geometric scaling was used whenever practical to insure faithful reproduction of the dynamic characteristics of the full-scale vehicle. It should be emphasized, however, that the structure is not a replica model and that some component items were represented by simple structural designs which were dynamically similar to the prototype. Examples of this substitution include lumped masses for equipment items and engines and simple shapes for shell stiffeners for which cross-sectional area and area moment of inertia are scaled. The various geometric and structural properties of the model were scaled by the following relationships in which n is the scale factor:

Length	$L_m = nL_f$
Area moment of inertia	$I_m = n^4 I_f$
Mass	$m_m = n^3 m_f$
Frequency	$f_m = (1/n) f_f$
Mass moment of inertia	$I'_m = n^5 I'_f$

The subscripts m and f represent model and full-scale quantities, respectively.

Description

The materials used for the model structure are the same as those used for the full-scale vehicle except that in some cases different alloys were substituted to simplify fabrication. The model configuration and major components are shown in figure 1. The basic components are described briefly in the following paragraphs.

Payload.- A payload scaled to represent a 5000-lb (2268-kg) undefined potential full-scale payload was used in the tests. The payload, shown in figure 2, consists of a

thin-walled (0.049 in. or 1.24 mm) aluminum tube, 6 in. (0.152 m) in diameter, and 33 in. (0.838 m) in length with lead ballast attached circumferentially near the top and bottom of the cylinder. The cylinder is connected to a cutout conical-frustum structure which allows mating of the payload to the top of the vehicle.

Transtage.- The transtage section, shown in figure 3, consists of a steel plate on which lead ballast was symmetrically distributed. The weight was positioned in the model within 2 in. (5.08 cm) of the location of the center of gravity scaled from the prototype. As noted for the payload, the transtage is a representative mass and not scaled from a full-size transtage structure.

Stage II.- The components of stage II consist of the fuel and oxidizer tanks and tank skirts and the propulsion system. A view of stage II, looking toward the forward oxidizer skirt, is shown in figure 4. The forward oxidizer section is a thin-skin (0.009 in. or 0.229 mm) structure 30 in. (0.762 m) long and 24 in. (0.610 m) in diameter, reinforced by longitudinal stringers and internal circumferential stiffeners riveted to the skin. The locations of the stiffeners inside the structure are indicated by the lines of rivets in the tank skirts shown in figure 4. The approximate locations of the center portions of the oxidizer and fuel tanks are indicated by the weld lines running circumferentially around the model (fig. 4). Both the oxidizer tank (volume: 4.05 ft³ or 0.115 m³) and the fuel tank (volume: 3.60 ft³ or 0.102 m³) were full during the vibration tests. The full-scale liquid propellants were simulated by inert liquids having the same density as the actual propellants (table 1). The simulated stage II engine was scaled only by weight and is shown in figure 5. The structure consisted of a steel cylinder 7.5 in. (0.190 m) in diameter, 12.5 in. (0.318 m) long, and 0.125 in. (3.18 mm) thick.

TABLE 1.- SIMULATED LIQUID PROPELLANT

Propellant	Mixture (by weight)	Specific gravity
Oxidizer	50.2 freon 49.8 methylene chloride	1.42
Fuel	57.0 alcohol 43.0 water	0.93

Stage I.- The transportation section (which houses the stage II propulsion simulation), the two large liquid-propellant tanks, and the twin-engine propulsion module constitute the first stage of the model. The transportation section shown in figure 6 is a thin-skin (0.009 in. or 0.229 mm) structure 24 in. (0.610 m) in diameter. It is longitudinally and circumferentially stiffened and is similar in construction to the stage II tank skirts. The oxidizer tank (volume: 15.48 ft³ or 0.428 m³) and fuel tank (volume: 13.01 ft³ or 0.368 m³) can also be loaded with the liquids identified in table 1. The

general structure of these tanks is basically the same as that of the partially completed fuel tank in figure 7. The cylindrical barrel of the tank is assembled from two sections 0.023 in. (0.584 mm) thick welded at two seams 180° apart and running longitudinally along the tank. The cylindrical part of the structure is stiffened internally by longitudinal members welded to the skin and circumferential stiffeners attached to the longerons. The oxidizer tank has 12 circumferential stiffeners and 36 longitudinal stringers; the fuel tank has 10 circumferential stiffeners and 32 longitudinal stringers. The completed stage I oxidizer tank is shown in figure 8. In the operational flight vehicle the oxidizer is pumped to the stage I engines through a tube running longitudinally from the bottom of the oxidizer tank through the fuel tank to the engines. The transfer tube (fig. 9) in the model contained simulated oxidizer fluid during vibration tests in which liquid propellants were required in the stage I tanks. The position of the oxidizer transfer tube is indicated in figure 1. The stage I engines and thrust frames were dynamically scaled in the model as shown in figure 10.

Physical data. - Weights of the major model components are summarized in table 2. The weight data were calculated from the dimensions and material density of the structural elements of the model. The payload weight was obtained by weighing the actual payload configuration provided for the tests. A detailed breakdown of the model weight data is provided in table 3, in which the center-of-gravity locations are also included. The longitudinal stiffness parameter AE for the model is shown as a function of length in figure 11. Young's modulus E is 10^7 psi (68 948 meganewtons/meter²) and A represents the cross-sectional area of the structural components of the model that resist longitudinal (axial) elastic motion. These areas exclude the area of the 0.009-inch-thick (0.229 mm) skin covering most of the second stage and transportation section. The omission of this skin area is discussed later in the analytical investigation.

TABLE 2.- MODEL COMPONENT WEIGHTS

Component	Empty		Full fuel load	
	lb	kg	lb	kg
Payload	35.7	16.2	35.7	16.2
Transtage	213.2	96.7	213.2	96.7
Stage II	50.0	22.7	586.4	266.0
Stage I	87.5	39.7	2098.0	951.7
Total	386.4	175.3	2933.3	1330.6

TABLE 3.- WEIGHT AND CENTER OF GRAVITY OF STRUCTURAL ITEMS OF MODEL

Item	Weight		x_{cg}/l	Component
	lb	kg		
Payload	35.7	16.2	-0.007	Payload
Control-module skirt	2.19	0.99	0.083	Transtage
Transtage	211.0	95.7	.105	
Forward oxidizer skirt	7.36	3.34	0.151	Stage II
Forward oxidizer dome	3.02	1.37	.203	
Oxidizer-tank barrel	2.40	1.09	.230	
Aft oxidizer skirt	4.15	1.88	.254	
Aft oxidizer dome	1.60	.73	.258	
Equipment truss	3.94	1.79	.275	
Forward fuel dome	3.16	1.43	.293	
Forward fuel skirt	2.90	1.32	.300	
Fuel-tank barrel	2.23	1.01	.319	
Aft fuel skirt	4.89	2.22	.344	
Aft fuel dome	2.86	1.30	.344	
Engine simulation	11.44	5.19	.392	
Oxidizer (full)	343.7	155.9	0.231	
Fuel (full)	192.7	87.4	.321	
Transportation section	9.40	4.26	0.413	Stage I
Forward oxidizer dome	3.08	1.40	.478	
Forward oxidizer skirt	2.81	1.27	.485	
Oxidizer-tank barrel	15.56	7.06	.588	
Aft oxidizer skirt	2.47	1.12	.696	
Aft oxidizer dome	2.30	1.04	.705	
Forward fuel skirt	4.06	1.84	.737	
Forward fuel dome	2.94	1.33	.742	
Fuel-tank barrel	18.90	8.57	.840	
Aft fuel skirt	7.31	3.32	.936	
Aft fuel cone	4.88	2.21	.944	
Engines	13.8	6.26	1.000	
Oxidizer (full)	1321.1	599.3	0.598	
Fuel (full)	689.5	312.8	.843	
Suspension system	110.0	49.9	0.951	

TEST APPARATUS

Suspension System

The suspension system shown schematically in figure 12 consisted, basically, of cable supports on both sides of the model. The system was designed for use with several model configurations and therefore employed large cables and fixtures to support a wide range of weights. On each side of the model one end of the support cable was attached to a yoke which connected to two other cables that supported a cradle fastened to the base of the model. Each of the two support cables passed through an overhead pulley and

terminated at a leaf spring located near the model base. The model was stabilized by a set of horizontal cables connecting the yoke to the model at $x/l = 0.146$. A picture of the model in the suspension system prior to the longitudinal tests is shown in figure 13.

The degree of restraint to longitudinal motion offered by the suspension system was determined experimentally. The impedance of the system was measured over the frequency range of the model vibration tests when the suspension system was loaded with a rigid mass equal to the mass of the completely empty model. The test results showed a negligible variation between the measured impedance of the combination of suspension system and rigid mass and the impedance of the rigid mass alone. The suspension system, therefore, is considered to offer negligible restraint to longitudinal motion of the model for the propellant loading conditions tested.

A static load-deflection relationship of the suspension system was measured prior to the vibration tests and a spring constant of 4500 lb/in. (788 kN/m) was determined. With this value and the appropriate model weight, the calculated resonant frequency of the model acting as a rigid body in the suspension system ranges from approximately $3\frac{1}{2}$ cps for the full condition to 10 cps for the empty condition.

Instrumentation

The model was sinusoidally excited by means of a single electromagnetic shaker attached by a U-shaped rigid frame to the bottom of the model as shown in figure 14. Removal of the first-stage engines permitted the U to be attached to the model so that longitudinal excitation of the structure could be accomplished through the engine gimbals. Mass distribution of the model in this area was not altered since the U-frame equaled the combined weight of the two removed engines.

The direct-measurement instrumentation consisted of crystal-type accelerometers with cathode followers and voltage amplifiers for signal conditioning. Accelerometers were used as fixed and movable probes in determining the mode shapes at resonant frequencies. A schematic diagram of the instrumentation is shown in figure 15. All transducers were calibrated in their respective signal-conditioning systems and found to have a flat response ranging from 6 cps to above 100 cps. During the measurement of a mode shape, one fixed and one movable accelerometer were used. The movable probe was fitted with a small lightweight cup which was connected by a hose to a vacuum line. The transducer could then be secured to the model by suction and maintain the same adhesive force between the model and accelerometer at all points of measurement. A vacuum-attached probe mounted at $x/l = 0.951$ on the model is shown in figure 16.

The excitation force was measured by a crystal-type force gage inserted between the U-frame and the driving element of the shaker. (See fig. 14.) This gage was also calibrated in its signal-conditioning system and the force delivered to the model was monitored quantitatively on an rms voltmeter and qualitatively on an oscilloscope.

TEST PROCEDURE

Forced oscillation of the model in the longitudinal direction was used to obtain resonant frequencies and associated mode shapes for propellant loading conditions corresponding to flight times of 0 (stage I ignition), 40, 80, 120, and 152 sec (stage I burnout). The payload was attached during all tests. For each flight time the general procedure described in the following paragraphs was used to determine a resonant condition of the model.

With accelerometers mounted at selected locations on the structure ($x/l = 0, 0.324,$ and 1.00), a relationship between response and frequency was obtained by slowly sweeping through the frequency range of interest (usually 10 to 100 cps). During the sweep a constant input force was maintained and the output of the fixed accelerometer was determined by an rms voltmeter. The sweep was accomplished by moving the oscillator frequency selector manually in increments, usually of $1/2$ cps, in the range up to 50 cps and in increments of 1 cps in the range between 50 and 100 cps. A plot of these data provided a picture of the model response at selected points on the structure as a function of frequency. Using manual sweep data as a guide, individual modes were tuned by seeking the frequencies at which the maximum response of an antinode on the model was noted for a constant force input.

The mode shapes associated with the resonances were measured by using both the fixed and movable probes in the following manner: Once a resonant condition of the model was excited, the fixed and movable probes were attached near the antinode at which the maximum displacement occurred. The transducer signals were filtered to eliminate signal noise and fed into an oscilloscope displaying a Lissajous figure which indicated the relative phase between the output signals of these probes. The unfiltered signal from the movable accelerometer was monitored by an rms voltmeter which indicated the model response in g units at the points of measurement. Therefore, by moving the roving probe to different stations on the model, the phase (from the oscilloscope) and amplitude (in g units from the rms voltmeter) of the response at any location on the model relative to the location of the fixed accelerometer was read directly.

The model response was investigated by attaching the vacuum-held accelerometer to plastic blocks positioned at 90° intervals around the model circumference. A set of four blocks was located at each of 15 stations along the length of the model. The orientation of the blocks, numbered as positions 1, 2, 3, and 4, was such that an arrow through

positions 1 and 3 pointed in the pitch direction and an arrow through positions 2 and 4 indicated the yaw direction. At a given station, measurements were obtained at all four blocks to determine longitudinal motion, at block positions 2 and 4 to determine pitch motion, and at block positions 1 and 3 to determine yaw response. The vacuum-attached probe shown in figure 16 is longitudinally oriented on block 4 at $x/l = 0.951$.

Resonant frequencies and associated mode shapes were determined experimentally by the above procedure for the desired propellant loadings. The liquid propellants were fed into the stage I and stage II tanks by gravity aided by pressurization of the propellant storage container. The amount of fluid injected into the tanks was controlled by monitoring the weight loss of the storage containers during the filling process. All propellant loading data for the flight times are shown in table 4.

TABLE 4.- MODEL PROPELLANT LOADING BY WEIGHT

Component	Oxidizer		Fuel		
	lb	kg	lb	kg	
Stage II	343.7	155.9	192.7	87.4	
Stage I	t = 0 sec	1321.1	599.3	689.5	312.8
	t = 40 sec	973.4	441.5	508.1	230.5
	t = 80 sec	625.7	283.8	326.6	148.1
	t = 120 sec	278.1	126.1	145.2	65.9
	t = 152 sec	0	0	0	0

ANALYTICAL PROCEDURE

Description of Mathematical Model

The longitudinal response of the vehicle was calculated by using a two-dimensional analytical model as derived in reference 5. The analysis utilizes a finite-element technique to construct the total launch-vehicle stiffness and mass matrices by subdividing the structure into a set of: (1) axisymmetric shell components, (2) fluid components, and (3) spring-mass components. By this method the vehicle fairing, interstage structure, bulkheads, tank walls, and engine-thrust structure may be represented as separate shell units. Also the inertial and stiffness characteristics of equipment, engines, and vehicle support structure can be provided conveniently. The mass and stiffness characteristics are computed for the individual components by using a Rayleigh-Ritz approach. The mass and stiffness matrices for the complete launch vehicle are obtained by superposition of the mass and stiffness matrices of the components. An eigenvalue equation constructed from the total-system mass and stiffness matrices will then yield the natural

frequencies and mode shapes of the system. Although the analysis accounts for shell motion, the circumferential modes of the shell components are limited to the axisymmetric case. In the longitudinal direction, the number of possible patterns is dictated by the assumed polynomial mode shape as governed by the number of coordinates chosen to define the shell wall motion.

A computer program to calculate the longitudinal vibration response of the test specimen by the component method is provided in reference 7 and was used to calculate the model response. The response of the structure is computed at discrete points located at intersections of shell components, at lumped masses, and at intermediate points between the extremities of the shell components. The model was divided into 29 shell components, a maximum of 4 liquid components, and a maximum of 7 spring-mass elements. The division of the model is shown in figure 17, in which the locations of the selected system coordinates (numbered 1 to 85) are indicated by the small arrows. Coordinates 1 to 37 denote longitudinal motion, 38 to 57 denote radial motion (also, 81 to 85 indicate zero radial motion), and 58 to 80 indicate rotation at shell extremities. Intermediate points 19 and 25 were chosen to provide longitudinal stage I midtank motion. Coordinates 50 to 52 on the stage I oxidizer-tank barrel and 56, 57, and 83 on the fuel-tank barrel provide radial tank-wall motion in a line which parallels the longitudinal axis of the model. The longitudinal motion is also computed for the center of the stage II forward oxidizer skirt (coordinate 4) and the center of the transportation section (coordinate 15).

Computer-Program Input

The physical data for the model, which constituted the prime input to the computer program, were extracted from drawings showing details of the vehicle structure. In addition, an input consisting of an effective mass of the suspension system was calculated and assumed to act as part of the model mass lumped at the aft end of the structure ($x/l = 0.951$) during longitudinal response. An effective mass was included in the calculation since the suspension-system mass was appreciable relative to the mass of the model for some of the propellant loading conditions of the investigation. In calculating the effective mass, the suspension system was idealized as two linear springs in series; one spring represented the support cables and the second the leaf springs near the base of the model. The stiffness of the leaf springs was determined by using the measured system spring constant and a spring constant for the support cables calculated from the AE/L interpretation of stiffness value. The length (i.e., the mass) of each leaf spring undergoing deflection could then be calculated by assuming that the spring deflects as a cantilevered beam loaded at the free end. The effective mass of the suspension system was therefore approximated as the sum of the masses of the model suspension cradle, the cable connections and turnbuckles, the deflected length of the leaf spring, and

one-third the mass of the cables. An effective mass of 110 lb (49.9 kg) was determined by this procedure.

The suspension-system effective mass and certain equipment items were represented as lumped masses attached either to the shell components or to a linear spring of known stiffness. In this computation, as suggested by the structure in figure 17, the transtage (mass 2), the stage II equipment truss (mass 3), the suspension system (mass 5), and the fluid mass in the oxidizer feed line concentrated at the small end of the stage I fuel-tank aft cone (mass 7) were incorporated in the mathematical model as lumped masses attached to the indicated shells. The payload (mass 1), the stage I engines (mass 6), and the stage II propulsion system (mass 4) were considered as lumped masses attached by linear springs.

A stiffness constant for the spring between: (1) the payload mass and the first mass of the basic structure, (2) the stage II engines and the stage II bottom fuel dome, and (3) the stage I engines and the aft end of the model was determined experimentally in each case by tapping the mass with a rubber mallet and electronically measuring the resonant frequency. The spring constants were calculated by assuming a single-degree-of-freedom response of each mass. In measuring these data every effort was made to detect the component fundamental response; however, the procedure is admittedly unsophisticated and the accuracy in obtaining uncoupled single-degree-of-freedom response for these cases is uncertain. This method was employed to obtain the spring stiffness for the model payload since the effective spring in a conical, frustum-shaped structure with cutout portions (fig. 2) cannot be accurately represented by an AE/L value. Similarly, the AE/L spring-constant representation is not applicable to the conical structure connecting the stage II engines to the aft fuel-tank dome (see fig. 5) and the angled bracing members between the stage I engines and the aft end of the model (fig. 10). The experimentally determined spring constants and the stations at which connection was assumed on the mathematical model are given in table 5.

TABLE 5.- MEASURED SPRING CONSTANTS

Component to which spring is attached	Spring constant, k		x/l
	lb/in.	kN/m	
Control module skirt	15 000	2 630	0.061
Stage II fuel-tank barrel	106 000	18 560	.319
Stage I aft fuel-tank skirt	136 000	23 810	.951

The fluid-component input consists basically of the fluid mass, density, and liquid height in each element of the shell component at the different simulated flight times. These data are presented in table 6.

TABLE 6.- LIQUID HEIGHT AND WEIGHT IN INDICATED SHELL AT FLIGHT TIME

Time, t, sec	Oxidizer tank ^a					Fuel tank ^b				
	Shell no.	Fluid height		Fluid weight		Shell no.	Fluid height		Fluid weight	
		in.	m	lb	kg		in.	m	lb	kg
Stage II										
0, 40, 80, 120, 152	{ -7 5 -3	8.5 4.3 6.1	0.22 .11 .16	130 98 116	59 44 53	{ -15 12 -10	8.5 2.6 5.8	0.22 .066 .15	83 38 72	38 17 33
Stage I										
0	{ -21 20 -19	8.5 46.6 5.8	0.22 1.18 .15	130 1070 112	59 485 51	{ 28 27 -26	9.3 40.0 4.9	0.24 1.02 .12	49 578 63	22 262 29
40	{ -21 20 -19	8.5 26.4 0	.22 .67 0	130 884 0	59 401 0	{ 28 27 -26	9.3 31.8 0	.24 .81 0	49 459 0	22 208 0
80	{ -21 20 -19	8.5 21.3 0	.22 .54 0	130 488 0	59 221 0	{ 28 27 -26	9.3 19.3 0	.24 .49 0	49 278 0	22 126 0
120	{ -21 20 -19	8.5 6.1 0	.22 .16 0	130 139 0	59 63 0	{ 28 27 -26	9.3 6.7 0	.24 .17 0	49 96 0	22 44 0
152	{ -21 20 -19	0 0 0	0 0 0	0 0 0	0 0 0	{ 28 27 -26	0 0 0	0 0 0	0 0 0	0 0 0

^aDensity of oxidizer: 0.1311×10^{-3} lb-sec²/in⁴ (3.63 kg/m³).

^bDensity of fuel: 0.0842×10^{-3} lb-sec²/in⁴ (2.33 kg/m³).

As previously stated, the cross-sectional area of the thin (0.009-in. or 0.229-mm) skin covering most of the second stage and the transportation section is not included in the plot of longitudinal stiffness parameter AE shown in figure 11. This omission is considered justified because slight buckling of the skin between stiffeners is visible throughout the model second stage. The condition is obviously caused by the lines of rivets connecting the skin to the longitudinal and circumferential stiffeners (e.g., see figs. 4 and 6) which dimple the skin between stiffeners. The buckled skin is assumed to offer negligible resistance (relative to that of the longitudinal and circumferential stiffeners) to longitudinal and hoop stress. Therefore, in the model response computations the contribution of the 0.009-in. (0.229-mm) skin to longitudinal and hoop stiffness is neglected.

The inputs most difficult to define for the component model program are the orthotropic stiffness factors, which must be calculated from structural details of the shell components. Most of the shell components in the model consist primarily of a skin with closely spaced longitudinal stringers but relatively widely spaced

circumferential ring stiffeners. In tank skirts and interstage structure of the model, stiffeners were frequently unevenly spaced and different in size and shape. An exception to this general arrangement occurs in the stage I oxidizer and fuel-tank barrels, where all stiffeners are evenly spaced and the ratio of the number of circumferential ring stiffeners to longitudinal stiffeners is roughly one to three, as indicated previously in the description of the model. In all cases, however, stiffened shell walls were considered orthotropic material for which the stiffness was obtained by averaging the discrete stiffness of the individual elements into an effective wall thickness. Applying this principle, the stiffness coefficients were calculated by using the following relationships:

$$C_{11} = \frac{Et_{l,av}}{1 - \mu^2} \quad (1)$$

$$C_{22} = \frac{Et_{c,av}}{1 - \mu^2} \quad (2)$$

$$C_{12} = C_{21} = \frac{\mu(C_{11} + C_{22})}{2} \quad (3)$$

$$C_{33} = \frac{EI_{l,cg}}{2\pi r(1 - \mu^2)} \quad (4)$$

$$C_{44} = \frac{EI_{c,cg}}{L_s(1 - \mu^2)} \quad (5)$$

$$C_{34} = C_{43} = \frac{\mu(C_{33} + C_{44})}{2} \quad (6)$$

where $\mu = 0.3$ in all calculations involving skin and stiffener combinations. In these equations, $t_{l,av}$ and $t_{c,av}$ are the average thickness of the longitudinal stiffener and skin combination and of the circumferential stiffener and skin combination as given by:

$$t_{l,av} = t_1 + \frac{A_l}{2\pi r} \quad t_{c,av} = t_1 + \frac{A_c}{L_s}$$

The moments of inertia $I_{l,cg}$ and $I_{c,cg}$ are taken about the center of gravity of the skin-longitudinal stiffener combination and of the skin-circumferential stiffener combination. The form of the stiffness coefficient equations (1) to (6) deviates slightly from that usually found in the literature. The altered versions were used in the calculation to conform with the skin-stiffener averaging technique previously described. It should be noted

that the 0.009-in. (0.229-mm) skin is omitted only in calculation of C_{11} , C_{22} , and C_{12} , the coefficients defining longitudinal and hoop rigidity. The effect of the skin is included in the calculation of the other coefficients, which denote bending rigidity. The calculated stiffness data are provided in table 7.

TABLE 7.- SHELL STIFFNESS COEFFICIENTS

Shell no.	Component	C_{11}		$C_{12} = C_{21}$		C_{22}		C_{33}		$C_{34} = C_{43}$		C_{44}	
		lb/in.	kN/m	lb/in.	kN/m	lb/in.	kN/m	lb-in.	N-m	lb-in.	N-m	lb-in.	N-m
1	Control-module skirt	59 700	10 500	15 400	2 700	42 600	7 460	4 200	475	1 250	141	4 110	464
2	Stage II forward oxidizer skirt	62 800	11 000	15 900	2 780	43 800	7 670	410	46	3 500	396	22 700	2 570
		104 000	18 200	22 100	3 870	43 800	7 670	8 700	983	4 700	531	22 700	2 570
-3	Stage II forward oxidizer dome	452 000	79 200	136 000	23 800	452 000	79 200	64	7	19	2	64	7
4 5 6	Stage II oxidizer-tank barrel	414 000	72 500	124 000	21 700	414 000	72 500	50	6	19	2	75	8
		350 000	61 300	105 000	18 400	350 000	61 300	28	3	14	2	62	7
		420 000	73 600	126 000	22 100	420 000	73 600	52	6	21	2	88	10
-7	Stage II aft oxidizer dome	240 000	42 000	72 000	12 600	240 000	42 000	10	1	3	1	10	1
8	Stage II aft oxidizer skirt	125 000	21 900	27 100	4 750	56 300	9 860	1 720	194	1 200	136	6 400	723
9	Stage II forward fuel skirt	125 000	21 900	28 100	4 920	62 900	11 000	1 720	194	2 100	237	12 500	1 410
-10	Stage II forward fuel dome	474 000	83 000	142 000	24 900	474 000	83 000	73	8	22	2	73	8
11 12 13	Stage II fuel-tank barrel	440 000	77 100	132 000	23 100	440 000	77 100	60	7	20	2	70	8
		421 000	73 700	126 000	22 100	421 000	73 700	44	5	18	2	76	9
		468 000	82 000	140 000	24 500	468 000	82 000	73	8	24	3	88	10
14	Stage II aft fuel skirt	124 000	21 700	28 000	4 900	63 000	11 000	1 750	198	1 360	154	7 300	825
-15	Stage II aft fuel dome	429 000	75 100	129 000	22 600	429 000	75 100	54	6	16	2	54	6
16	Transportation section	154 000	27 000	31 800	5 570	58 000	10 200	4 260	481	1 840	208	7 620	861
17 18	Stage I forward oxidizer skirt	316 000	55 300	86 100	15 100	258 000	45 200	2 950	333	1 950	220	10 000	1 130
		489 000	85 600	147 000	25 700	489 000	85 600	82	9	21	2	59	7
-19	Stage I forward oxidizer dome	462 000	80 900	139 000	24 300	462 000	80 900	68	8	20	2	68	8
20	Stage I oxidizer-tank barrel	337 000	59 000	93 900	16 400	289 000	50 600	350	40	400	45	2 310	261
-21	Stage I aft oxidizer dome	345 000	60 400	104 000	18 200	345 000	60 400	28	3	8	1	28	3
22 23	Stage I aft oxidizer skirt	478 000	83 700	143 000	25 000	478 000	83 700	76	9	26	3	97	11
		252 000	44 100	77 400	13 600	264 000	46 200	2 090	236	1 560	176	8 290	937
24 25	Stage I forward fuel skirt	305 000	53 400	58 000	10 200	81 500	14 300	2 870	324	1 300	147	5 800	655
		485 000	84 900	146 000	25 600	485 000	84 900	79	10	51	6	3 340	377
-26	Stage I forward fuel dome	441 000	77 200	132 000	23 100	441 000	77 200	59	7	18	2	59	7
27	Stage I fuel-tank barrel	312 000	54 600	83 400	14 600	244 000	42 700	481	54	454	51	2 550	288
		396 000	69 300	96 000	16 800	244 000	42 700	4 610	521	1 070	121	2 550	288
28	Stage I aft fuel cone	488 000	85 500	131 000	22 900	385 000	67 400	27 700	3 130	4 200	475	110	12
		815 000	143 000	180 000	31 500	385 000	67 400	89 000	10 060	13 400	1 510	110	12
29	Stage I aft fuel skirt	623 000	109 000	167 000	29 200	490 000	85 800	26 500	2 990	6 100	689	14 000	1 580

The analytical model also accounts for initial stresses in the shell components due to the weight distribution of the structure and internal and external tank pressure. During the model tests, the tanks were not pressurized; however, with the many propellant loadings considered, a weight distribution was established for each flight time. The data are presented in table 8, where the shell number is given with the amount of weight contributing to compressive stress in the shell at the indicated flight time.

TABLE 8.- FORCE PRODUCING SHELL COMPRESSIVE STRESS

Shell no.	Compressive force at -									
	t = 0		t = 40 sec		t = 80 sec		t = 120 sec		t = 152 sec	
	lb	kg	lb	kg	lb	kg	lb	kg	lb	kg
1	35.7	16.2	35.7	16.2	35.7	16.2	35.7	16.2	35.7	16.2
2	248.9	113	248.9	113	248.9	113	248.9	113	248.9	113
-3	0	0	0	0	0	0	0	0	0	0
4	256.3	116	256.3	116	256.3	116	256.3	116	256.3	116
5	376.1	171	376.1	171	376.1	171	376.1	171	376.1	171
6	606.7	275	606.7	275	606.7	275	606.7	275	606.7	275
-7	0	0	0	0	0	0	0	0	0	0
8	607.3	275	607.3	275	607.3	275	607.3	275	607.3	275
9	615.5	279	615.5	279	615.5	279	615.5	279	615.5	279
-10	0	0	0	0	0	0	0	0	0	0
11	618.4	281	618.4	281	618.4	281	618.4	281	618.4	281
12	694.3	315	694.3	315	694.3	315	694.3	315	694.3	315
13	830.4	377	830.4	377	830.4	377	830.4	377	830.4	377
14	831.2	377	831.2	377	831.2	377	831.2	377	831.2	377
-15	0	0	0	0	0	0	0	0	0	0
16	836.1	379	836.1	379	836.1	379	836.1	379	836.1	379
17	845.5	384	845.5	384	845.5	384	845.5	384	845.5	384
18	847.4	384	847.4	384	847.4	384	847.4	384	847.4	384
-19	0	0	0	0	0	0	0	0	0	0
20	963.4	437	851.4	386	851.4	386	851.4	386	851.4	386
-21	0	0	0	0	0	0	0	0	0	0
22	2181	989	1833	831	1487	675	1138	516	869.3	394
23	2183	990	1835	832	1489	675	1140	517	870.9	395
24	2184	991	1836	833	1490	676	1141	518	871.8	395
25	2187	992	1839	834	1493	677	1144	519	874.9	397
-26	0	0	0	0	0	0	0	0	0	0
27	2254	1022	1843	836	1497	679	1148	521	878.8	399
28	0	0	0	0	0	0	0	0	0	0
29	2787	1264	2257	1024	1730	785	1199	544	781.2	354

RESULTS AND DISCUSSION

By using the procedures previously described, experimental and computed data were obtained for the model with liquid propellant loadings which ranged from the full condition at stage I engine ignition to burnout. The data presented consist basically of mode shapes and associated frequencies but also include experimental plots of the response, measured in g units per pound (or newton) of excitation force, at several points on the structure as a function of excitation frequency.

A thorough experimental investigation of the model response to longitudinal excitation at $t = 0$ revealed that motion was not limited to the longitudinal direction. Response to longitudinal excitation was also noted in the pitch and yaw lateral planes (lateral response refers to beam-type bending of the model). Possible sources of lateral excitation in these tests were structural coupling and lateral forces due to fluid slosh in the stage I tanks. The former seems a more likely source since slosh frequencies for a 24-in.-diameter (0.61-m) cylinder are roughly one-tenth the lowest lateral mode frequency. At higher frequencies, however, fluid motion accounted for appreciable radial response of the walls of the large propellant tanks of stage I, especially when the propellant fluids occupied half or more of the tank volume. When appreciable amounts of fluid loaded the tanks, strong coupling with lateral and tank resonances was observed and identification of classical longitudinal mode shapes was not possible at the upper end of the frequency range covered in the tests. Several significant responses indicated by peaks of the response-frequency plots for $t = 0$ are presented to illustrate tank wall and coupled response in addition to the longitudinal responses. Experimental investigation of other fuel loading conditions was less complete and the major effort was devoted to measurement of the predominantly longitudinal low-frequency responses. In the following paragraphs the data are presented and discussed in more detail.

Stage I Engine Ignition

Response-frequency plots of the longitudinally excited model corresponding to stage I engine ignition ($t = 0$) are shown in figure 18. The magnitude of the response in the figure is given in g units per pound (or per newton) of excitation force, where the acceleration is the output of an accelerometer mounted on the payload at $x/l = 0$ and oriented so that the measurement axis of the accelerometer paralleled the longitudinal axis of the model. Similar data are presented in figure 18 for accelerometers mounted on the oxidizer-tank and fuel-tank walls and oriented to measure radial response. The tank response-frequency graphs do not necessarily indicate all tank modes, since the particular location of the accelerometer may be a node point for several resonant conditions of the tank. The accelerometer output shown over the frequency range is divided by the constant input force of 10 lb (44.5 N) delivered by the electromagnetic vibration exciter.

With the data shown in figure 18 as a guide, mode shapes of the model were mapped for several typical resonant conditions indicated in the sweep response data and are shown in figures 19 to 23. Each figure indicates the relative response of the structure laterally, longitudinally, and in the radial direction on the stage I propellant tanks. In general, tank radial motion was measured at a series of points on the tank wall running in two directions: (1) longitudinally along each of four lines 90° apart on the tank walls and (2) circumferentially on a line as near as possible to the station where maximum radial deflection of the tank occurred. The response measurements associated with each resonant frequency in a figure are normalized in amplitude and phase with respect to the maximum amplitude exhibited for that particular frequency. Therefore, if lateral, longitudinal, and tank response are evident for a particular resonance, the modal deflections are normalized in amplitude and phase at the point of maximum response.

The majority of the lower frequency (10 to 38 cps) resonance peaks denote lateral responses to the longitudinal excitation. (See peaks A to E and G in fig. 18 for $x/l = 0$.) The responses indicated by peaks B, D, E, and G represent pitch modes, whereas response peaks A and C denote yaw modes. In general, the longitudinally excited lateral mode shapes and frequencies agree well with the same modal response due to lateral excitation. Discrepancies were evident in some cases, however, since the longitudinal-vibration exciter attached to the first-stage-engine gimbal points imposed on the structure a different boundary condition for lateral motion from that of the laterally excited mode which was tested with a simulated free boundary.

Longitudinal response.- Predominant longitudinal response of the model occurred at two resonances (39.7 and 63.5 cps, peaks H and J in fig. 18 for $x/l = 0$) in the frequency range covered in these tests. The mode shapes corresponding to the measured frequencies are shown in figures 19 and 20 and reveal one ($f = 39.7$ cps) and two ($f = 63.5$ cps) nodes, respectively. The mode shape having one node line is accompanied by relatively small radial motion in both oxidizer and fuel tanks, whereas the "two node" mode has predominant payload motion but no other appreciable response. Also, in figure 19, it is interesting to note that the circumferential pattern of the wall of both tanks is asymmetrical.

Tank response.- In addition to motions associated with lateral and longitudinal responses already discussed, the stage I fuel and oxidizer tanks responded at resonances at which the tank wall motion constituted the predominant response. Typical examples of the deflection shapes of these tanks (normalized at the point of maximum response) are shown in figure 21 for various natural frequencies. The tank wall displacement is shown along its length at four locations around the circumference, and the circumferential mode shapes are shown at a location along the tank length as near as possible to the position of maximum response. The tank deflection mode shapes shown in figure 21 illustrate a

variety of combinations of tank response; these include well-defined shapes in one tank with negligible deflection in the other, strong response in both tanks, and symmetrical mode shapes in one and distorted shapes in the other.

No appreciable longitudinal motion was associated with this group of tank resonances. It is interesting to note that during excitation of most of these tank modes a considerable length of time was required (5 to 10 sec) for the tank wall response to attain maximum amplitude. This effect is significant since the corresponding time for radial response growth at full scale would range from 25 to 50 sec (17 to 33 percent of the total flight time). Therefore, it is conceivable that tank responses are minimized during an actual flight because combinations of excitation frequency and propellant loading which could excite tank resonances are not present long enough for maximum responses to develop.

Coupled response.- The final group of resonances (peaks I and K to P in fig. 18) for the $t = 0$ propellant loading condition are, in general, combinations of the basic model responses already discussed. (See examples in figs. 22 and 23.) In figure 23, the data are averaged at the measurement station and one point per station indicates the mode shape. The combination responses shown do not exhibit well-defined longitudinal or lateral mode patterns or symmetrical tank responses.

Flight Times to Stage I Engine Burnout

The response-frequency plots for constant force input at $t = 40, 80, 120,$ and 152 sec are shown in figure 24. The ordinate is given in g units per pound (or per newton), where the acceleration is the output of sensors located at $x/l = 0, 0.324,$ and 1.00 and oriented so that the measurement axis of the accelerometer was parallel to the longitudinal axis of the model. Although the model response shows many resonances for the indicated flight times over the range of frequencies tested, few resonances in each response graph represent well-defined longitudinal mode shapes. The mode shapes corresponding to significant response peaks are shown in figure 25 for $t = 40$ sec, figure 26 for $t = 80$ sec, figure 27 for $t = 120$ sec, and figure 28 for $t = 152$ sec. Two characteristic modes in all patterns shown duplicate qualitatively the predominant longitudinal mode shapes observed previously for the fuel condition at stage I engine ignition ($t = 0$). Other mode shapes observed in this range of flight times are components of motion in the longitudinal direction due to coupling. These are omitted in the data presentation because identification of a basic response is not possible (e.g., see fig. 27(c)). Two exceptions are the longitudinal responses shown in figure 27(d) for $t = 120$ sec and figure 28(d) for $t = 152$ sec. These mode shapes are representative of a classical longitudinal third mode. Undoubtedly this mode is present at frequencies for flight times earlier than $t = 120$ sec, but it is probably distorted by coupling of tank and lateral modes that have been observed and discussed in the presentation of data for earlier flight times.

The four measurements shown at each station in the mode-shape plots correspond to response readings taken at each of four positions in order to permit interpolation when scattered data occurred in the overall mode shape. The data scatter that can be seen in the mode-shape figures illustrates the spurious effects which may be introduced by localized responses of the structure or longitudinal components of lateral motion superimposed on the basic longitudinal response of the model.

Data Summary

A review of the longitudinal mode shapes for all flight times indicates that only two mode shapes (the lowest frequency mode exhibiting one node and the mode with predominant payload response) are responses common to all propellant loading conditions of the model. For $t = 152$ sec, a pair of one-node responses was obtained. (See figs. 28(a) and 28(b).) The resonant frequencies of these modes for all the liquid-loading conditions are summarized in figure 29, where frequencies of the one- and two-node modes are plotted as functions of flight time t . (The two measured one-node mode frequencies for $t = 152$ sec are shown.) The frequency of the mode with one node increases with loss of fluid mass as expected; however, the mode with predominant payload motion (indicated by flagged symbols in fig. 29) is relatively unchanged over the entire flight history. The existence of the mode with predominant payload motion is due to the extremely flexible mounting of the payload, which permits the package and mounting to behave as a single-degree-of-freedom system. The mass portion of the payload oscillates on top of the body of the model, while the relatively stiffer and heavier model body undergoes small-amplitude motion. The presence of fluid mass in the stage I and stage II propellant tanks probably accounts for the second node line nearer the aft end of the model. When the fluid is completely removed from stage I, the model is still of sufficient mass (almost 25 times the payload mass) and stiffness to act as a rigid mounting on which the payload may oscillate. However, the second node line observed near the aft end of the model in earlier flight times is not present in this case ($t = 152$ sec). Since the regular one-node mode shape also was evident for the first-stage burnout condition ($t = 152$ sec), two mode shapes having one node were obtained.

At resonance, the displacement at various stations along the length of the model relative to the displacement at the point of excitation provides an interesting picture of the elastic behavior of the structure. An example of the longitudinal displacement transmissibility of the model is shown in figure 30, where the displacement throughout the structure relative to a normalized displacement at the engine gimbal points is indicated for three propellant loading conditions ($t = 0, 80,$ and 152 sec). These graphs represent the absolute displacement of different points along the model from the lowest frequency one-node modal patterns, each of which is normalized by the displacement at the gimbal points. As shown in the curves in figure 30, transmissibility decreases with decrease in

liquid propellant loading along the forward half of the model structure. For the extreme case ($t = 0$) a displacement of 1 unit at the engines (at the indicated resonance) magnifies to a displacement of about $5\frac{1}{2}$ units at the payload. The same normalization procedure applied to the payload modes for all propellant loading conditions indicates that a displacement of 1 unit at the gimbal point results in a displacement averaging $11\frac{1}{2}$ units at the payload for these flight times. This magnification is due for the most part to the payload structural design and illustrates the undesirable weight and stiffness combination of the payload structure.

Comparison of Measured and Computed Results

The resonant frequencies computed by using the component mathematical model are summarized for all propellant loading conditions in table 9. The frequencies shown are compared on the basis of similarity of the computed and measured mode shapes. The mode numbers in the table are a sequential order of the frequencies calculated by the component model analysis. The frequency data presented in this manner indicate the cases in which comparable experimental and calculated mode-shape data were obtained for a particular mode. In two instances resonances ($f = 41.2$ cps for $t = 0$ and $f = 59.5$ cps for $t = 40$ sec) were obtained for the component model without corresponding experimental mode shapes. Experimental resonances were measured at $f = 42.3$ cps for $t = 0$ (see fig. 22) and at $f = 53.2$ cps for $t = 40$ sec (data are not presented, but response is indicated in fig. 24(a)); however, the measured mode shapes are predominantly fuel-tank motion and do not compare with the calculated mode shapes which show predominant longitudinal motion with lesser tank response. In one case ($f = 55.2$ cps for $t = 152$ sec in table 9), an experimental resonance was measured (see fig. 28(a)), but no corresponding mode was calculated by the mathematical model. Aside from these discrepancies, the mathematical model predicted longitudinal response modes corresponding to experimental values as shown in table 9.

On the basis of the mode-shape comparison criterion used, the frequencies for all fluid loadings show reasonably good agreement for the two basic longitudinal structural modes. Calculated and measured mode shapes are presented in figure 31 for $t = 0$, figure 32 for $t = 40$ sec, figure 33 for $t = 80$ sec, figure 34 for $t = 120$ sec, and figure 35 for $t = 152$ sec. A comparison of the calculated and experimental mode shapes of the two basic structural longitudinal modes showed, in general, good agreement. In the two cases of mode-shape comparison for the highest resonant frequency at $t = 120$ sec (fig. 34(c)) and $t = 152$ sec (fig. 35(c)), however, there is poor agreement between computed and measured data.

TABLE 9.- MEASURED AND COMPUTED FREQUENCIES

t, sec	Frequency, cps, for -									
	Mode 1		Mode 2		Mode 3		Mode 4		Mode 5	
	Measured	Computed	Measured	Computed	Measured	Computed	Measured	Computed	Measured	Computed
0	39.7	36.7	---	41.2	63.5	62.5	74.7	79.2	-----	-----
40	41.6	41.7	---	59.5	63.8	63.9	----	----	-----	-----
80	44.4	46.4	---	----	63.4	64.6	----	----	-----	-----
120	50.3	53.2	---	----	64.1	66.3	----	----	94.4	109.8
152	55.2	----	---	----	63.3	60.8	80.0	81.4	110.0	111.3

CONCLUDING REMARKS

A scaled model of a liquid-propellant multistage launch vehicle was subjected to forced vibration in the longitudinal direction in a frequency range from approximately 10 to 100 cps. The model structure was supported in a suspension system that offered negligible restraint to longitudinal motion and the vibration response was measured for selected fluid-propellant loading conditions representing different fluid loadings ranging from stage I engine ignition to burnout. Measured resonant frequencies and mode shapes of the model are presented. In addition, the vibration response of the model was computed by using a two-dimensional mathematical model which consisted of a series of axisymmetric shell, spring-mass, and fluid components. Computed results are presented and compared with experimental data.

An extensive investigation of the model vibration response for the propellant condition at stage I ignition revealed a complex response of the model to longitudinal excitation that consisted of lateral (pitch and yaw) and radial tank motions, as well as the longitudinal responses. In the frequency range tested, only two basic structural longitudinal modes were common to all propellant loading conditions.

Computations of the longitudinal natural frequencies and mode patterns by using a finite-element mathematical model of the structure indicates that the analysis adequately predicts the two modes which denote the basic longitudinal structural vibration response of the model. Prediction by the analysis is limited to these two modes because of the complexity of the response of the model and the limitation of the mathematical model in predicting only axisymmetric response.

For longitudinal vibration analysis it is felt that, regardless of the sophistication of analytical procedures utilized, it is presently highly desirable to employ extensive

experimental model vibration data to assure the development of an adequate mathematical model.

Langley Research Center,
National Aeronautics and Space Administration,
Langley Station, Hampton, Va., December 16, 1966,
124-11-05-24-23.

REFERENCES

1. Mixson, John S.; Catherine, John J.; and Arman, Ali: Investigation of the Lateral Vibration Characteristics of a 1/5-Scale Model of Saturn SA-1. NASA TN D-1593, 1963.
2. Catherine, John J.: Torsional Vibration Characteristics of a 1/5-Scale Model of Saturn SA-1. NASA TN D-2745, 1965.
3. Mixson, John S.; and Catherine, John J.: Comparison of Experimental Vibration Characteristics Obtained From a 1/5-Scale Model and From a Full-Scale Saturn SA-1. NASA TN D-2215, 1964.
4. Jaszlics, Ivan J.; and Morosow, George: Dynamic Testing of a 20% Scale Model of the Titan III. AIAA Symposium on Structural Dynamics and Aeroelasticity, Aug.-Sept. 1965, pp. 477-485.
5. Archer, J. S.; and Rubin, C. P.: Improved Analytic Longitudinal Response Analysis for Axisymmetric Launch Vehicles. Volume I - Linear Analytic Model. NASA CR-345, 1965.
6. Mechtly, E. A.: The International System of Units - Physical Constants and Conversion Factors. NASA SP-7012, 1964.
7. Rubin, C. P.; and Wang, T. T.: Improved Analytic Longitudinal Response Analysis for Axisymmetric Launch Vehicles. Volume II - Computer Program Description. NASA CR-346, 1965.

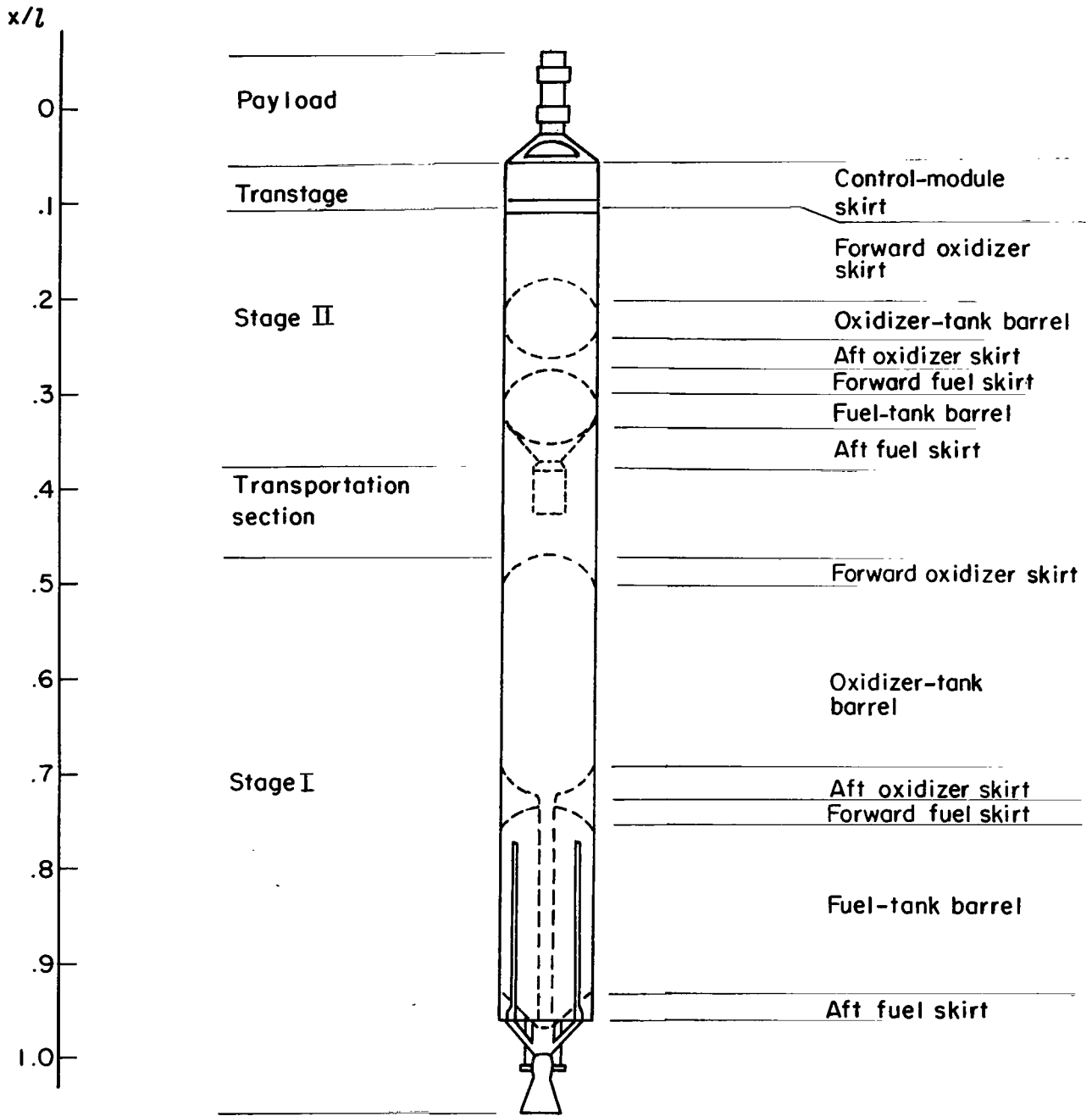


Figure 1.- Model configuration and major components.

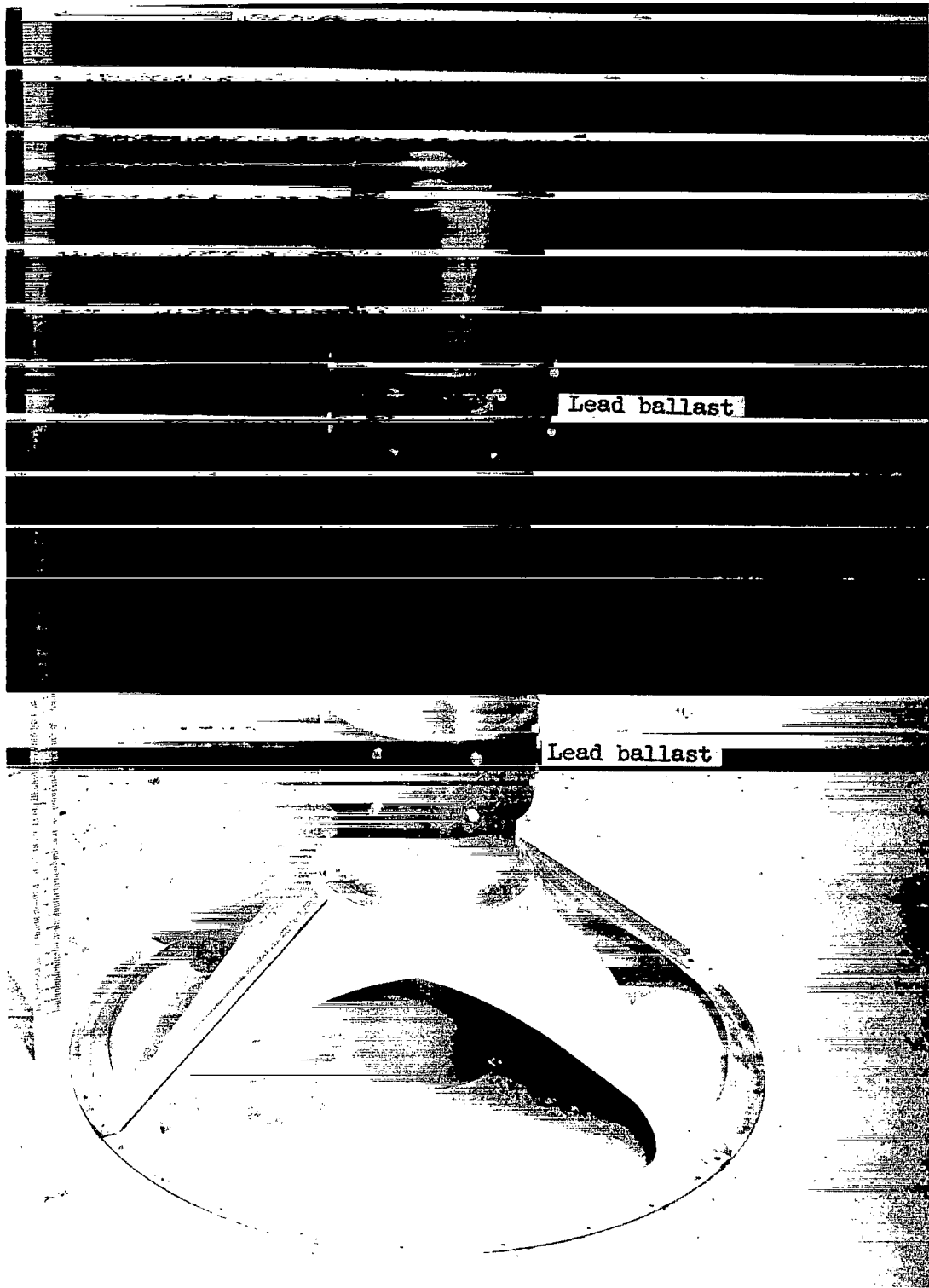


Figure 2.- Payload.

L-67-934

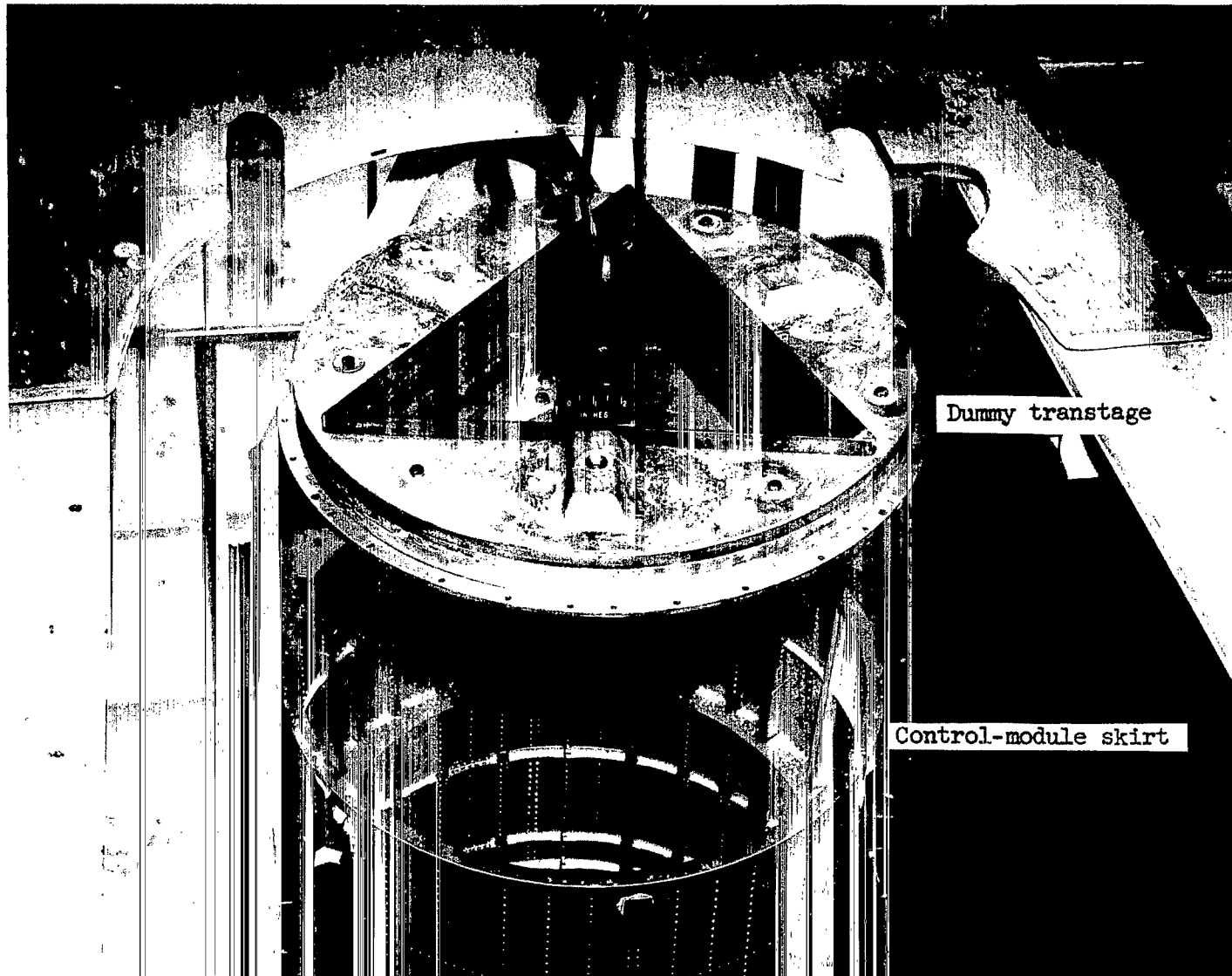


Figure 3.- Transtage simulation.

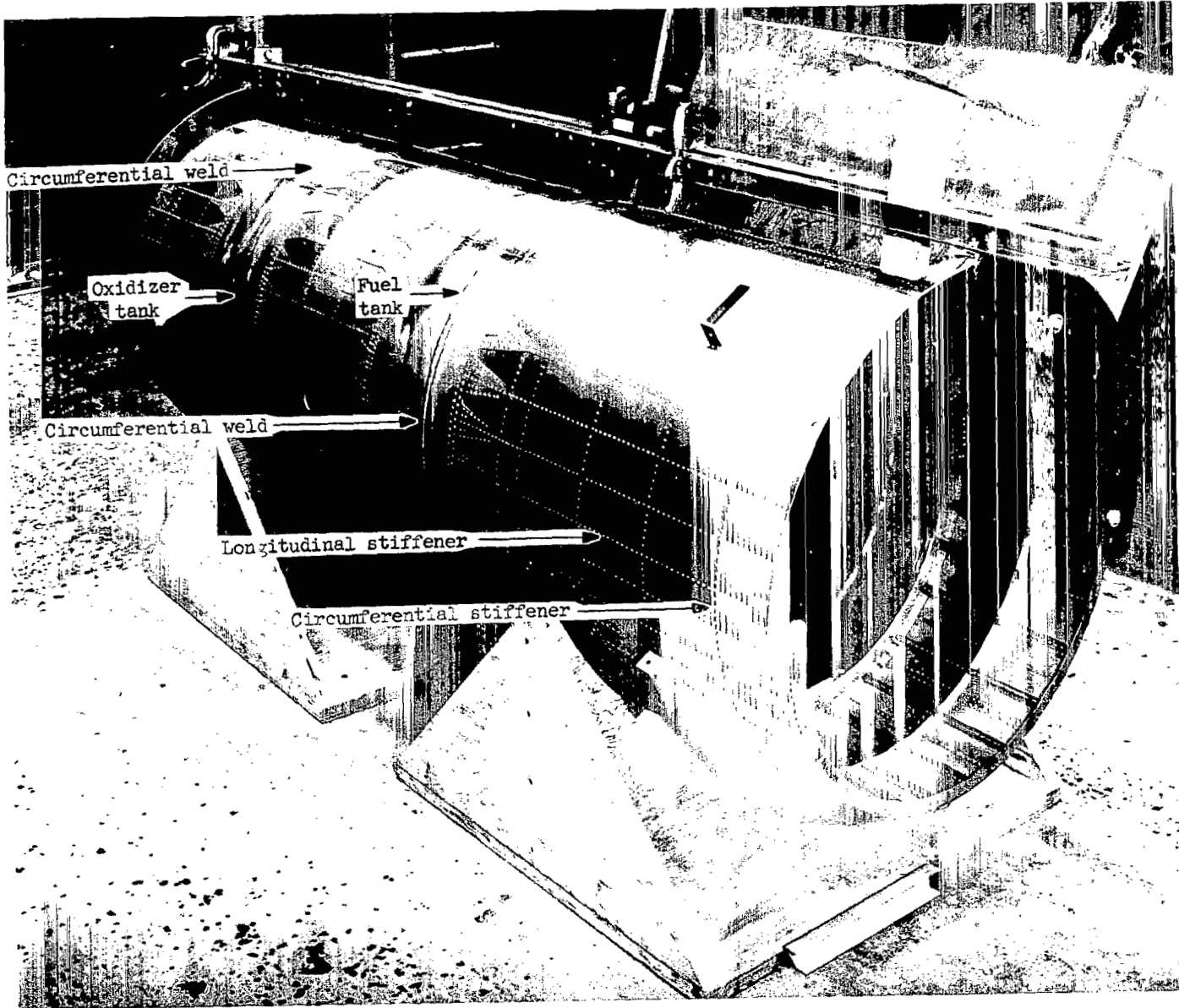


Figure 4.- Stage II.

L-67-935

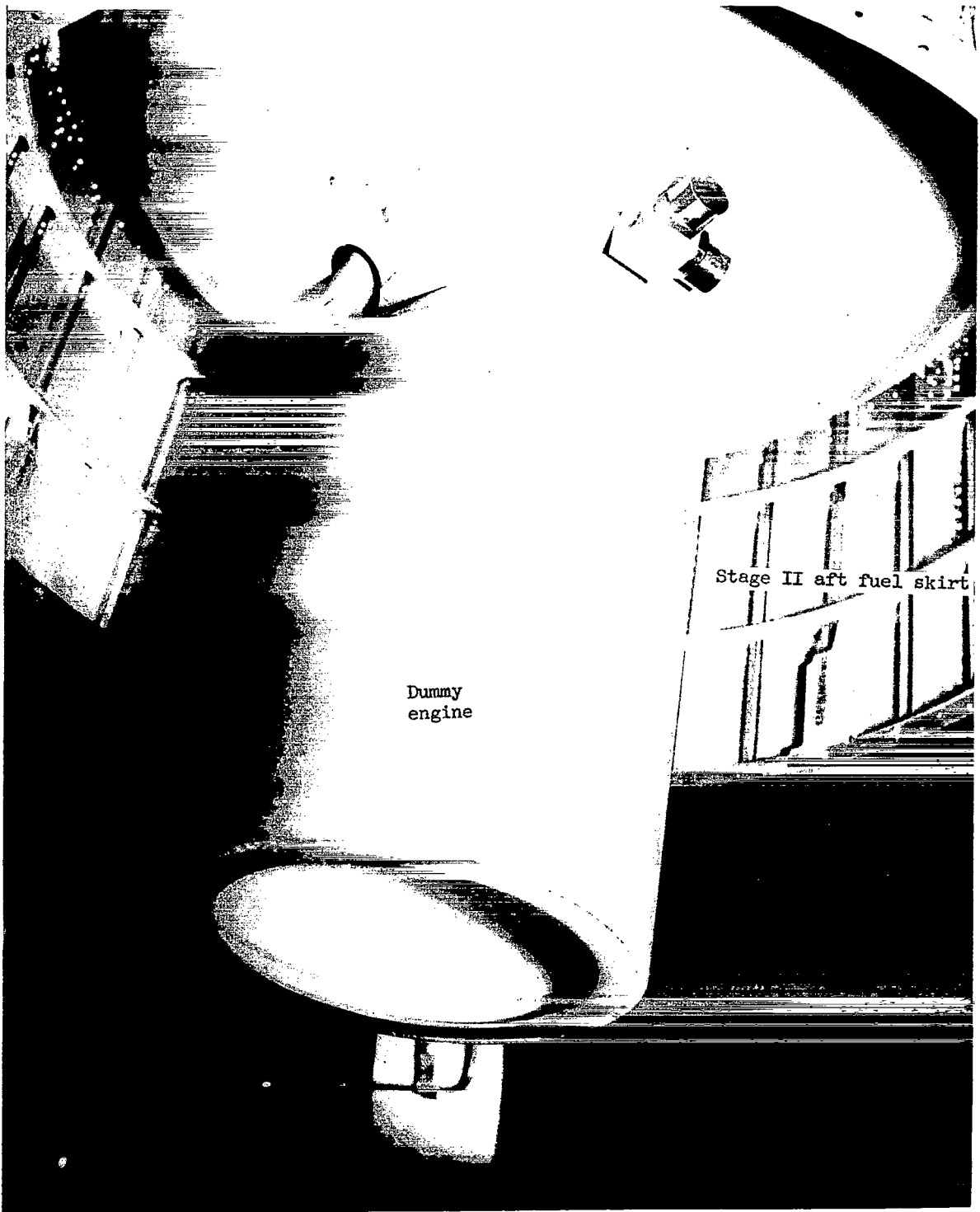


Figure 5.- Stage II single engine simulation.

L-64-3358.1

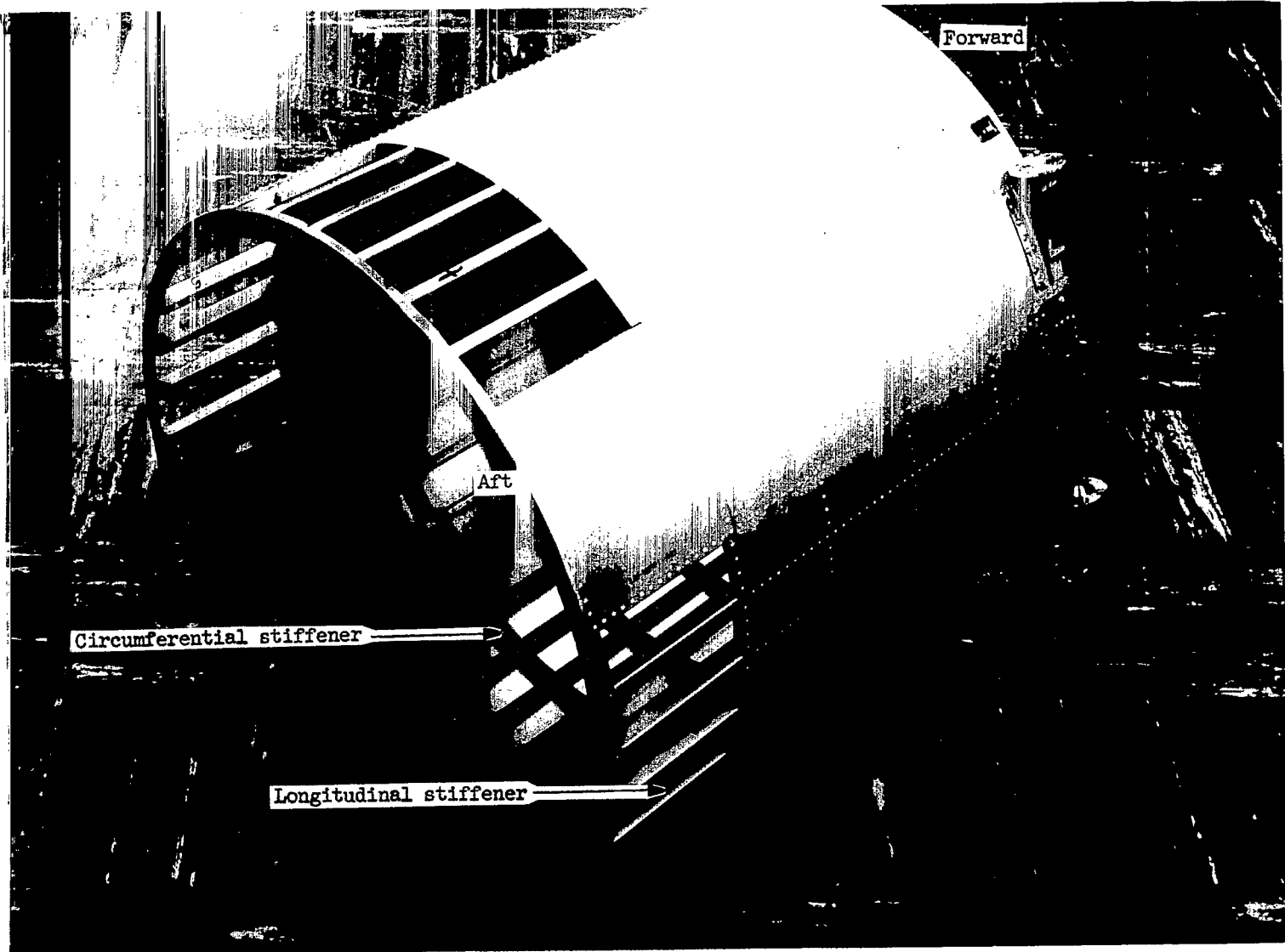


Figure 6.- Transportation section.

L-67-936

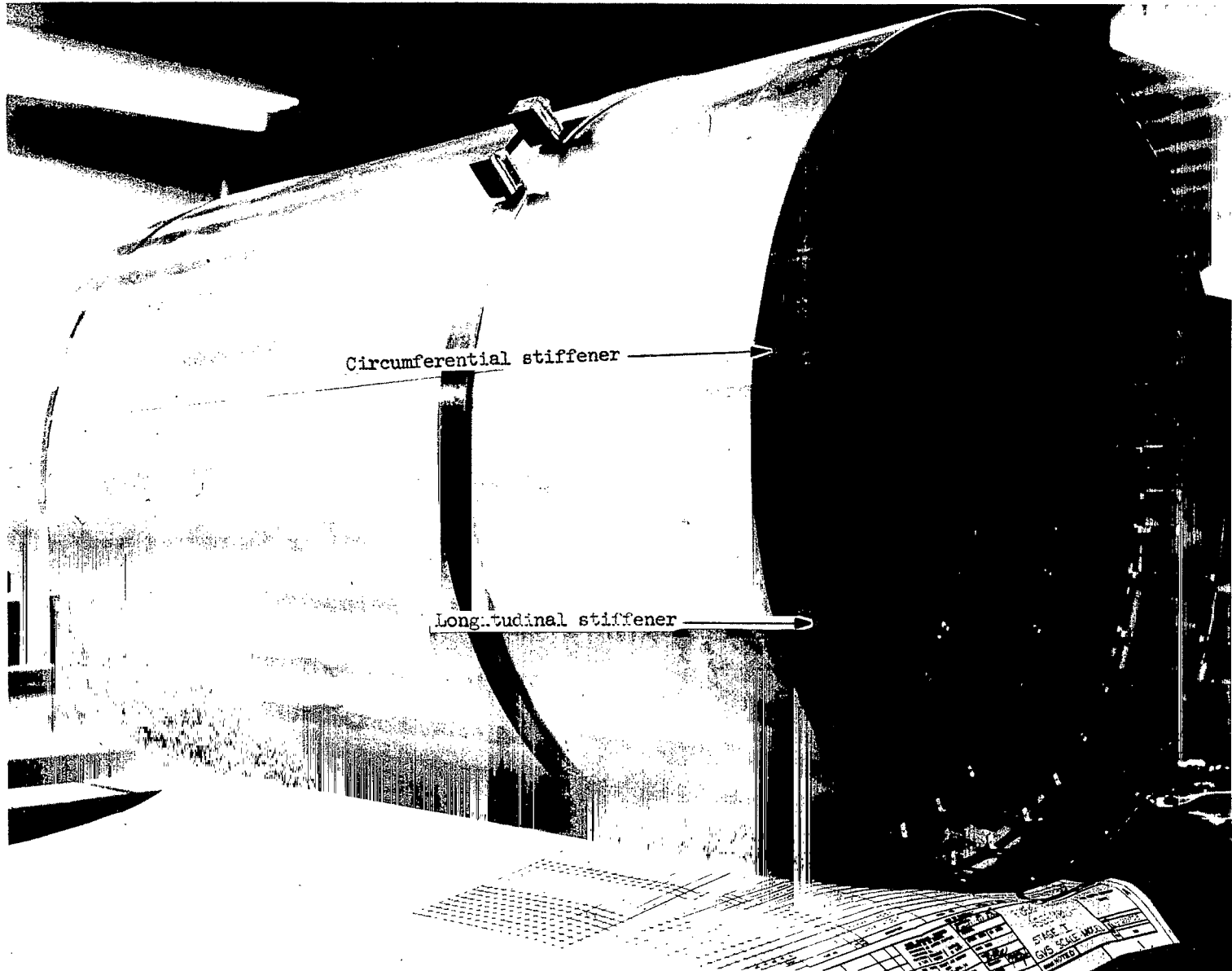


Figure 7.- Stage I fuel tank (during construction).

Aft oxidizer skirt

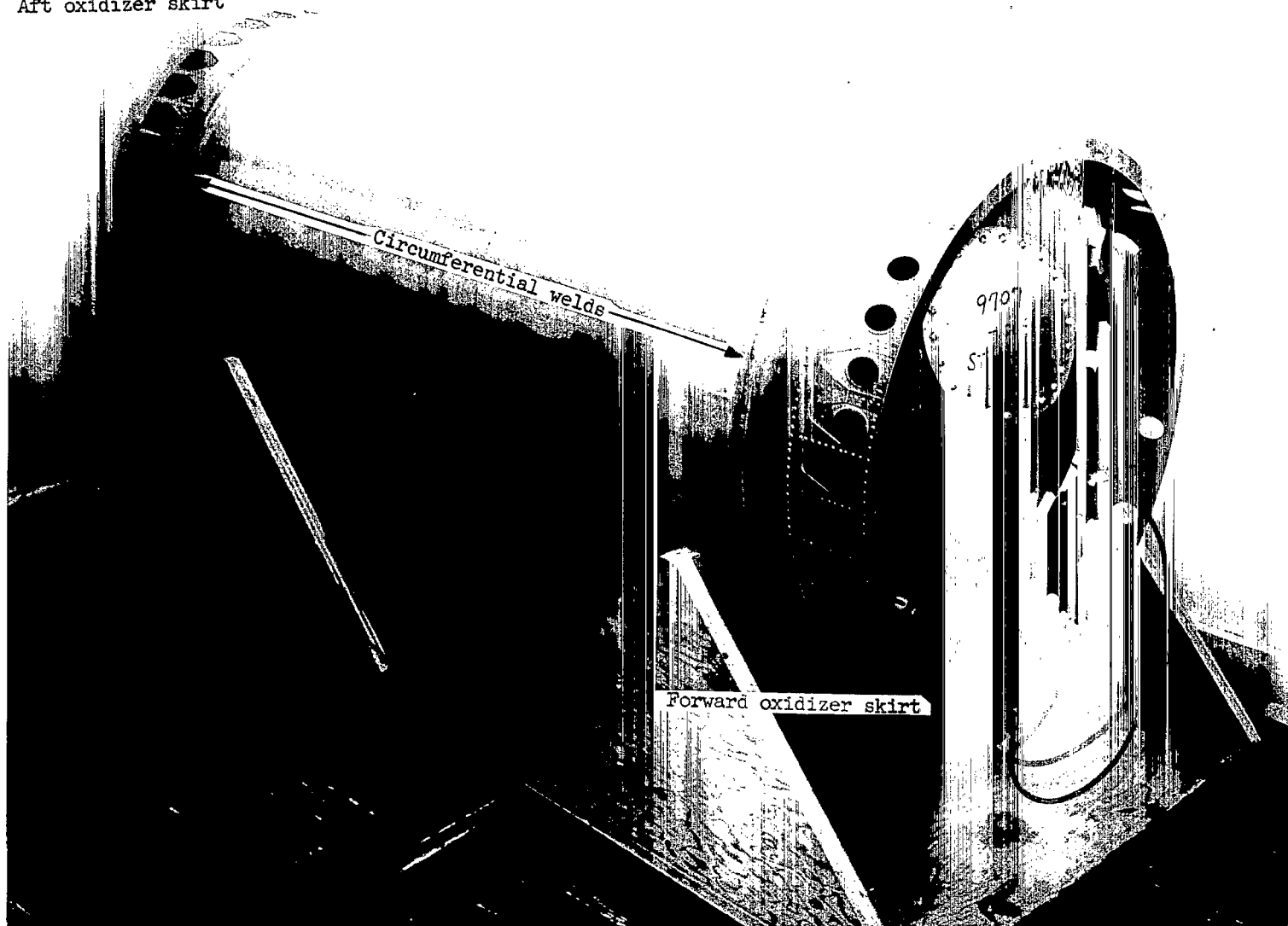


Figure 8.- Stage I oxidizer tank.

L-67-938



Figure 9.- Stage I oxidizer transfer tube.

L-67-939

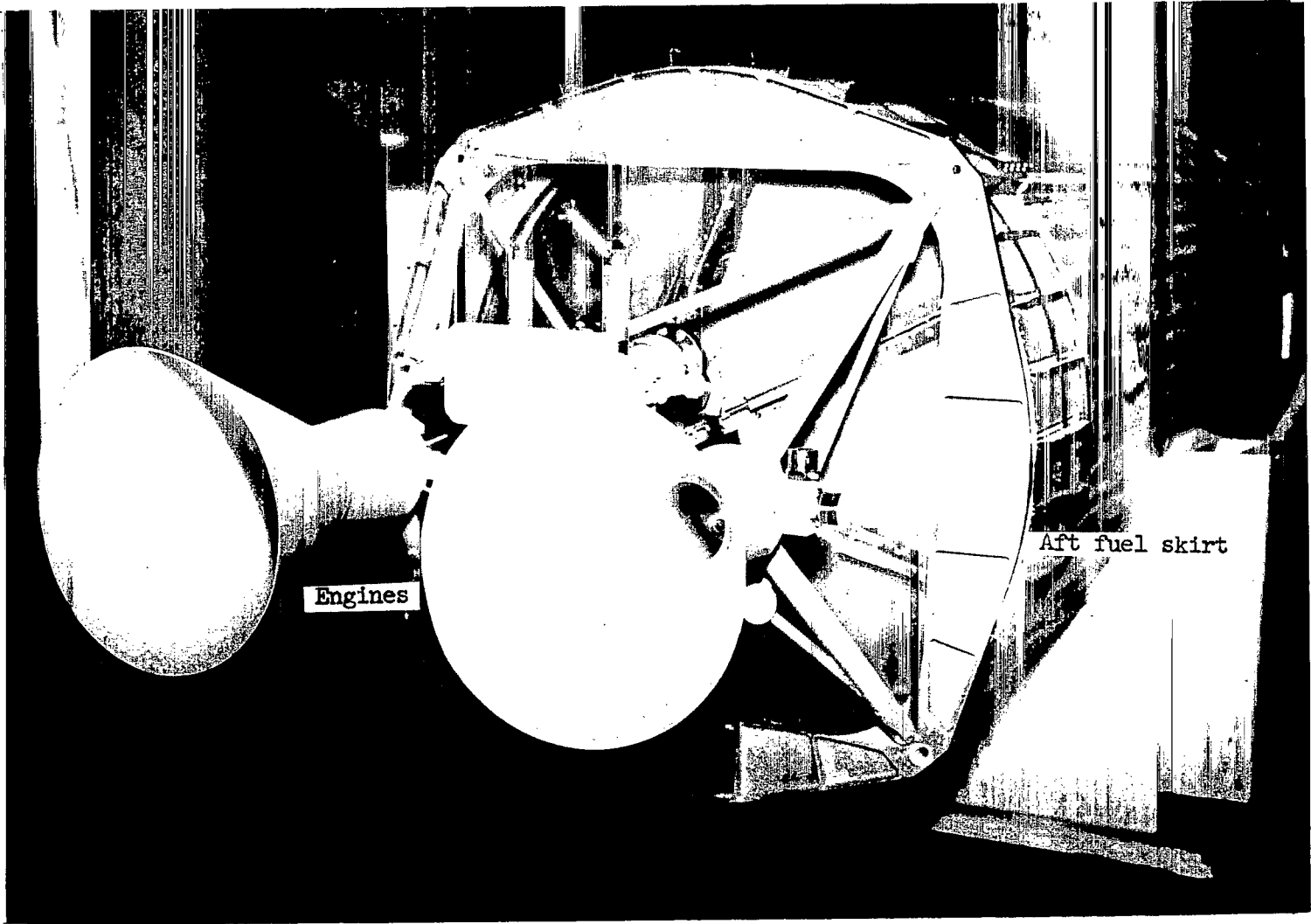


Figure 10.- Stage 1 engines.

L-64-3360.1

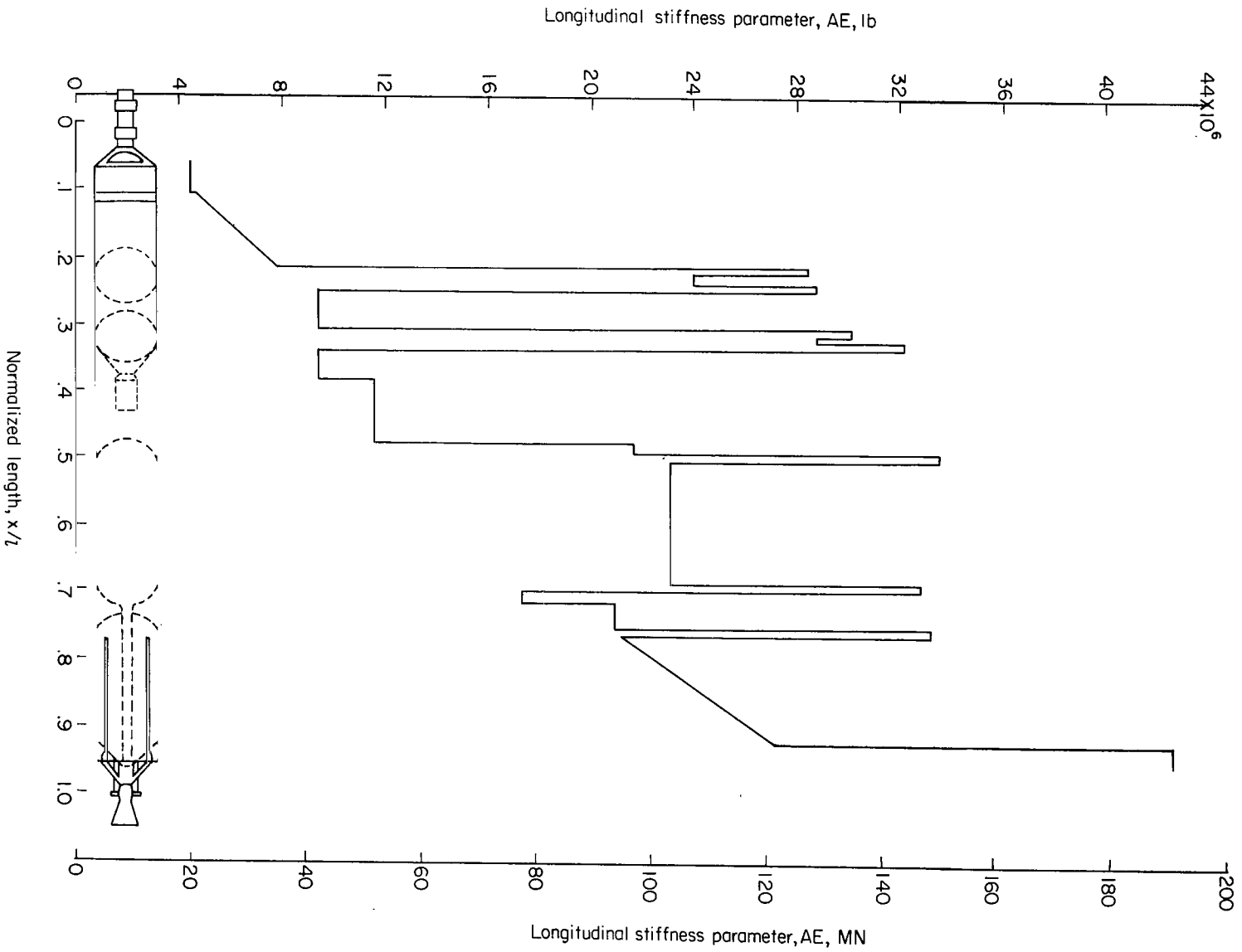


Figure 11.- Longitudinal-stiffness-parameter distribution.

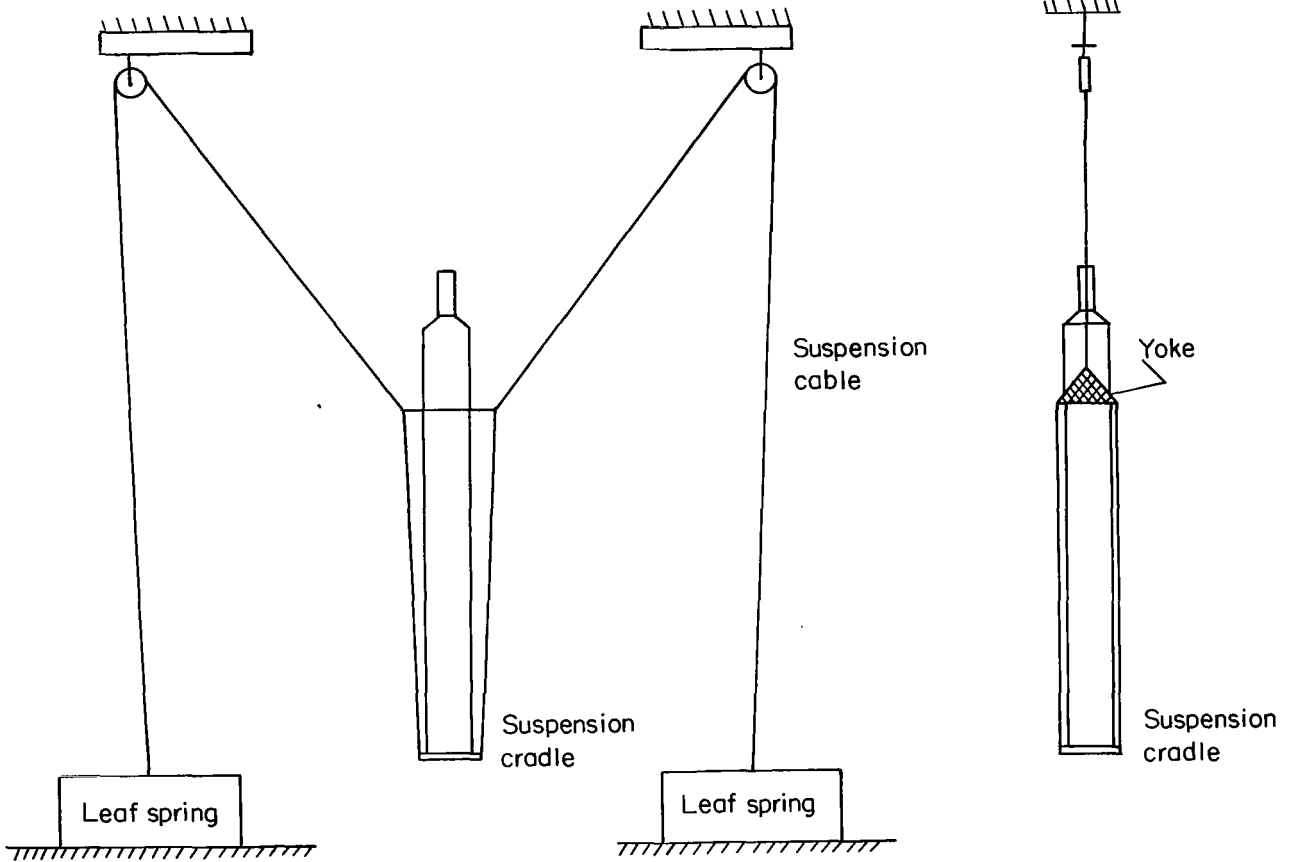


Figure 12.- Suspension system.

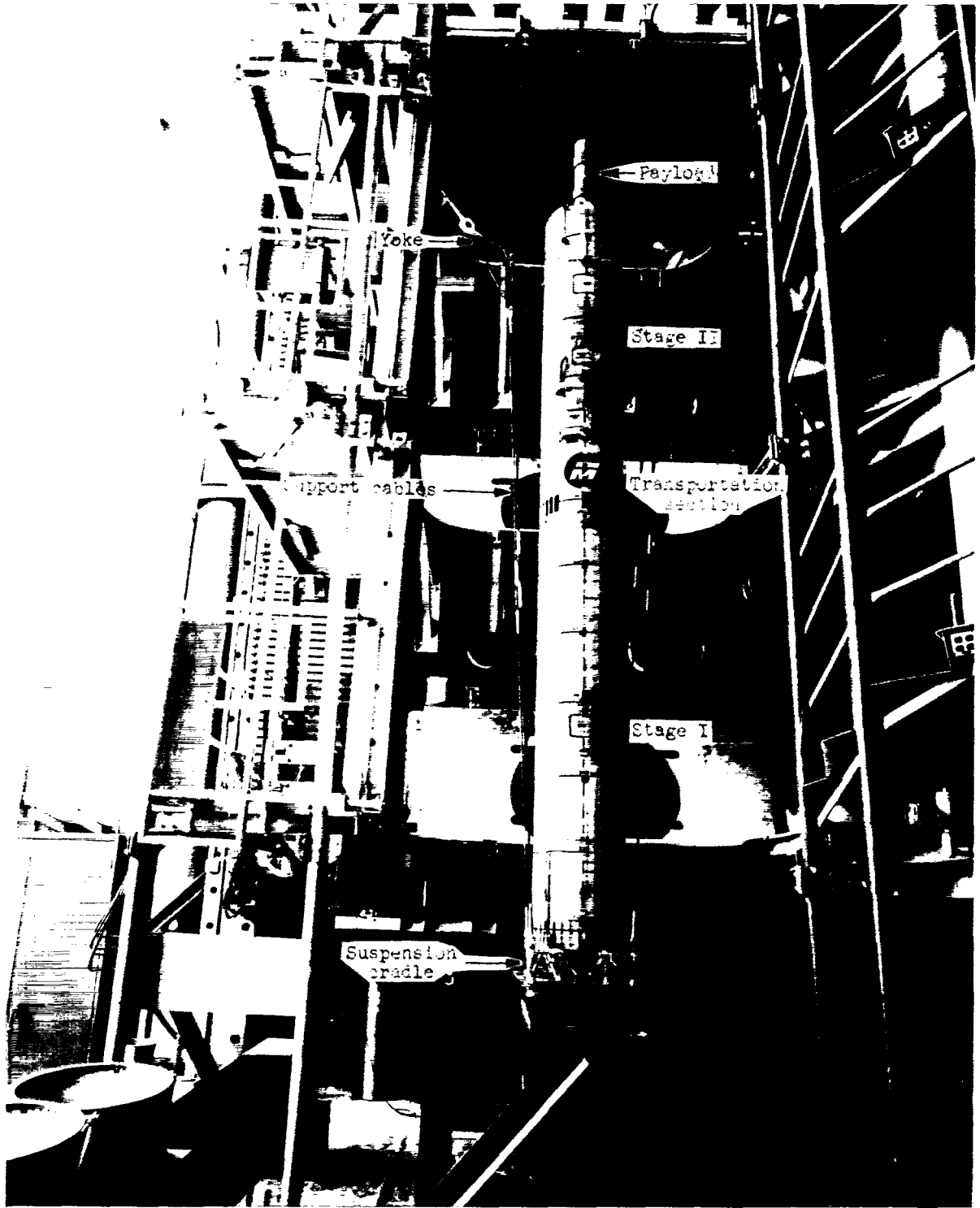


Figure 13.- Model in suspension system prior to test.

L-65-3934.2

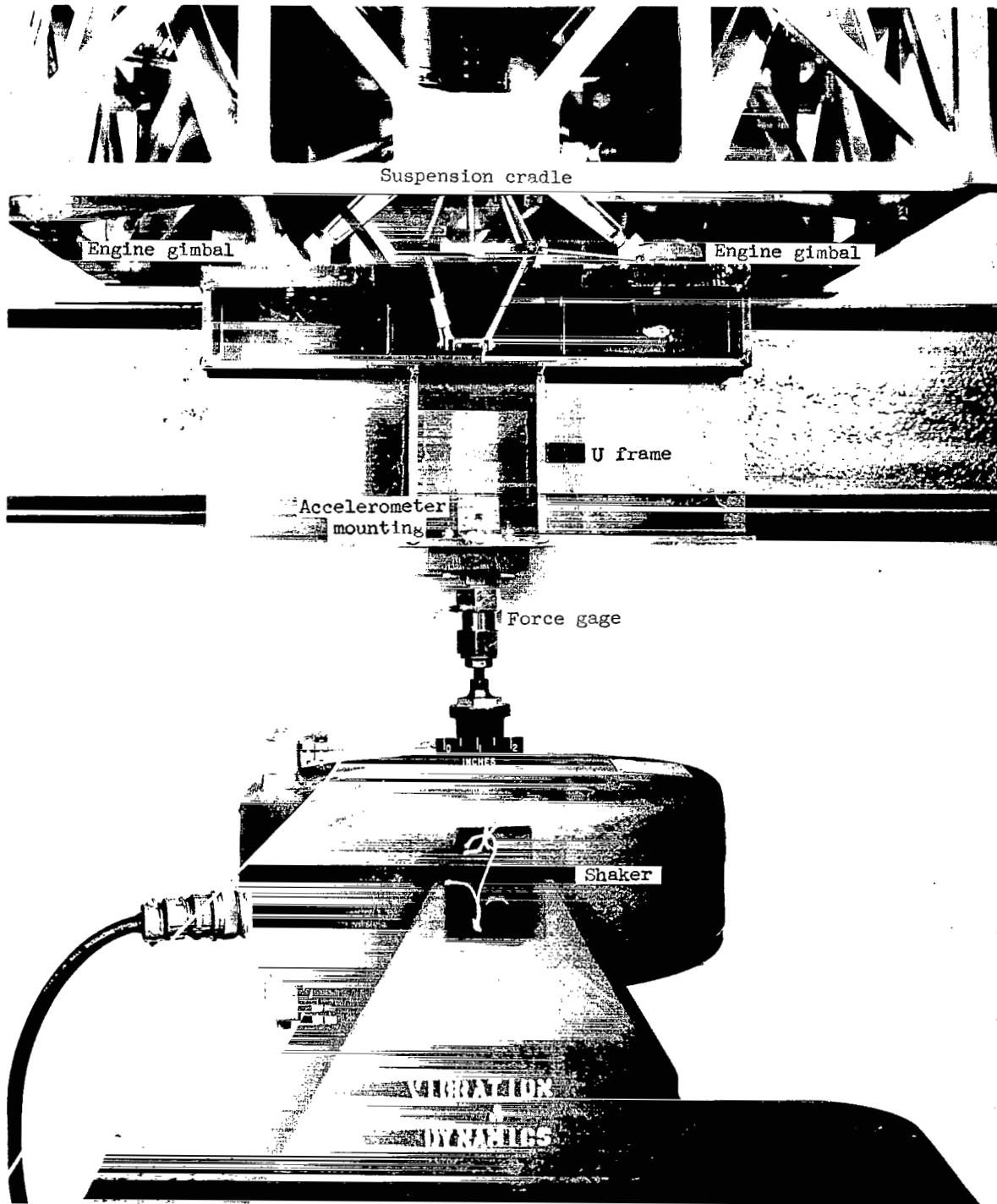


Figure 14.- Electromagnetic shaker and attachment linkage.

L-65-3935.1

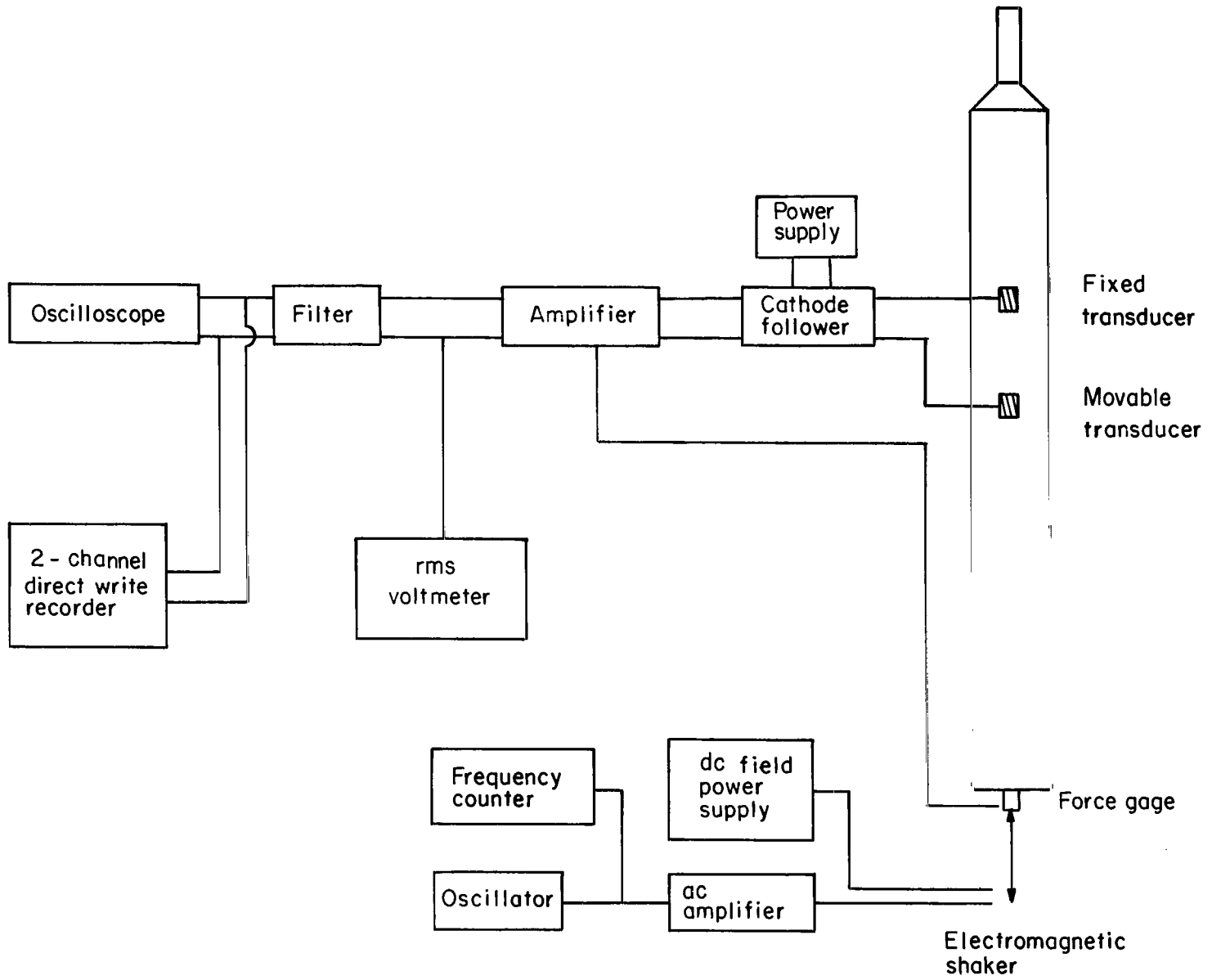


Figure 15.- Diagram of instrumentation system.

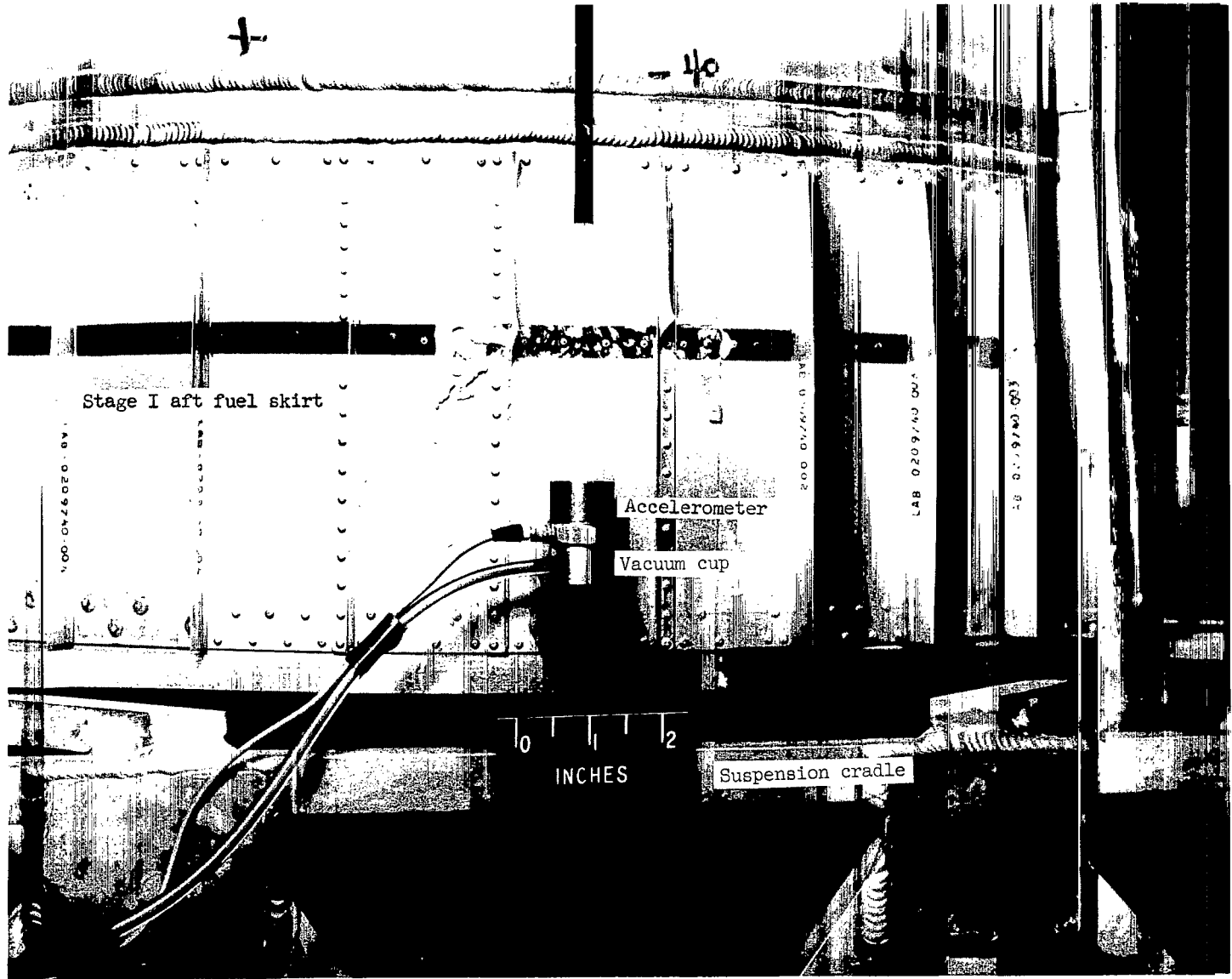


Figure 16.- Typical mounting of movable accelerometer.

L-65-3936.1

Component
 ○ Shell } Number in symbol identifies each component.
 □ Mass }
 ▽ Fluid } Negative number denotes a double-curvature shell.
 ▽ System coordinate locations.

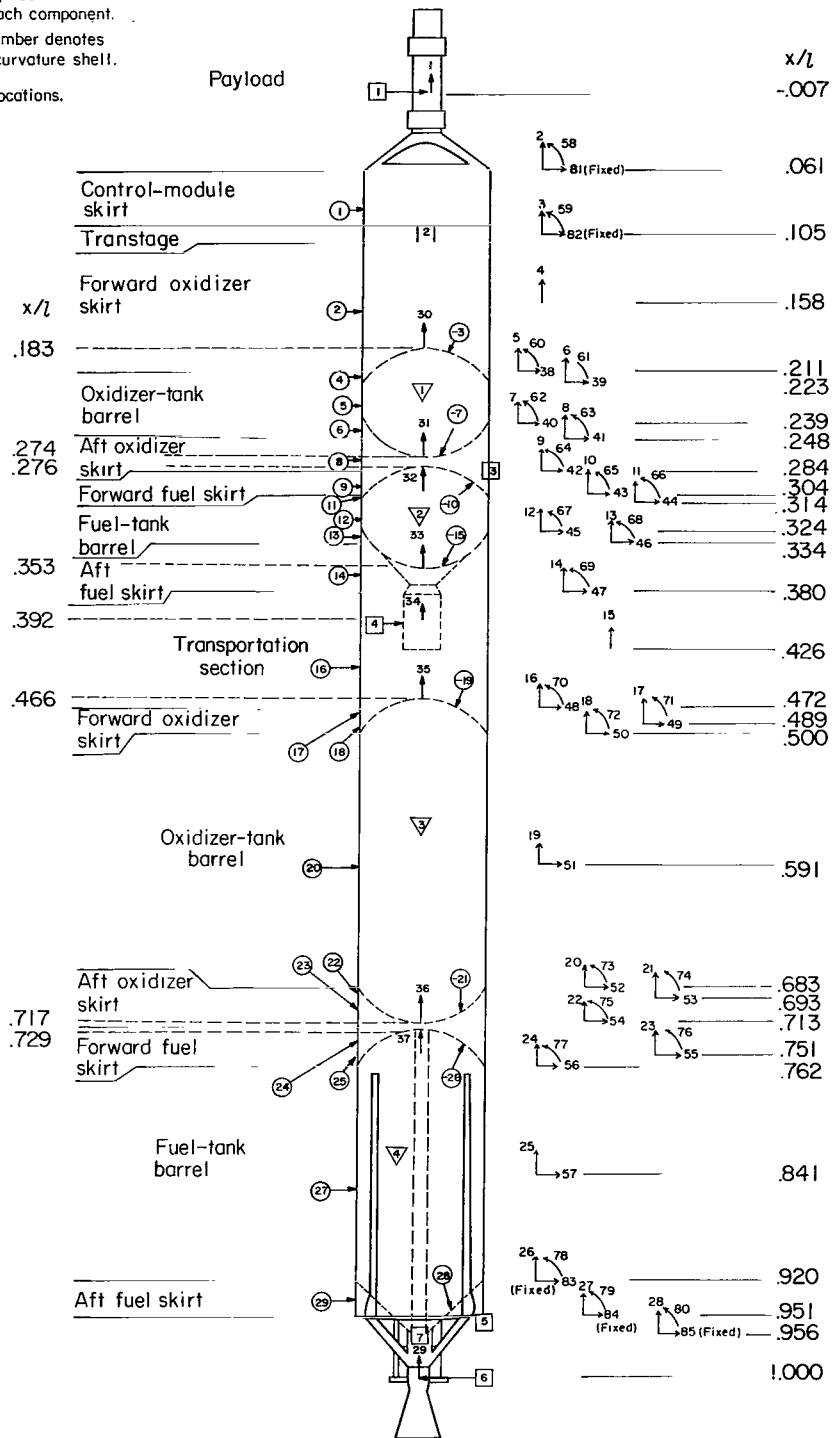


Figure 17.- Shell, fluid, mass, and system coordinate identification.

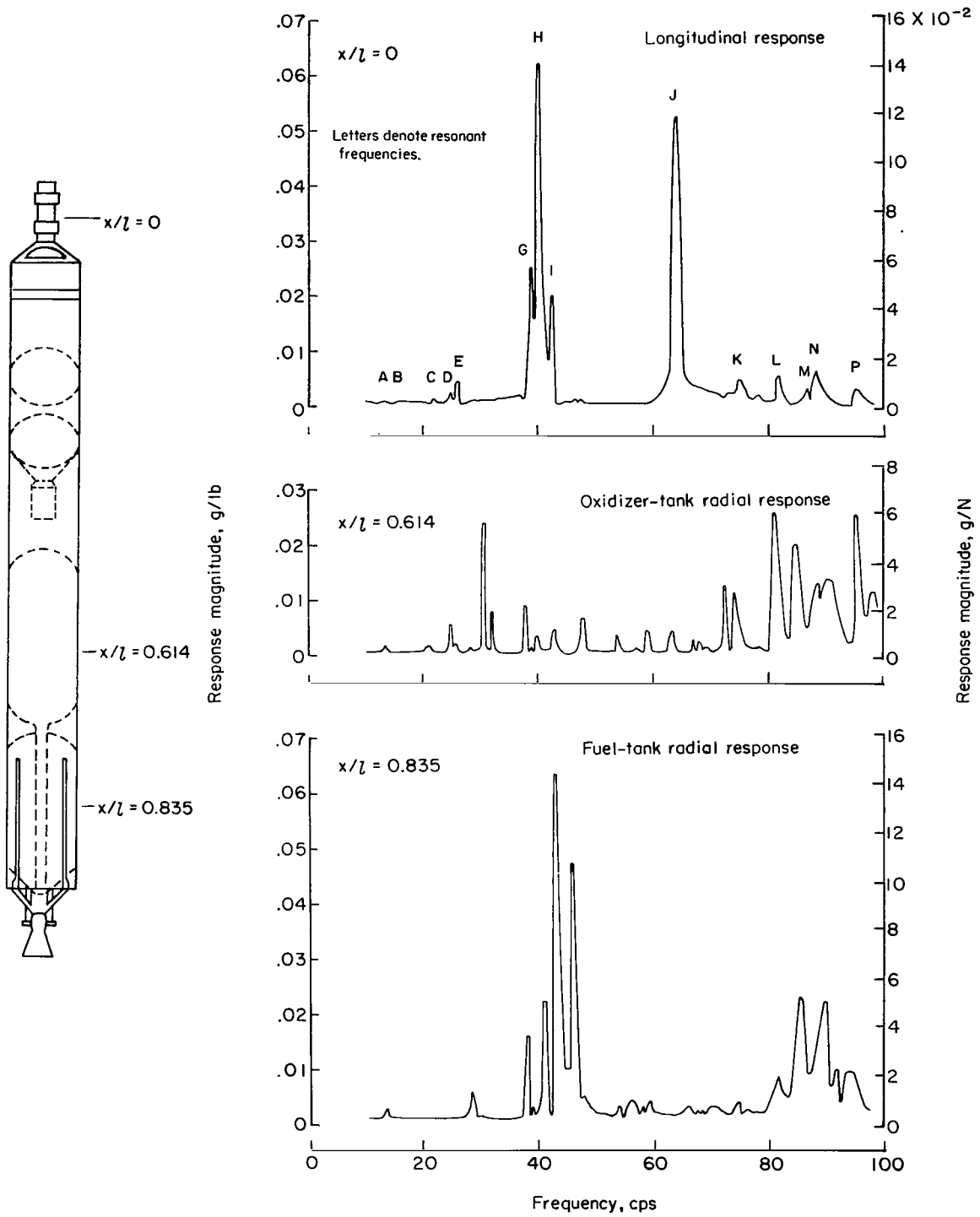


Figure 18.- Longitudinal and tank radial response for longitudinal excitation ($t = 0$).

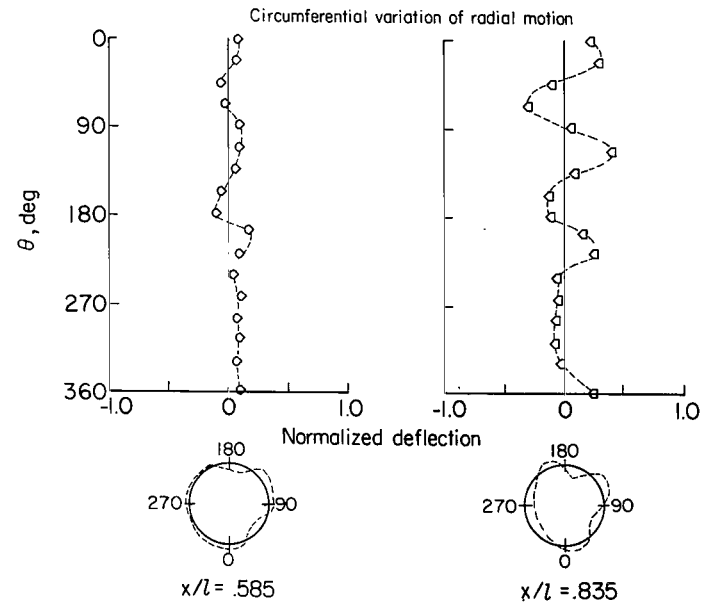
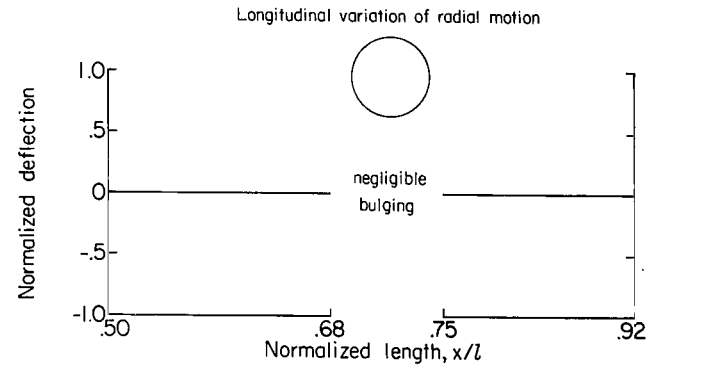
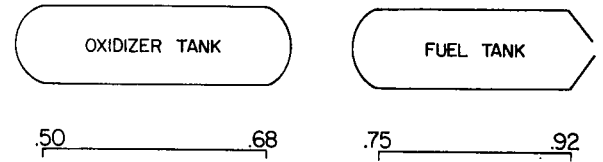
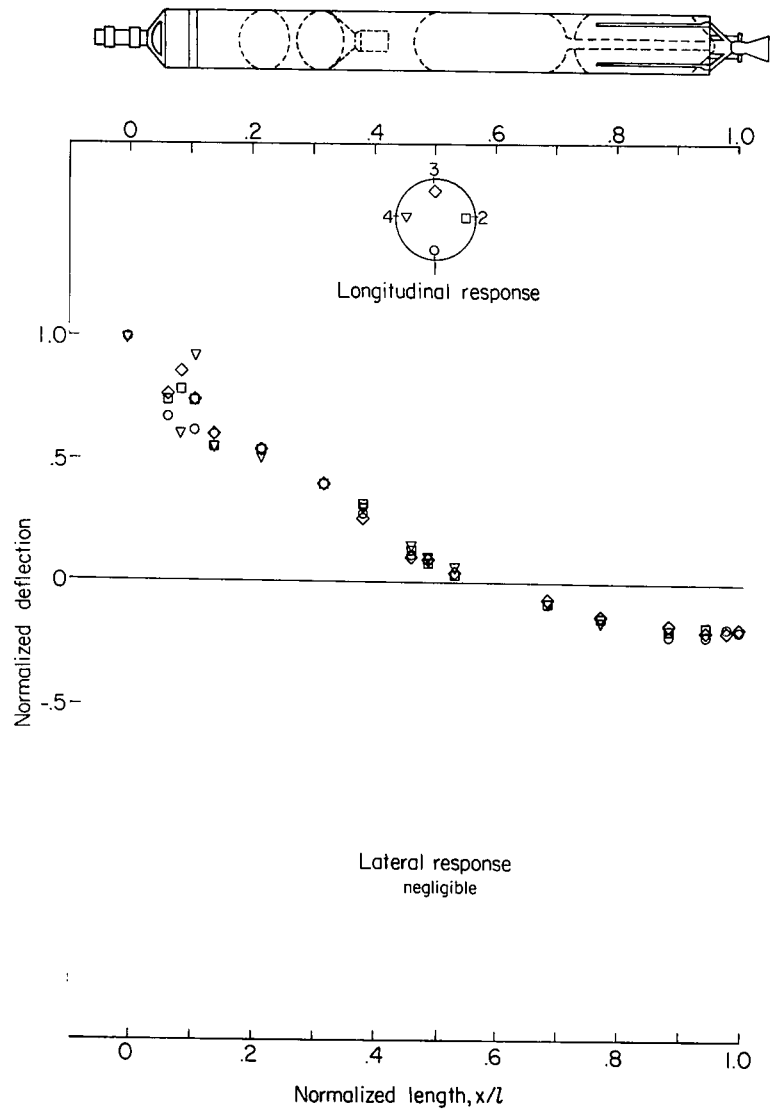


Figure 19.- Measured modal response normalized to longitudinal deflection at $x/l = -0.007$. $t = 0$; $f = 39.7$ cps.

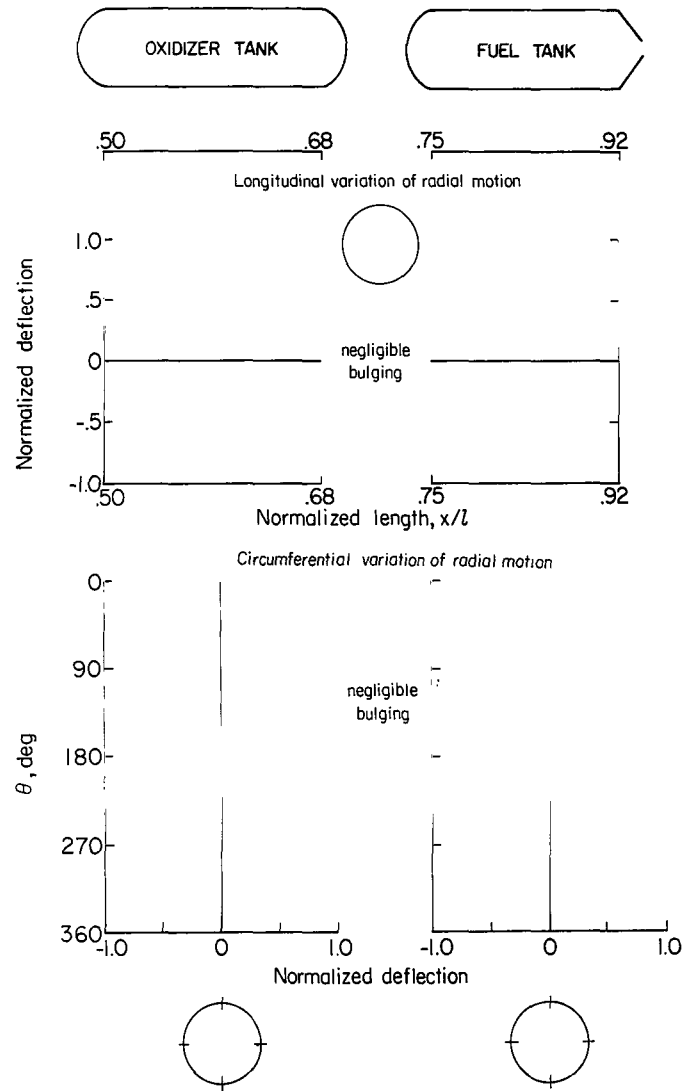
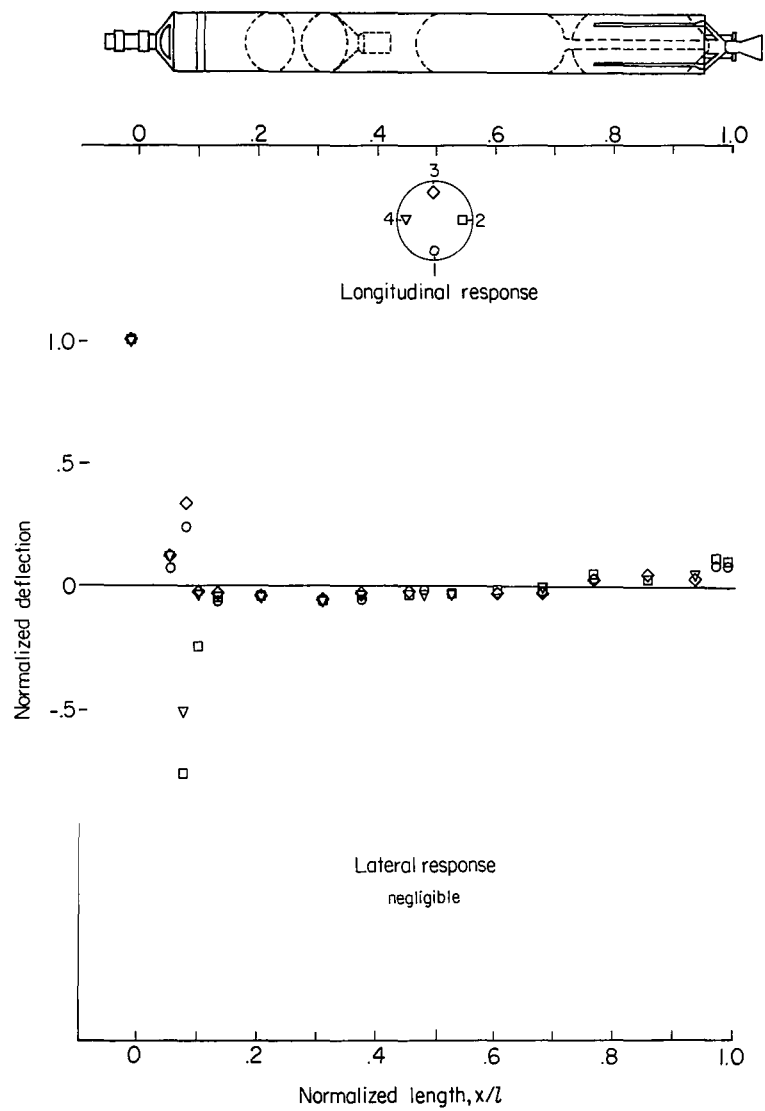
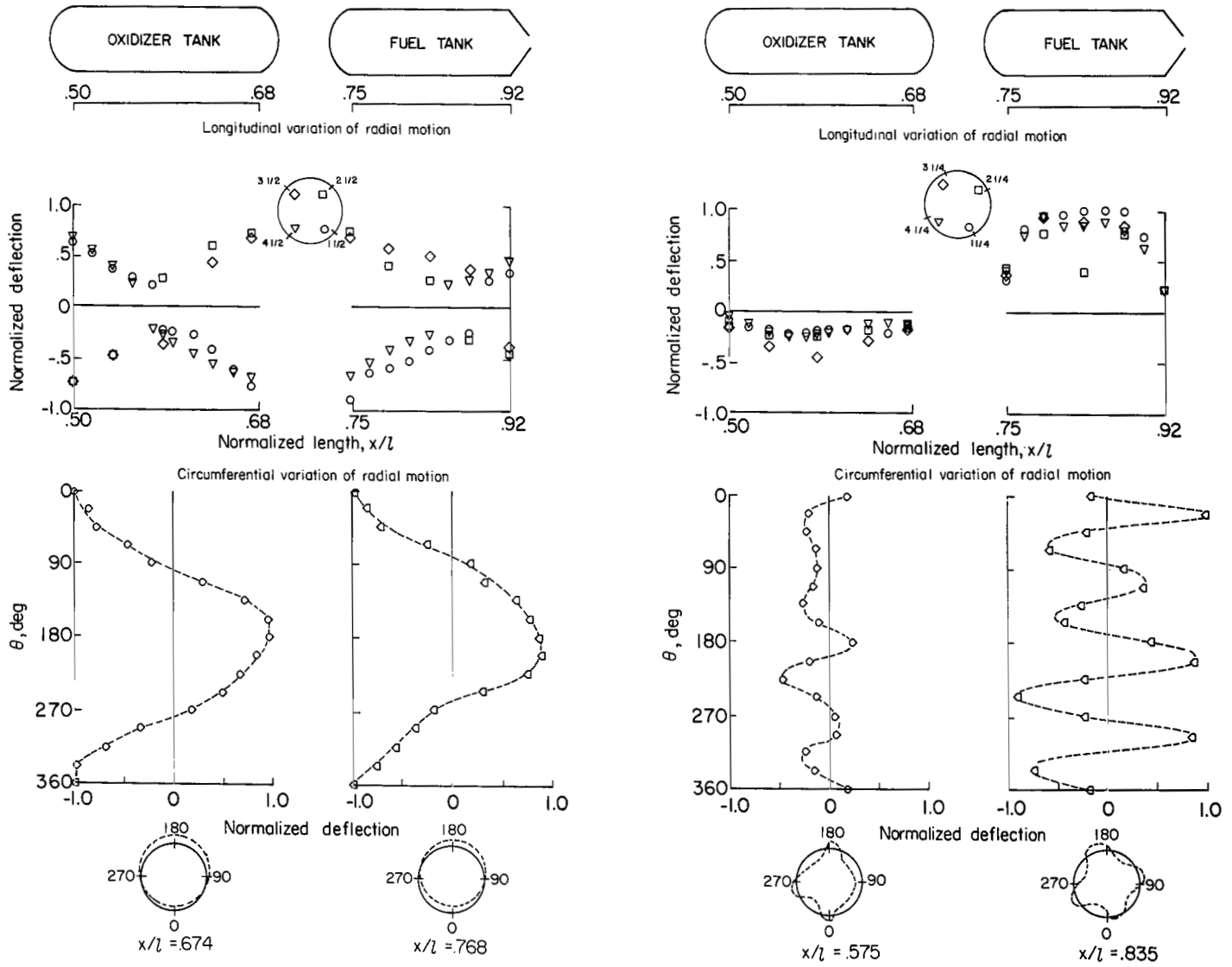


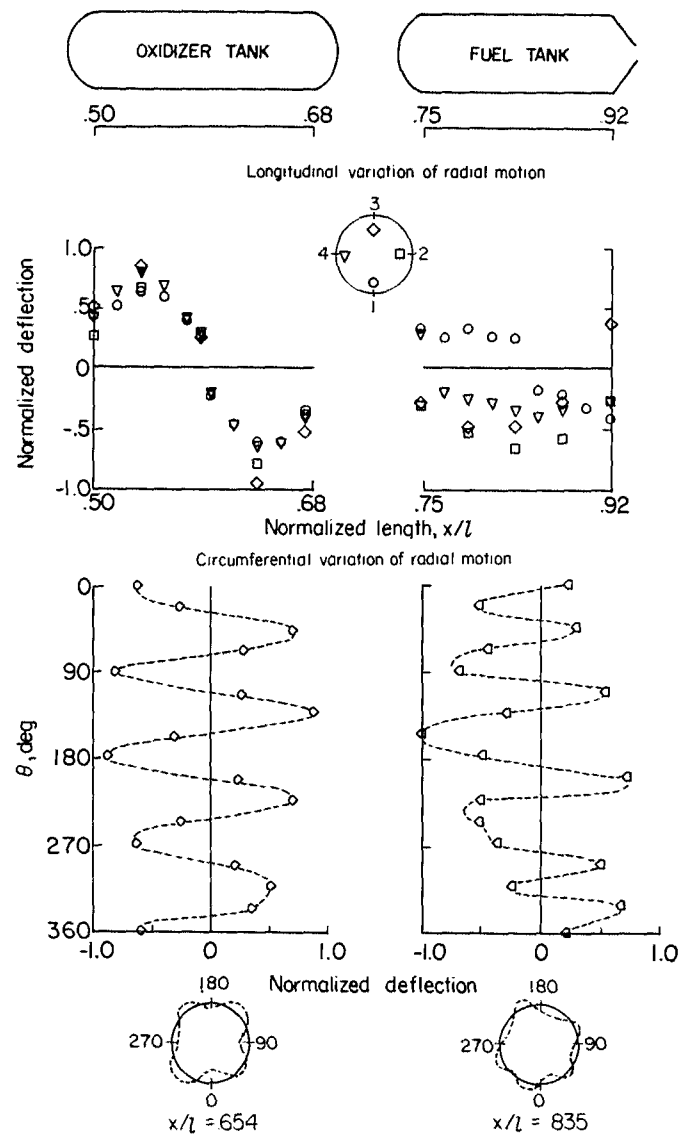
Figure 20.- Measured modal response normalized to longitudinal deflection at $x/l = -0.007$. $t = 0$; $f = 63.5$ cps.



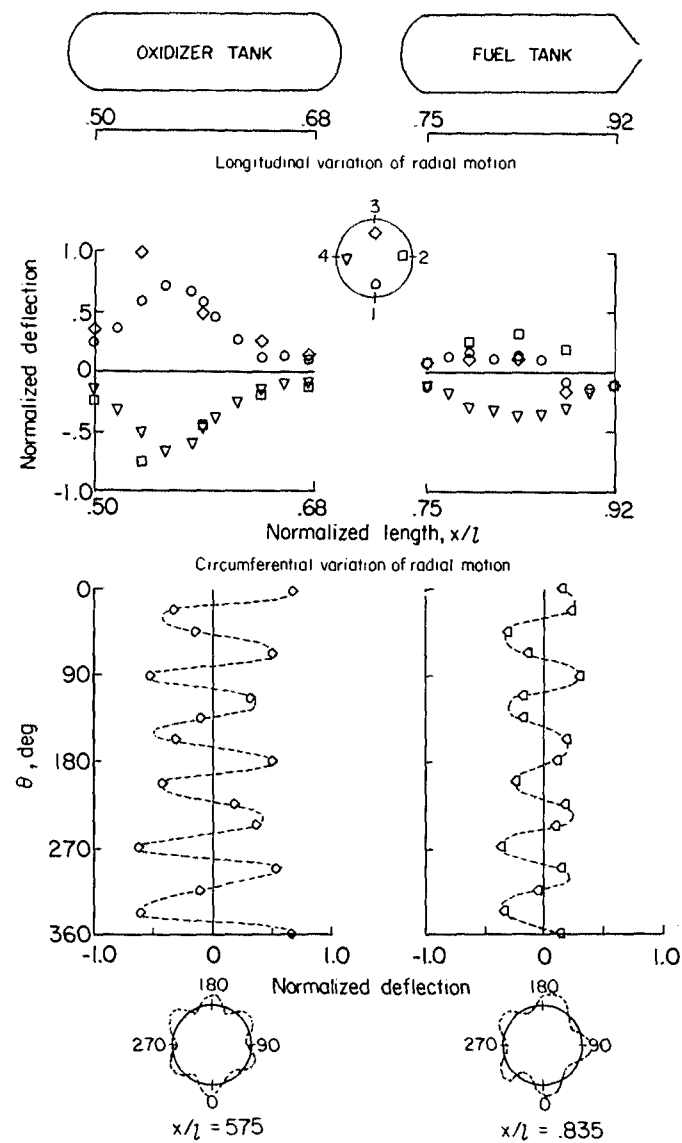
(a) $f = 37.8$ cps.

(b) $f = 42.7$ cps.

Figure 21.- Longitudinally excited radial response of tank normalized to maximum deflection at each frequency. $t = 0$.



(c) $f = 45.7$ cps.



(d) $f = 47.6$ cps.

Figure 21.- Continued.

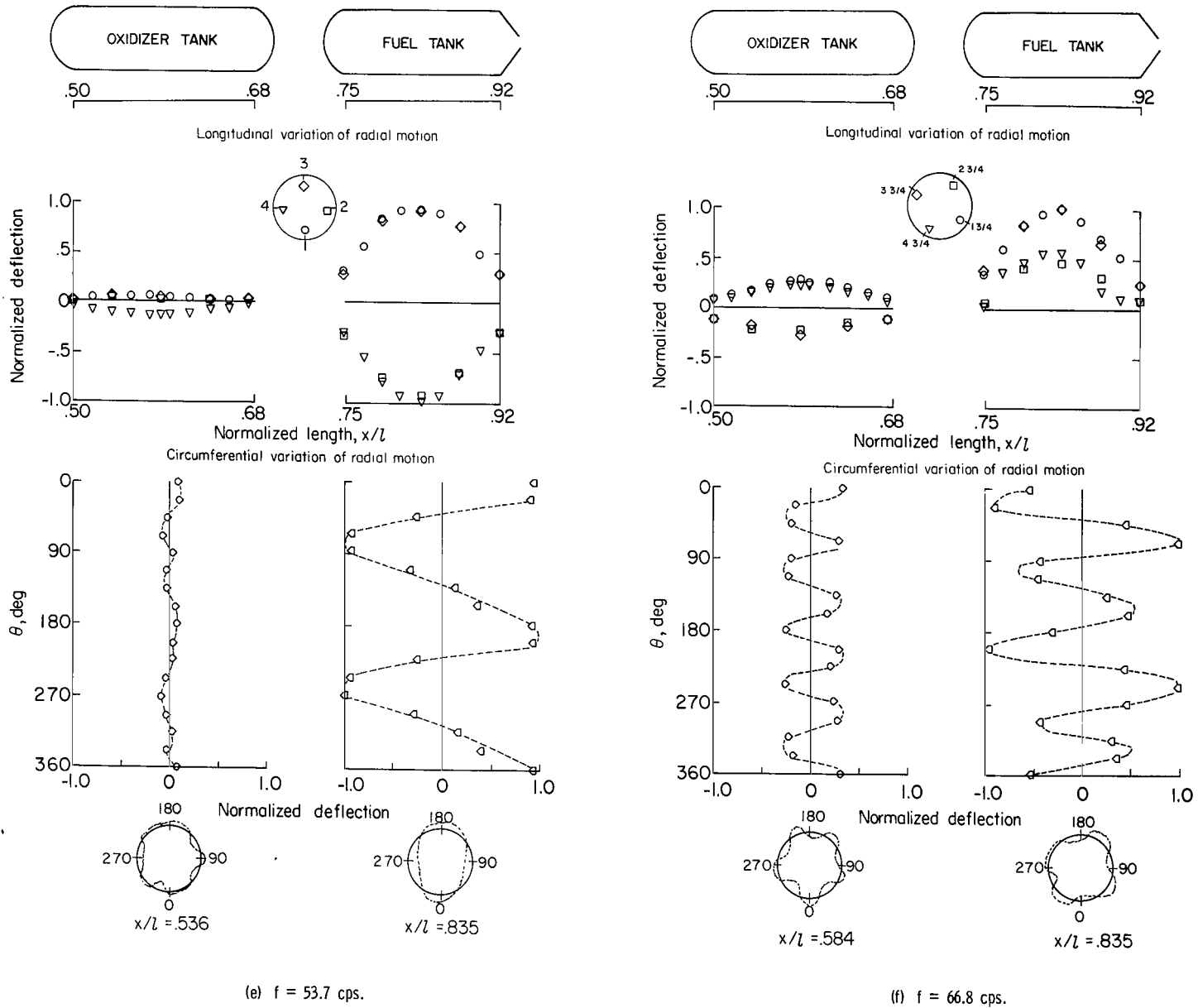


Figure 21.- Concluded.

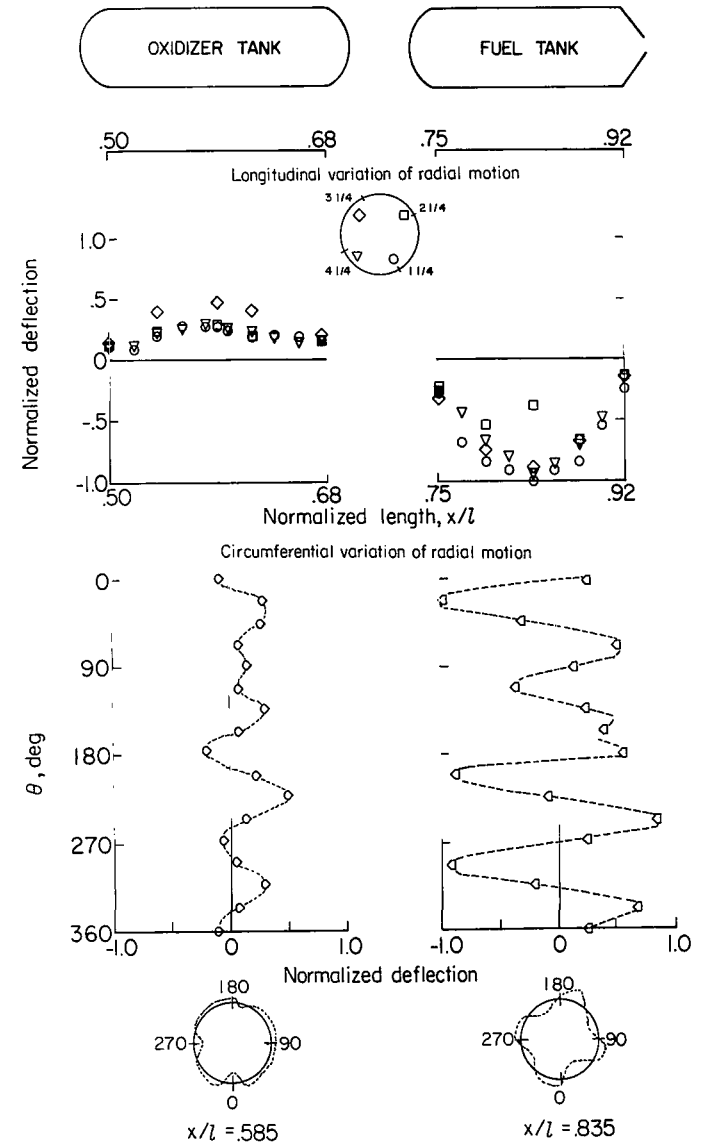
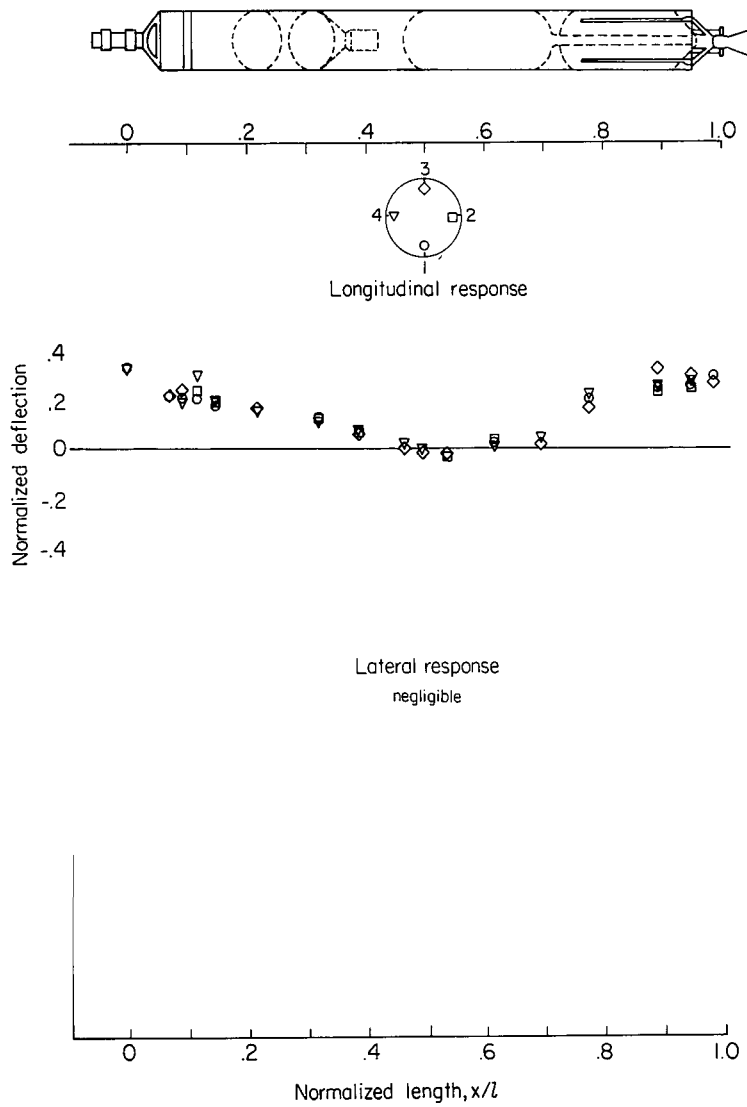


Figure 22.- Coupled response to longitudinal excitation normalized to fuel-tank deflection at $x/l = 0.835$ and $\theta = 22.5^\circ$. $t = 0$; $f = 42.3$ cps.

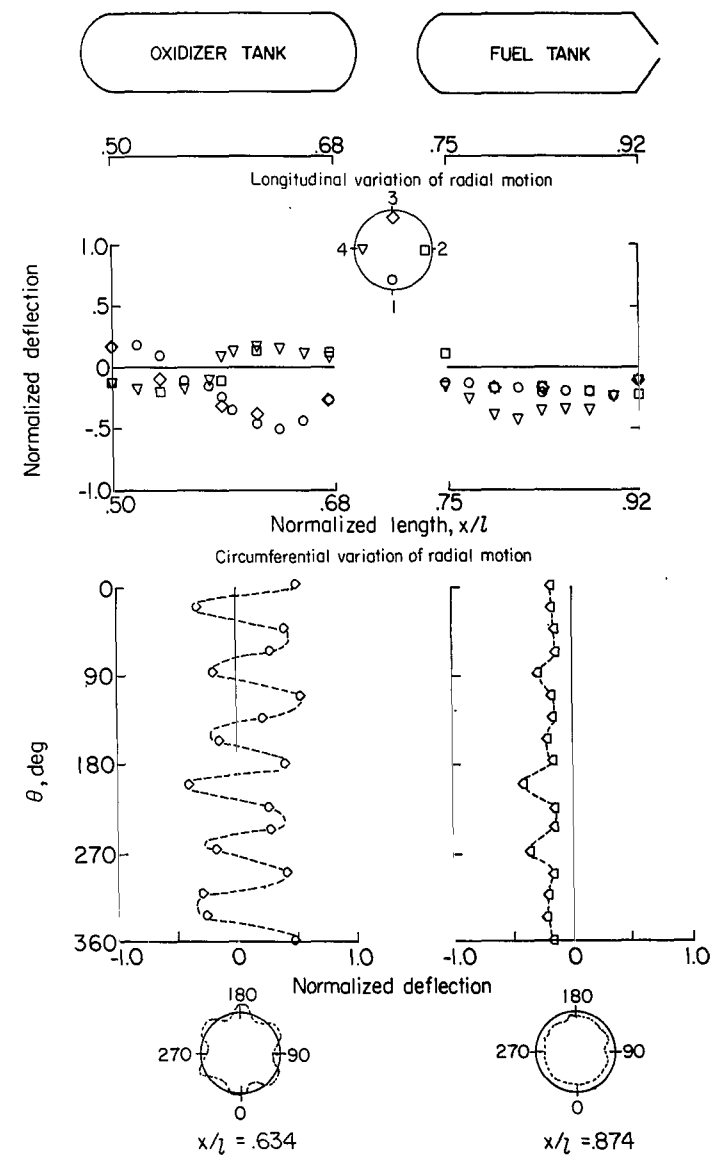
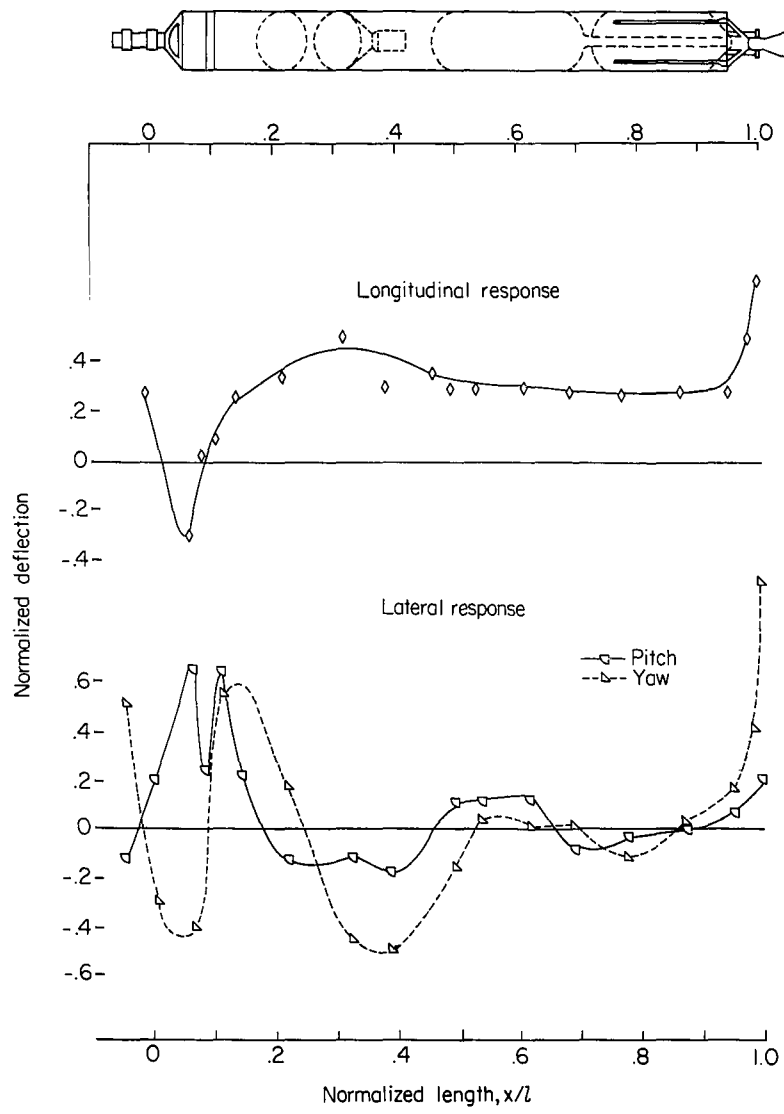


Figure 23.- Coupled response to longitudinal excitation normalized to lateral yaw response at $x/l = 1.00$. $t = 0$; $f = 74.7$ cps.

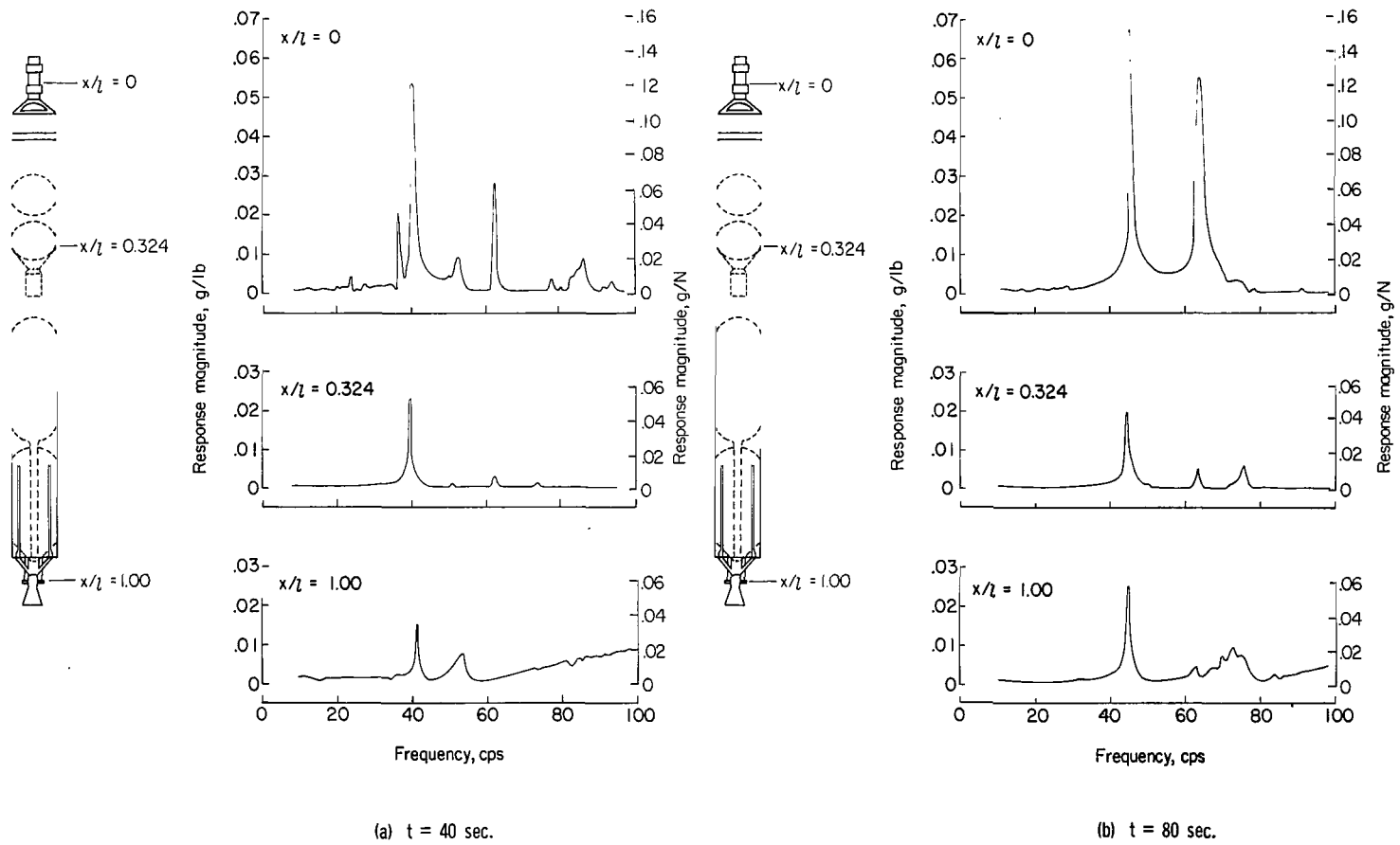
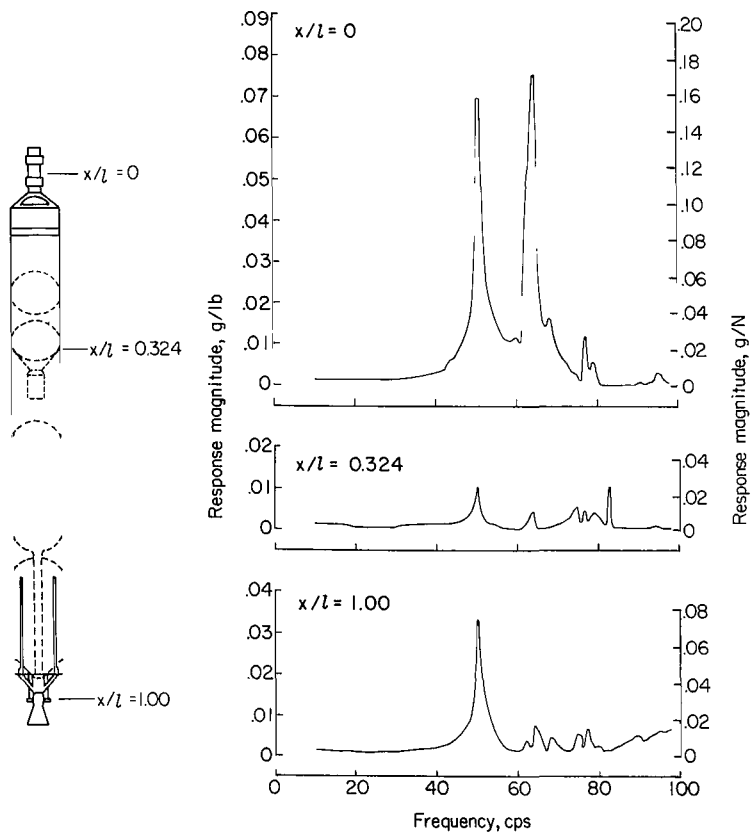
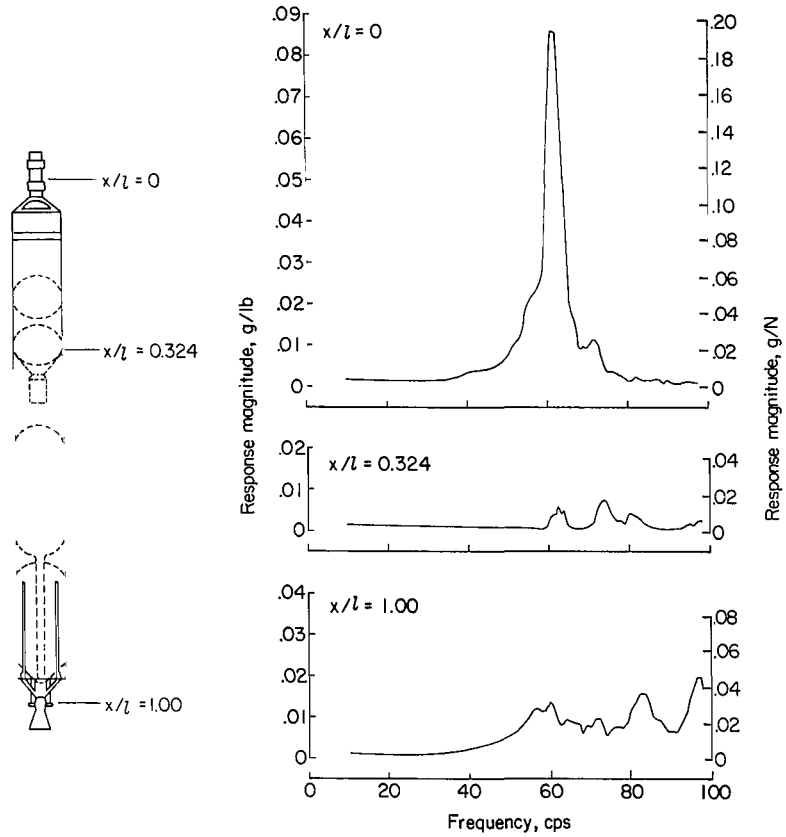


Figure 24.- Longitudinal response as a function of frequency.



(c) $t = 120$ sec.



(d) $t = 152$ sec.

Figure 24.- Concluded.

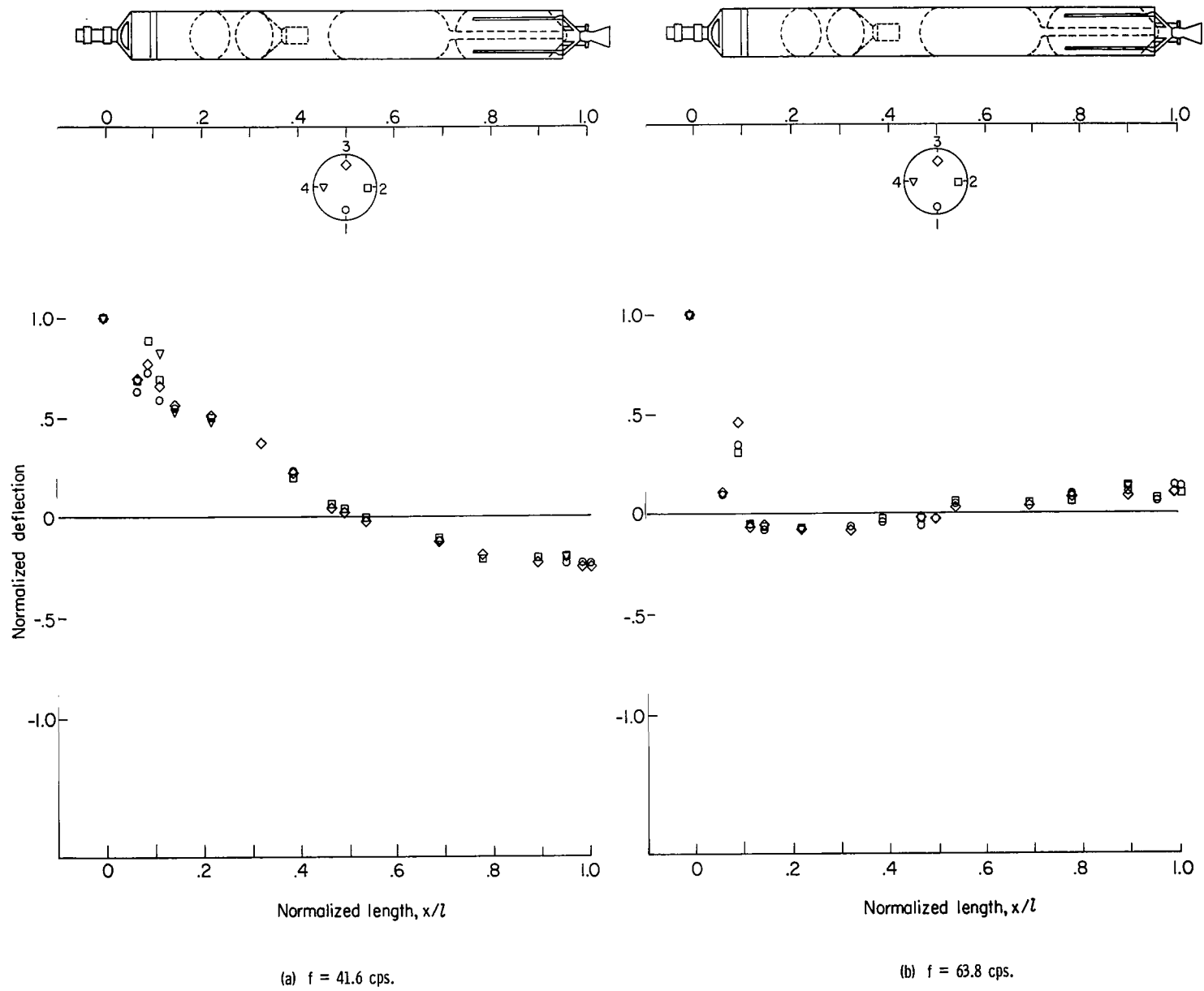


Figure 25.- Measured longitudinal response at $t = 40$ sec.

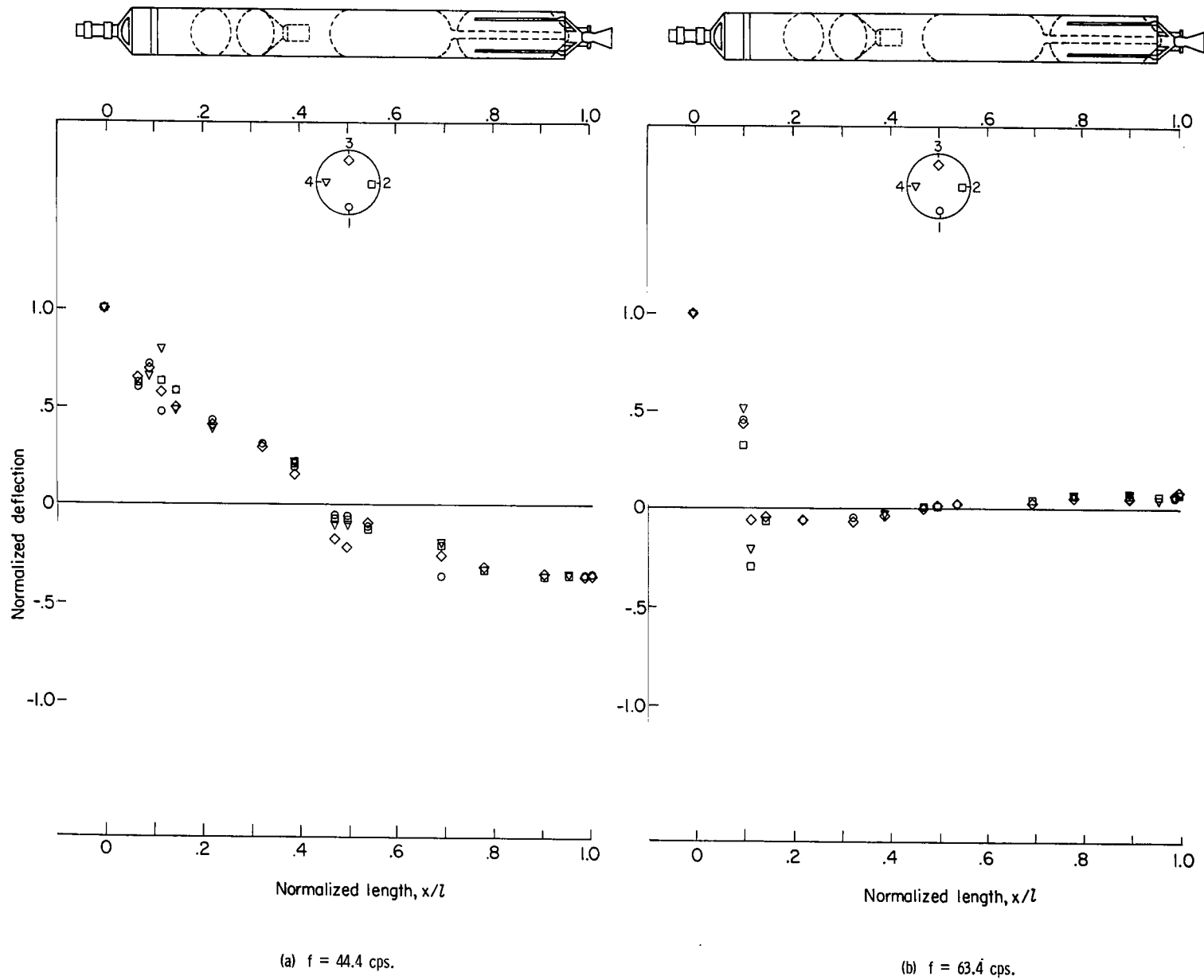
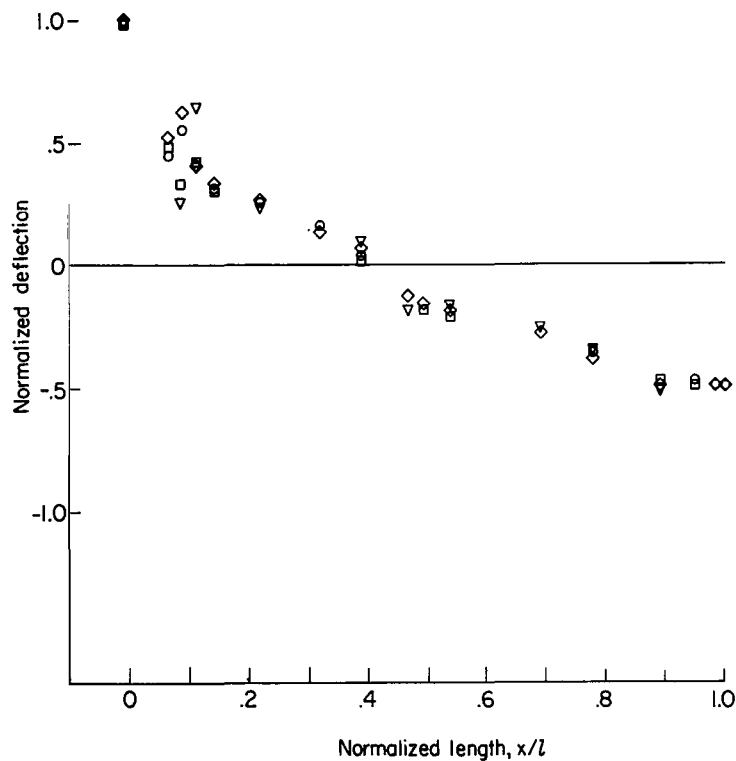
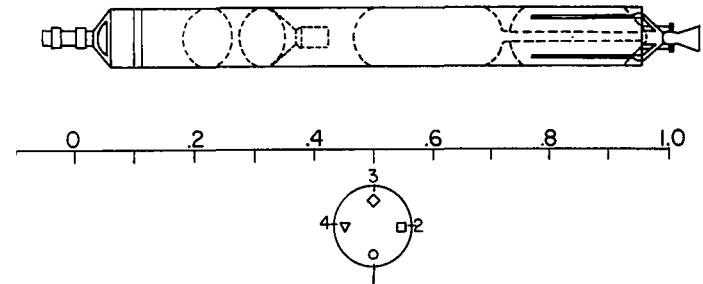
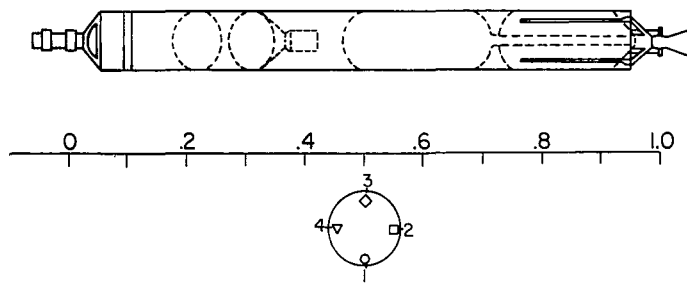
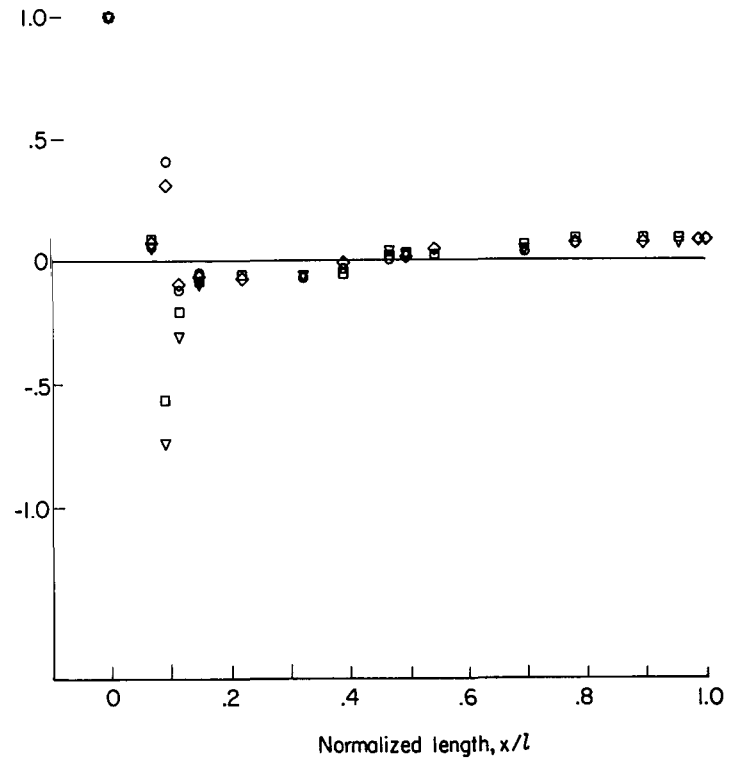


Figure 26.- Measured longitudinal response at $t = 80$ sec.



(a) $f = 50.3$ cps.



(b) $f = 64.1$ cps.

Figure 27.- Measured longitudinal response at $t = 120$ sec.

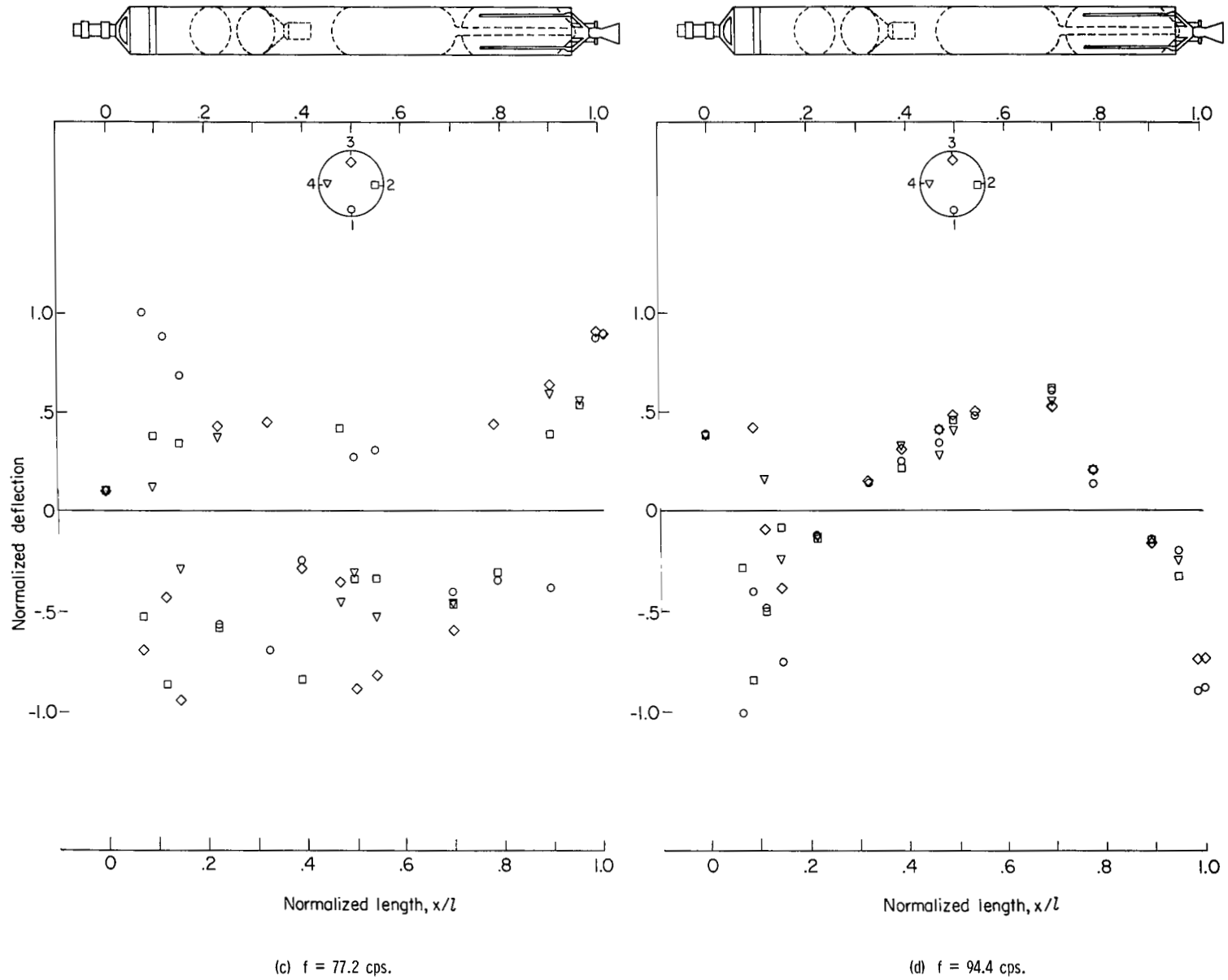
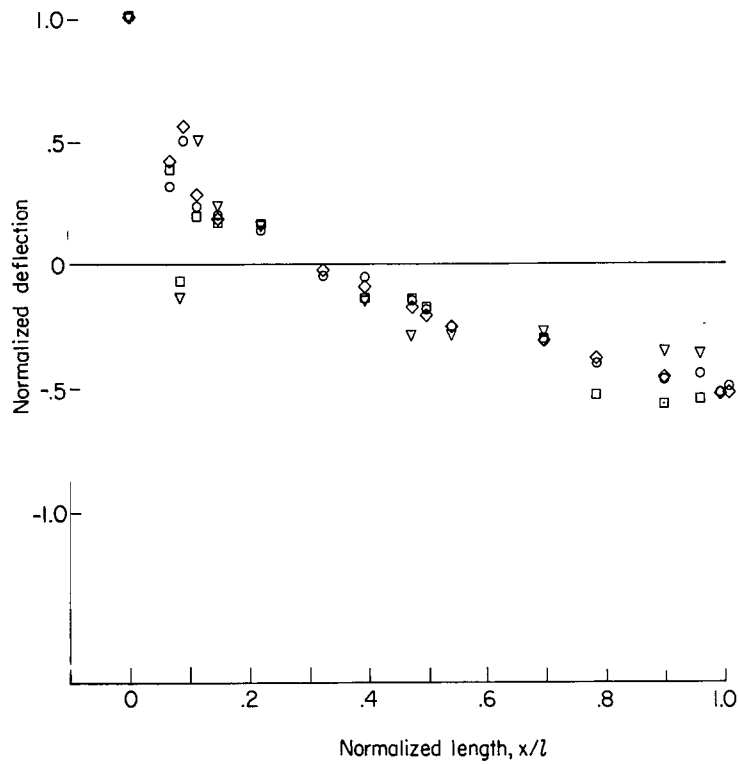
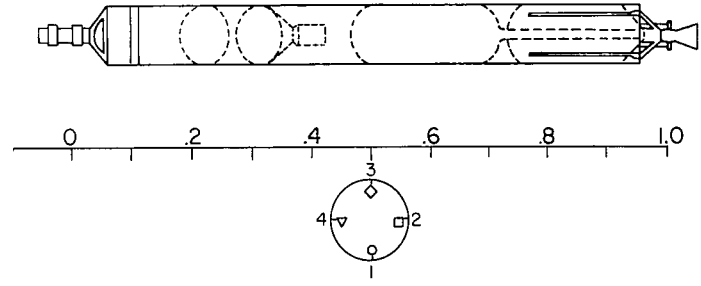
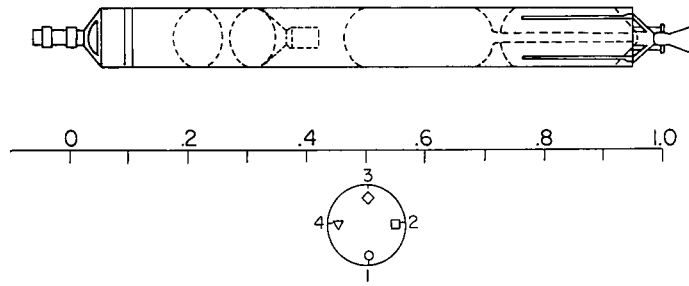
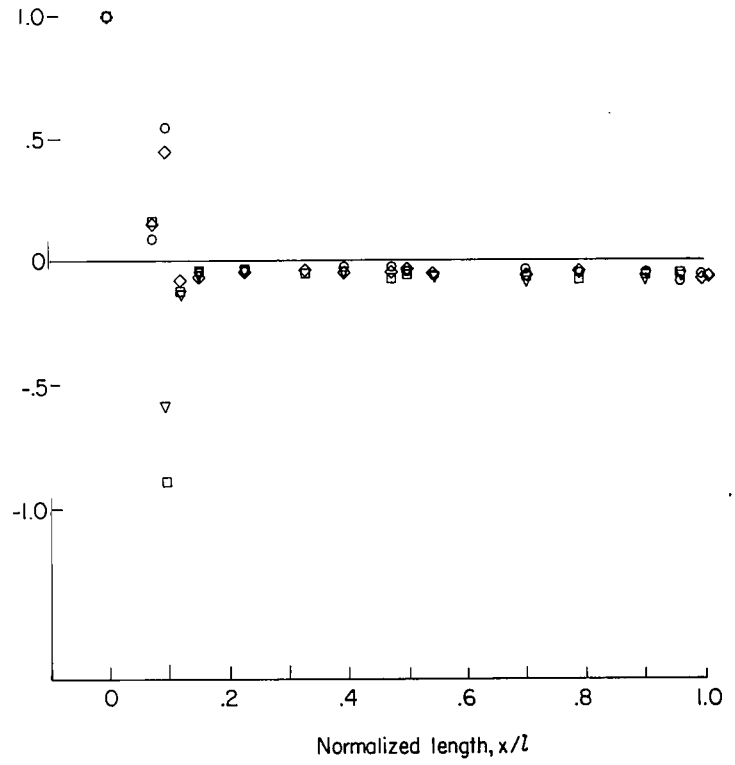


Figure 27.- Concluded.

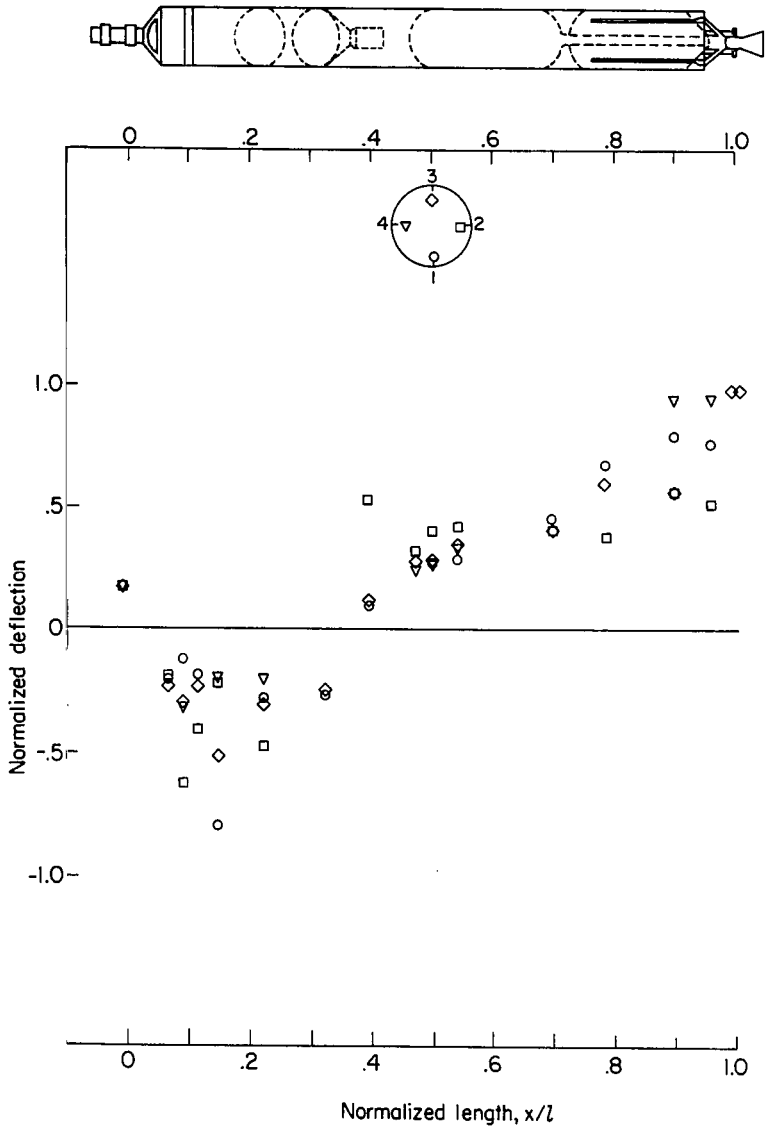


(a) $f = 55.2$ cps.

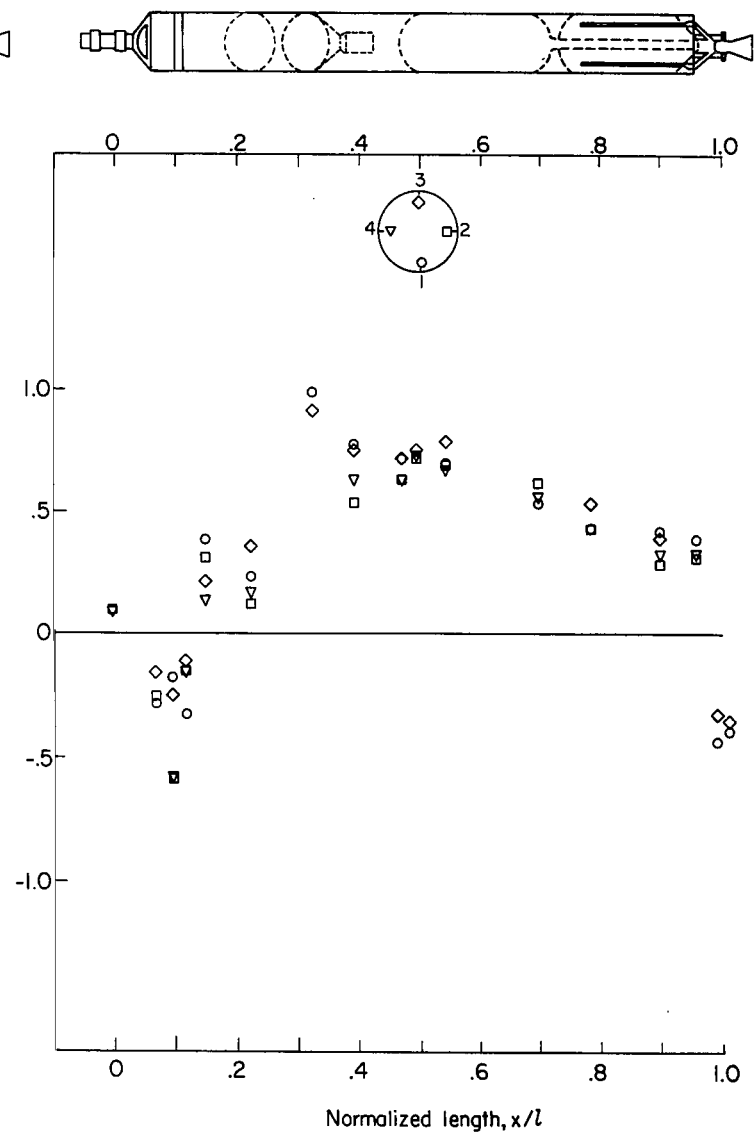


(b) $f = 63.3$ cps.

Figure 28.- Measured longitudinal response at $t = 152$ sec.



(c) $f = 80.0$ cps.



(d) $f = 110.0$ cps.

Figure 28.- Concluded.

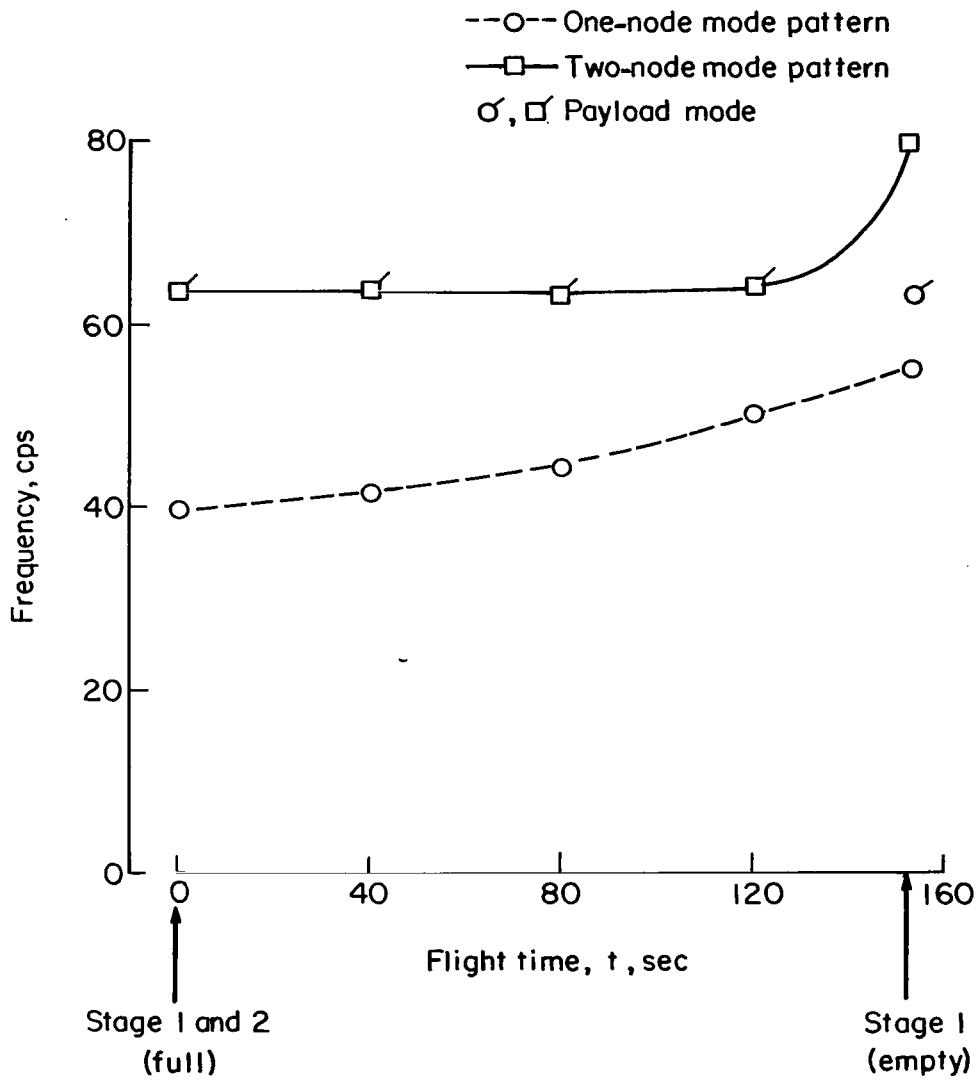


Figure 29.- Variation of measured frequency with propellant loading for the two lowest-frequency longitudinal modes.

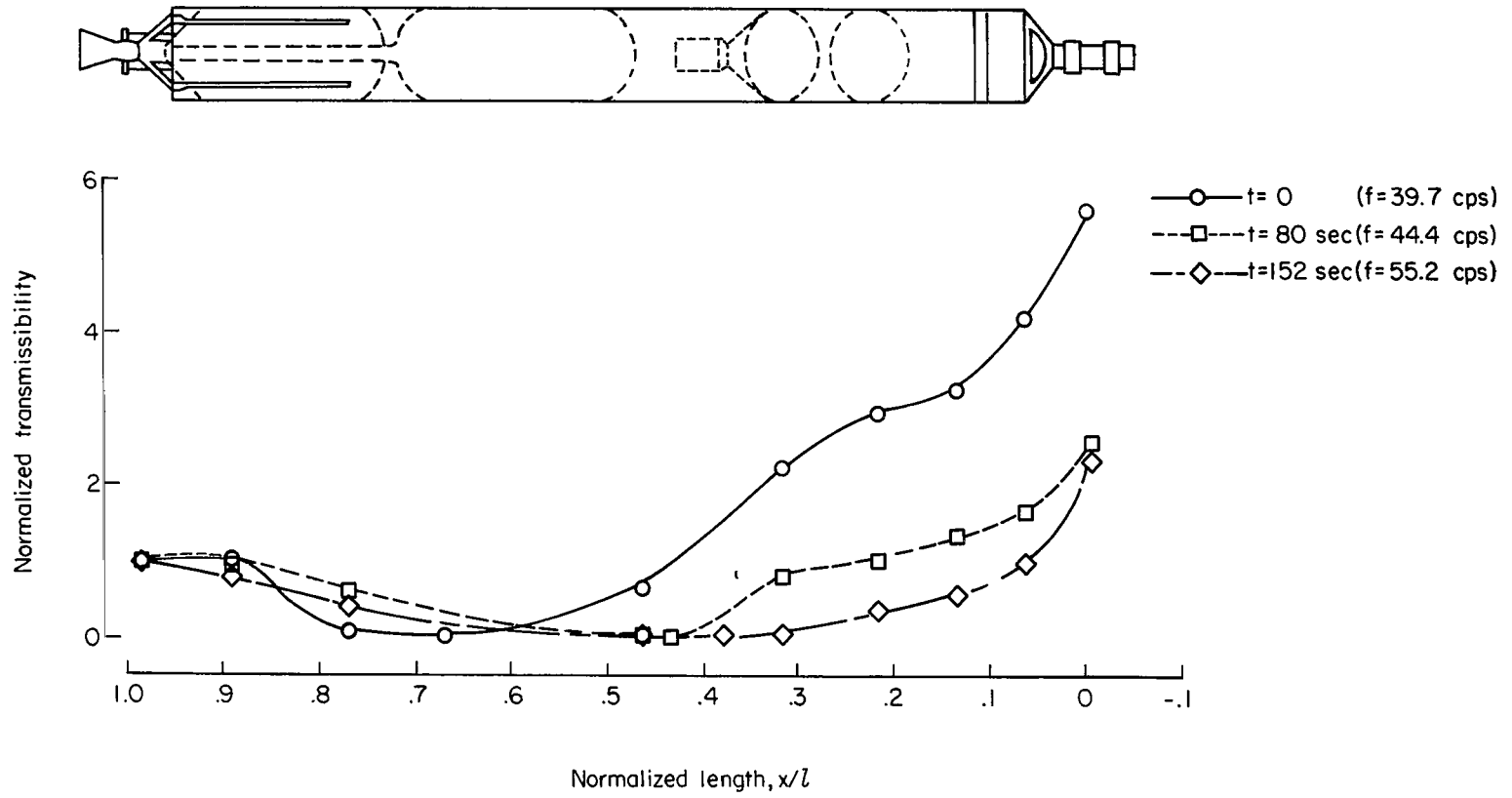
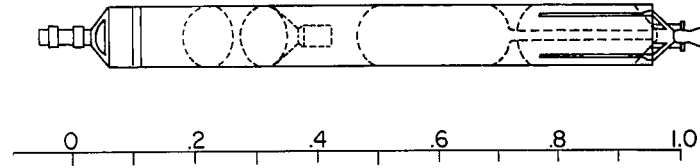
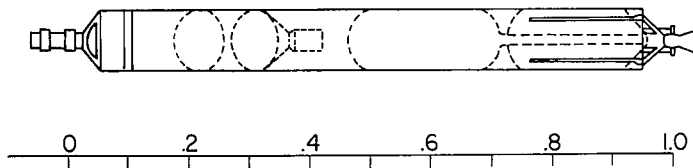


Figure 30.- Transmissibility of structure in longitudinal direction for lowest resonance (force applied and response normalized at $x/l = 1.00$).



Experimental: f, cps
 ○ Average at station 39.7
 Calculated:
 — Component model 36.8

Experimental: f, cps
 ○ Average at station 63.5
 Calculated:
 — Component model 62.5

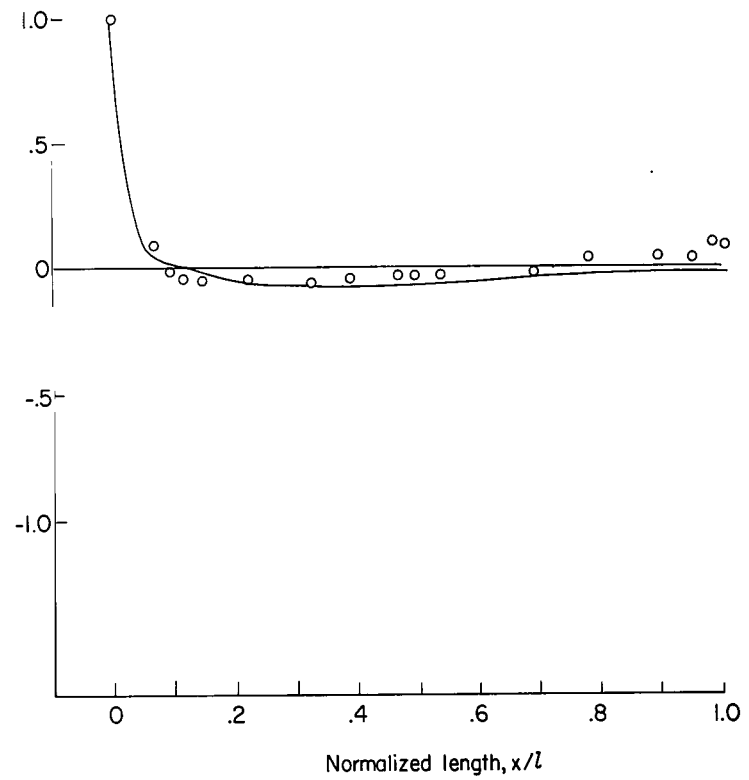
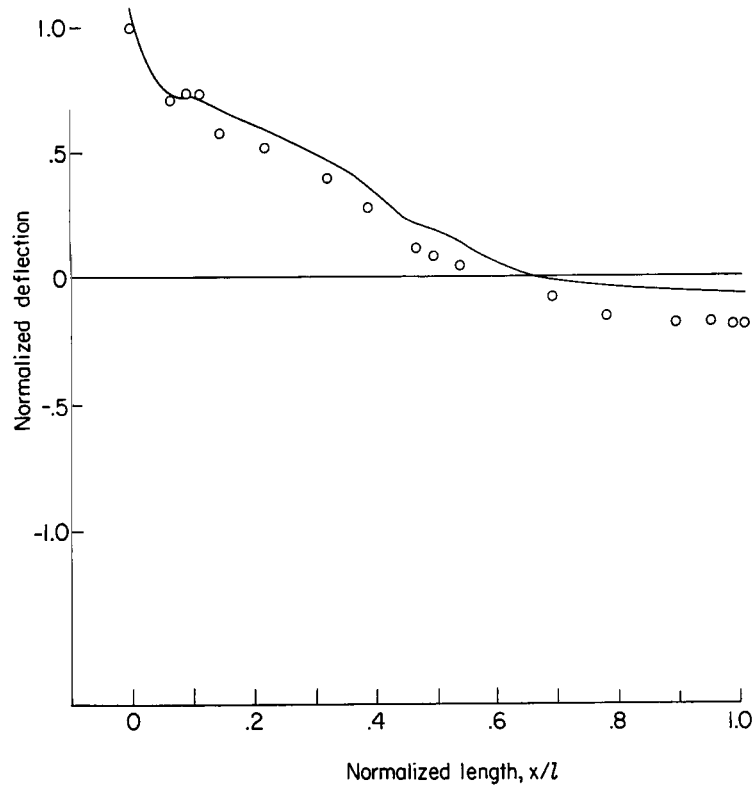


Figure 31.- Comparison of measured and calculated longitudinal response at $t = 0$.

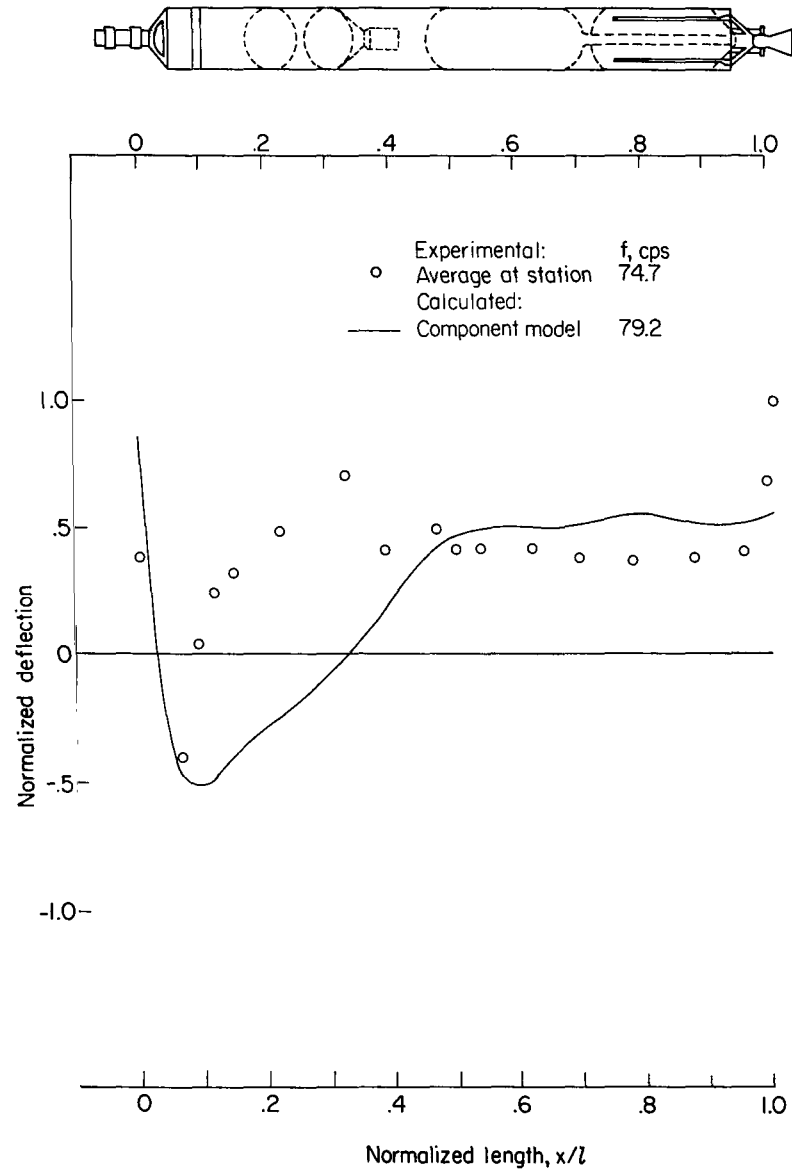
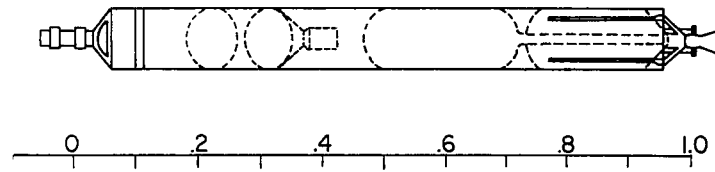
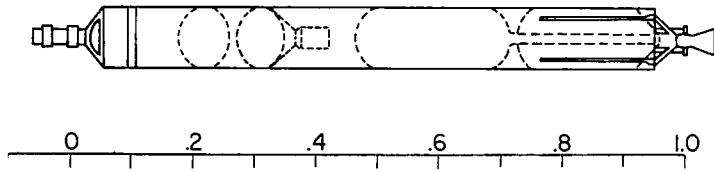


Figure 31.- Concluded.



Experimental: f,cps
 ○ Average at station 41.6
 Calculated:
 — Component model 41.7

Experimental: f,cps
 ○ Average at station 63.8
 Calculated:
 — Component model 63.9

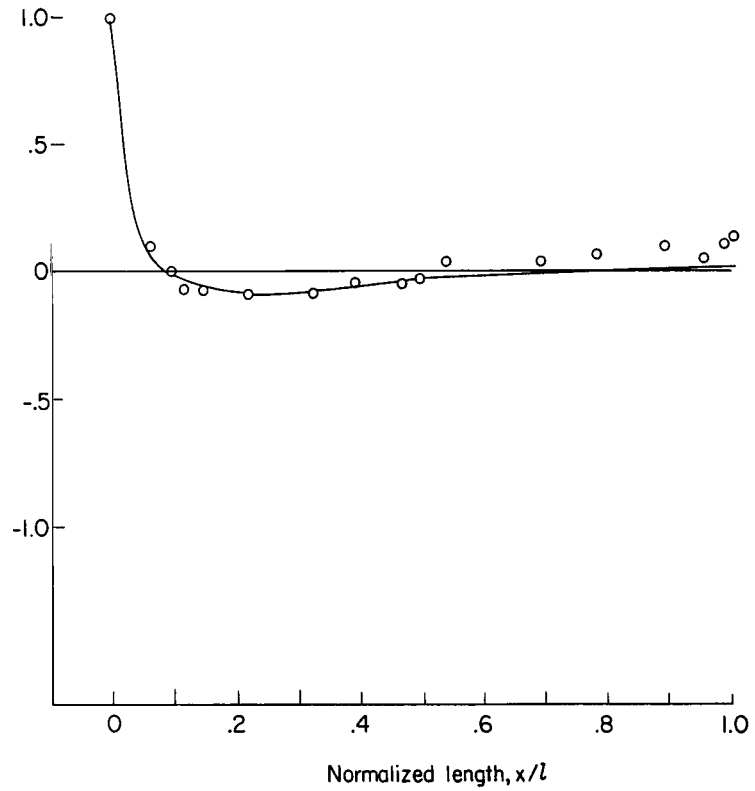
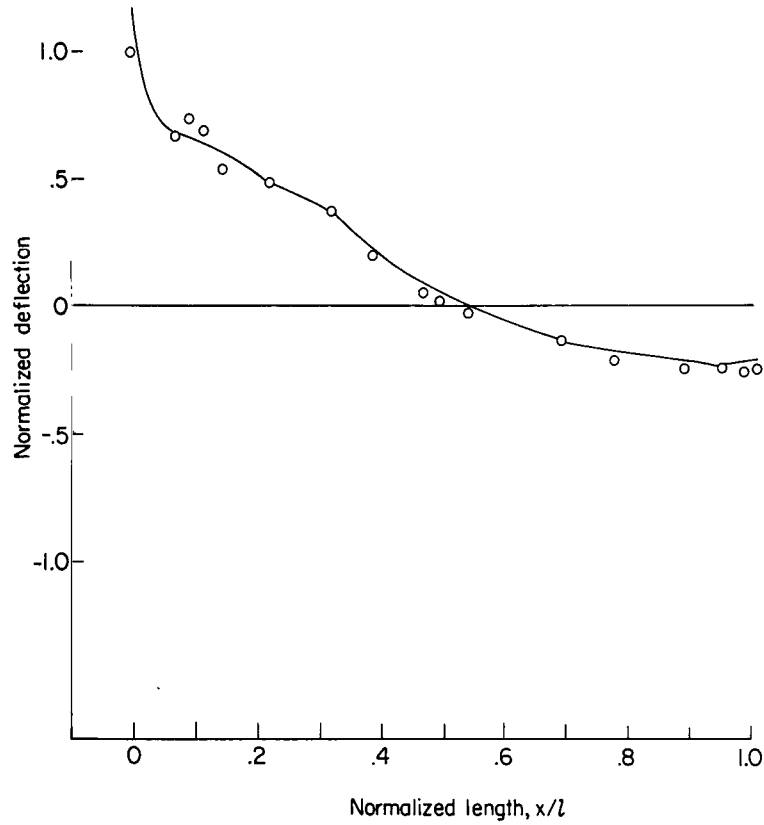


Figure 32.- Comparison of measured and calculated longitudinal response at $t = 40$ sec.

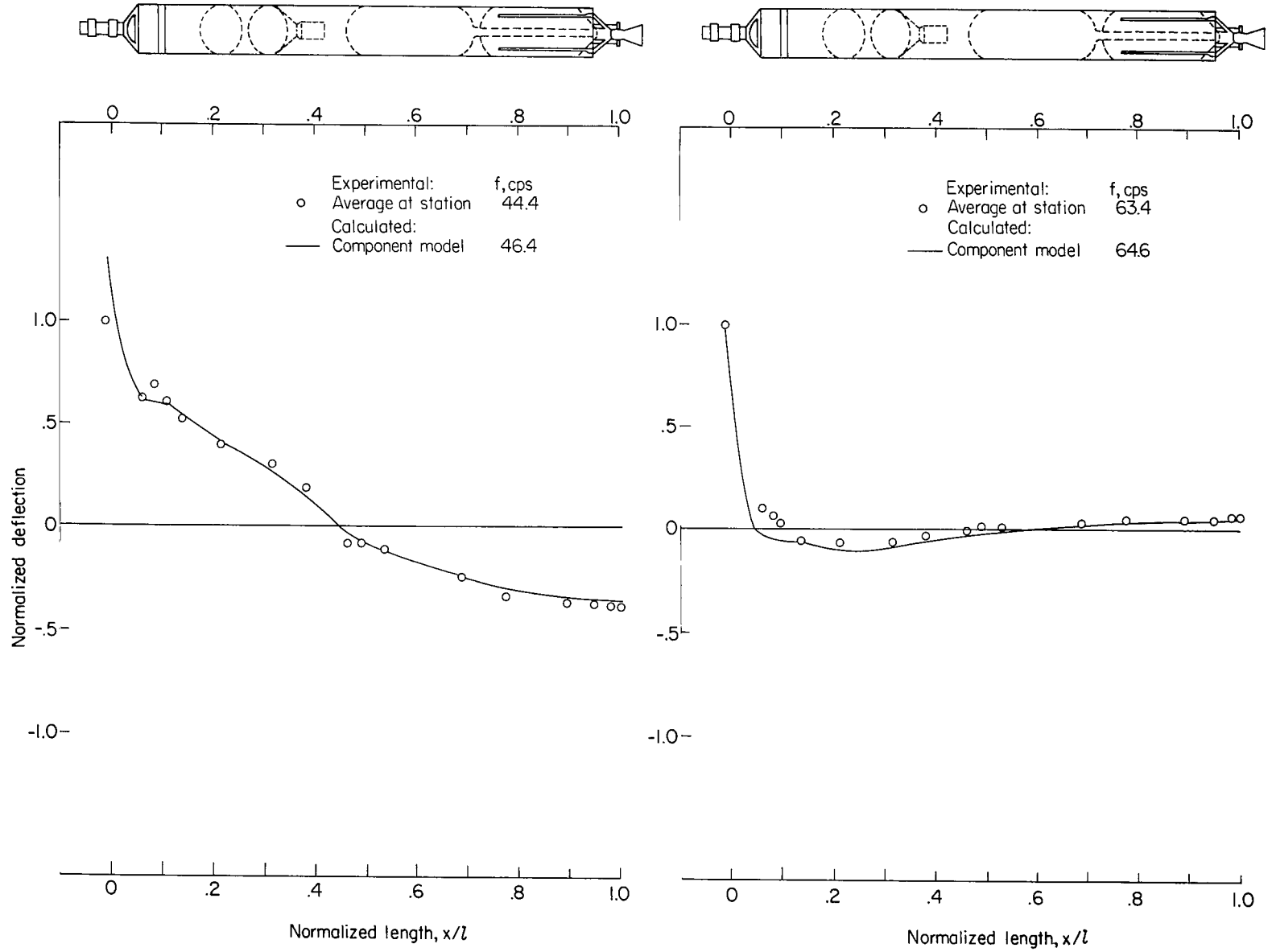


Figure 33.- Comparison of measured and calculated longitudinal response at $t = 80$ sec.

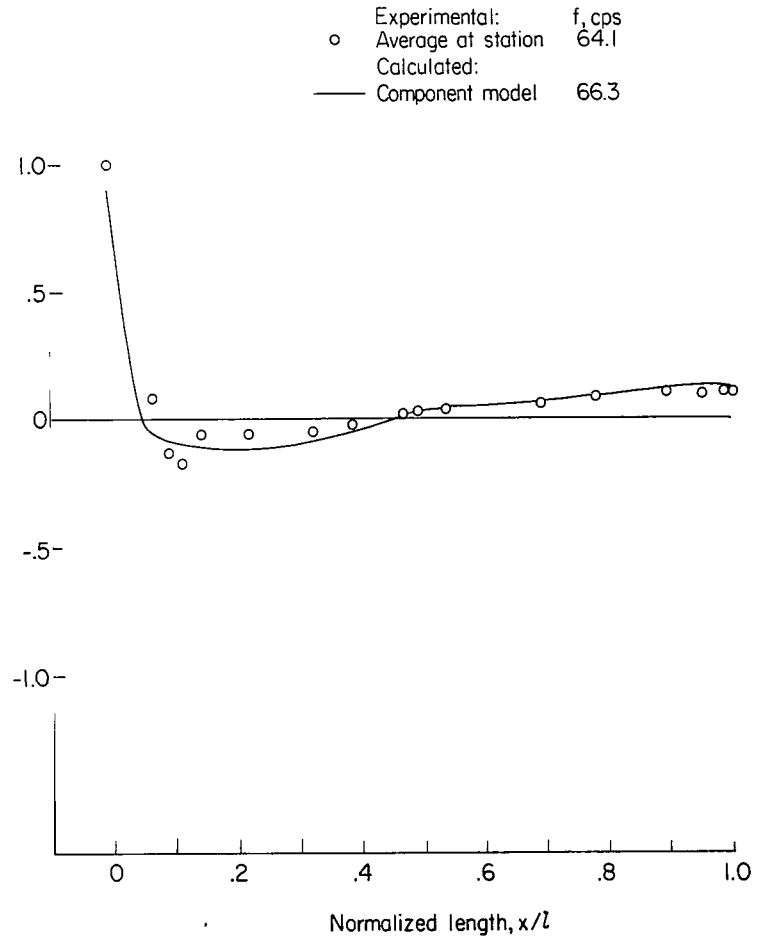
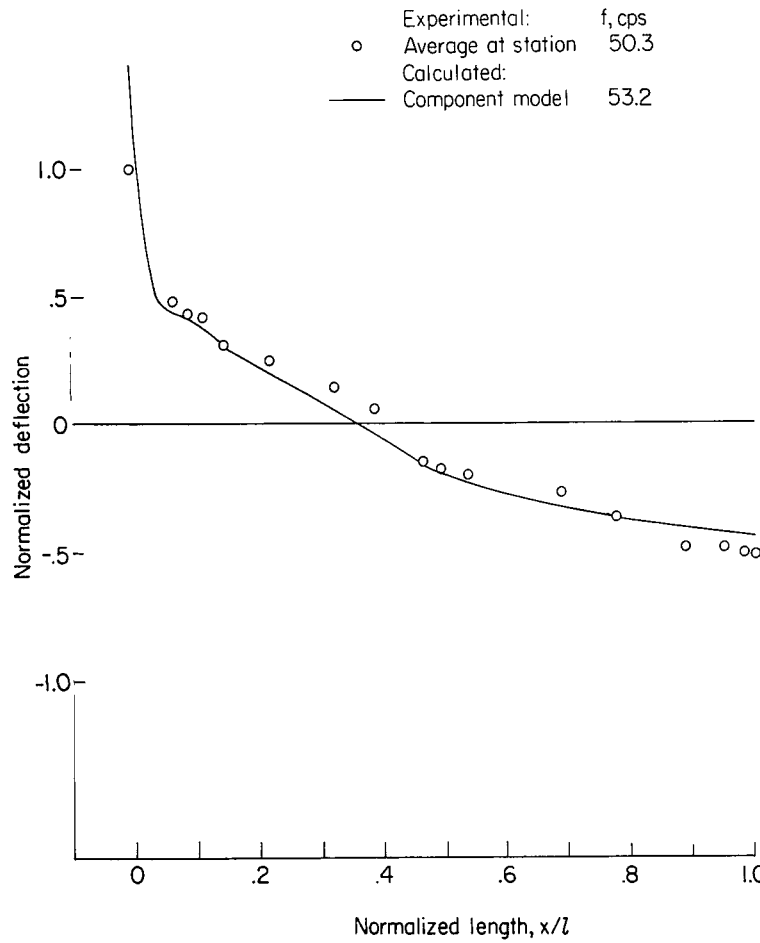
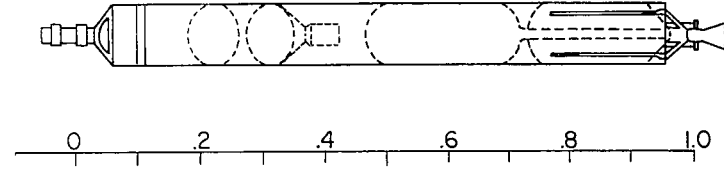
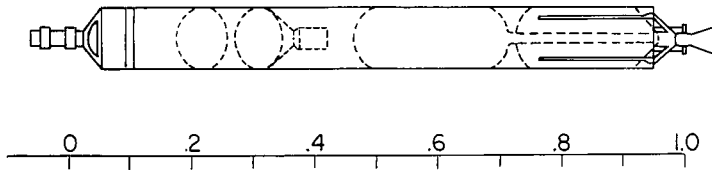


Figure 34.- Comparison of measured and calculated longitudinal response at $t = 120$ sec.

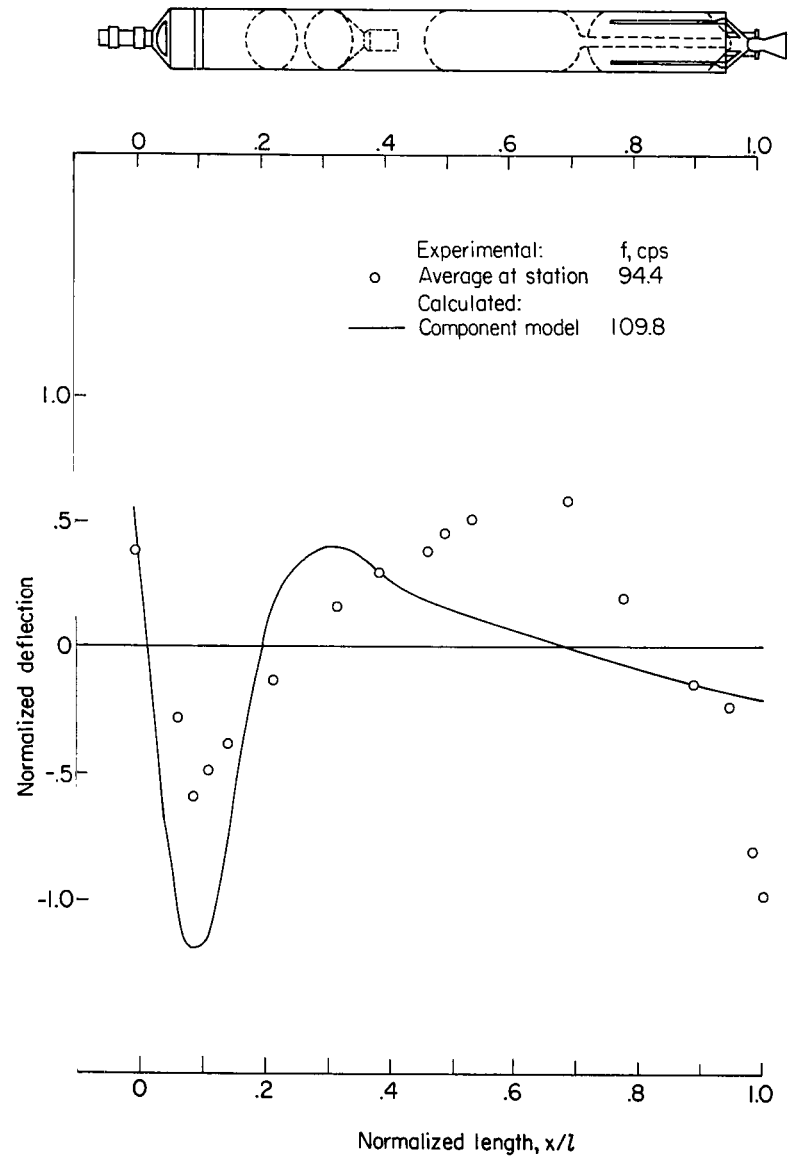
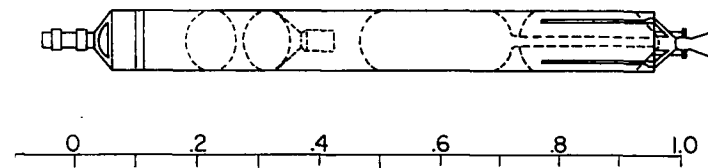
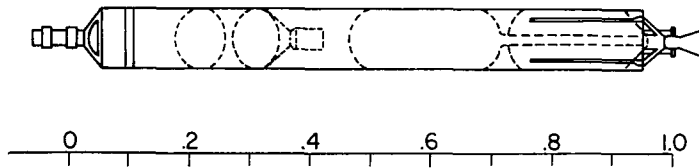


Figure 34.- Concluded.



Experimental: f, cps
 ○ Average at station 63.3
 Calculated:
 — Component model 60.8

Experimental: f, cps
 ○ Average at station 80.0
 Calculated:
 — Component model 81.4

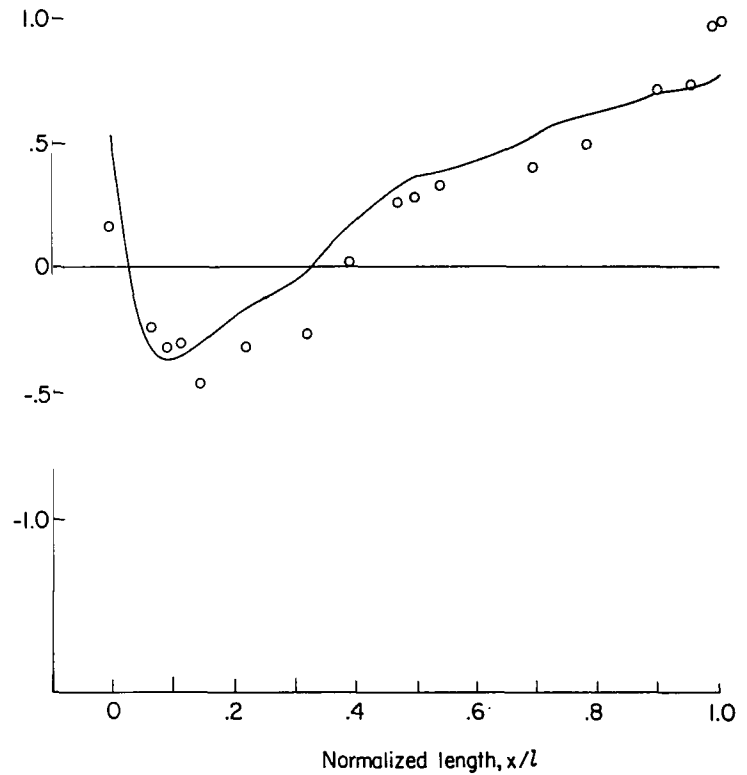
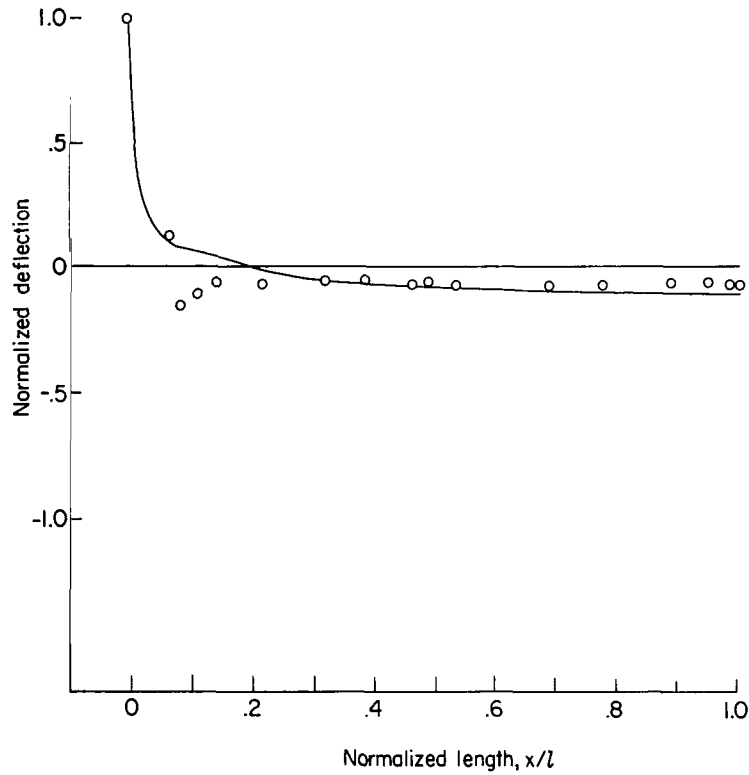


Figure 35.- Comparison of measured and calculated longitudinal response at $t = 152$ sec.

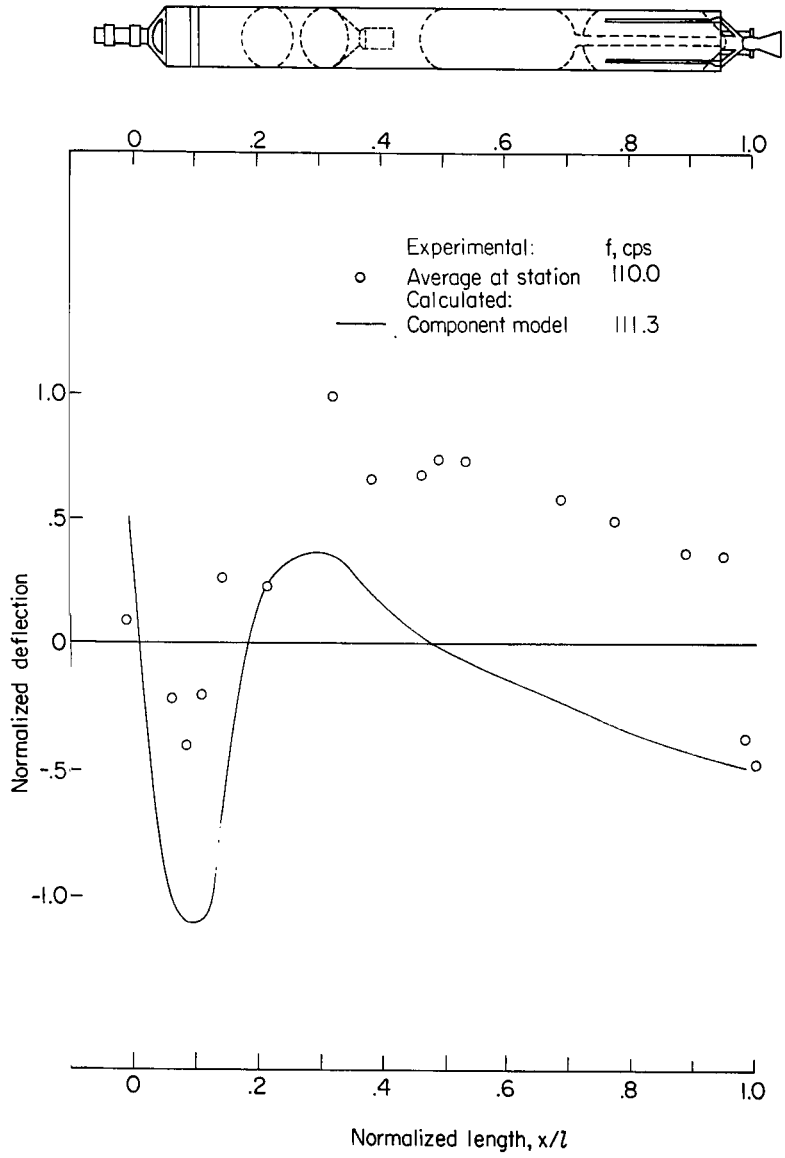


Figure 35.- Concluded.

"The aeronautical and space activities of the United States shall be conducted so as to contribute . . . to the expansion of human knowledge of phenomena in the atmosphere and space. The Administration shall provide for the widest practicable and appropriate dissemination of information concerning its activities and the results thereof."

—NATIONAL AERONAUTICS AND SPACE ACT OF 1958

NASA SCIENTIFIC AND TECHNICAL PUBLICATIONS

TECHNICAL REPORTS: Scientific and technical information considered important, complete, and a lasting contribution to existing knowledge.

TECHNICAL NOTES: Information less broad in scope but nevertheless of importance as a contribution to existing knowledge.

TECHNICAL MEMORANDUMS: Information receiving limited distribution because of preliminary data, security classification, or other reasons.

CONTRACTOR REPORTS: Scientific and technical information generated under a NASA contract or grant and considered an important contribution to existing knowledge.

TECHNICAL TRANSLATIONS: Information published in a foreign language considered to merit NASA distribution in English.

SPECIAL PUBLICATIONS: Information derived from or of value to NASA activities. Publications include conference proceedings, monographs, data compilations, handbooks, sourcebooks, and special bibliographies.

TECHNOLOGY UTILIZATION PUBLICATIONS: Information on technology used by NASA that may be of particular interest in commercial and other non-aerospace applications. Publications include Tech Briefs, Technology Utilization Reports and Notes, and Technology Surveys.

Details on the availability of these publications may be obtained from:

SCIENTIFIC AND TECHNICAL INFORMATION DIVISION
NATIONAL AERONAUTICS AND SPACE ADMINISTRATION

Washington, D.C. 20546